The Sun is rising over the North Sea

Assessment of offshore solar photovoltaics

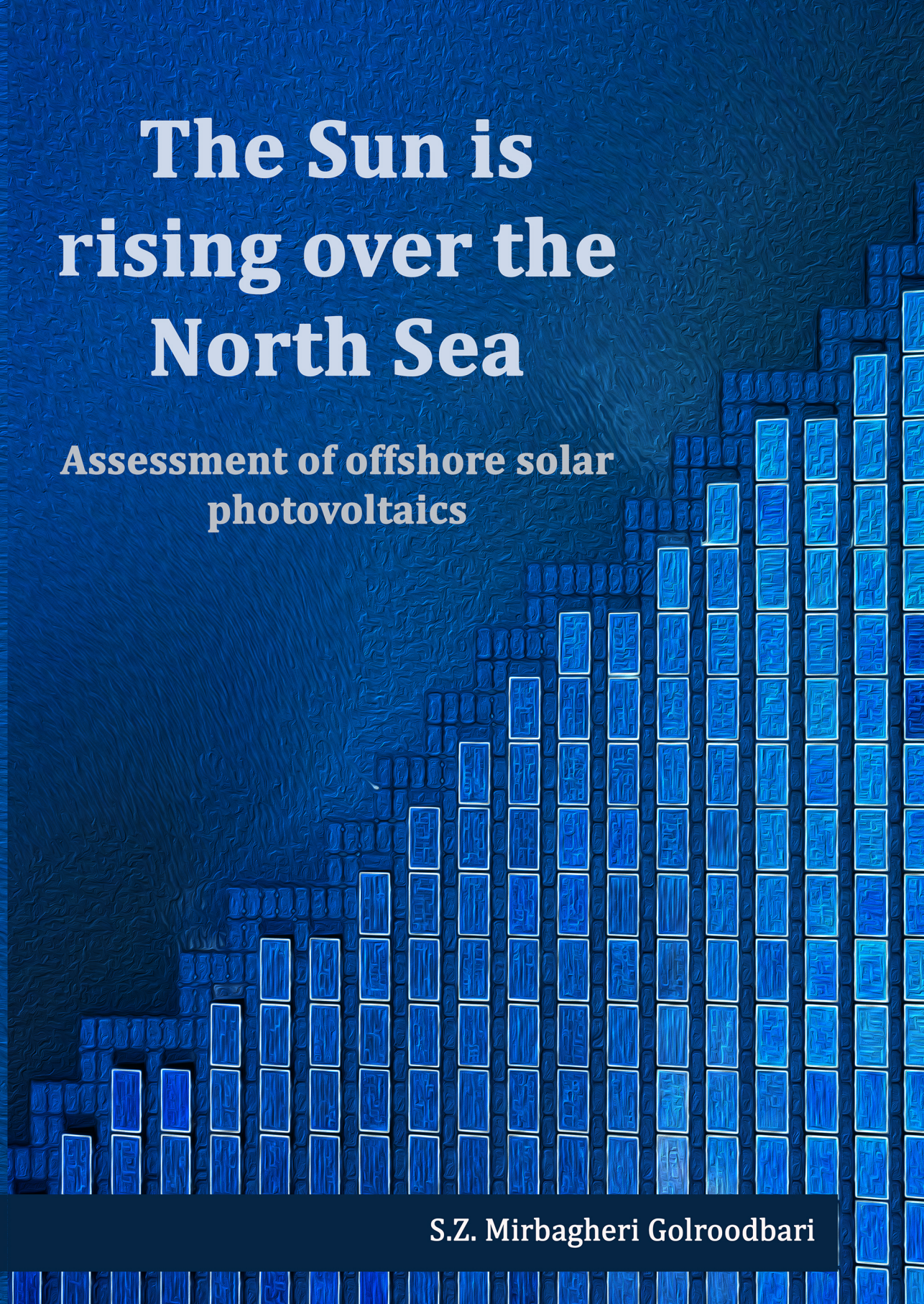

S.Z. Mirbagheri Golroodbari

The Sun is rising over the North Sea

Assessment of offshore solar photovoltaics

S.Z. Mirbagheri Golroodbari

The Sun is rising over the North Sea
Assessment of offshore solar photovoltaics

Copernicus Institute of Sustainable Development

Sayedeh Zahra Mirbagheri Golroodbari

ISBN: 978-94-6416-590-6

Cover: Aerial view of a photovoltaic solar plant floating on water showing rows of solar panels mounted in a lagoon.
Photo by: Plotphoto - Freepik.com
Design: Sayedeh Zahra Mirbagheri Golroodbari

The Sun is rising over the North Sea
Assessment of offshore solar photovoltaics

De zon komt op boven de Noordzee
Evaluatie van fotovoltaïsche zonne-energie op zee

(met een samenvatting in het Nederlands)

Proefschrift

ter verkrijging van de graad van doctor aan de
Universiteit Utrecht op gezag van de
rector magnificus, prof.dr. H.R.B.M. Kummeling,
ingevolge het besluit van het college voor promoties
in het openbaar te verdedigen op
vrijdag 4 juni 2021 des middags te 12.15 uur

door

Sayedeh Zahra Mirbagheri Golroodbari

geboren op 16 september 1983
te Lahijan, Iran

Promotor:
Prof. dr. W.G.J.H.M. van Sark

Copromotor:
Dr. A. Louwen

Summary

Floating solar photovoltaics (PV), also referred to as floatovoltaics, is a relatively new application type of PV systems, which is experiencing rapid growth in deployment. Floatovoltaic (FPV) systems do not take up any land, and except for technical space for electrical cabinets, these systems are typically more compact compared to land-based systems. With the very large off-shore potential, FPV can contribute considerably to decarbonising energy supply. In this thesis this new introduced type of PV system will be studied in detail, in particular regarding potential advantages in energy yield and integration aspects.

To this end, the purpose of the first part of this thesis is to model, simulate, and compare the performance of a 3.7 kW floatovoltaic system consisting of 12 panels, with a similar system on land. For a fair comparison the effect of sea waves, wind speed and relative humidity is considered in this model. The sea waves are modeled in the frequency domain, using a wave spectrum. The irradiation on a tilted surface for a floating system is calculated considering the tilt angle that is affected by the sea waves. Moreover, the temperature is estimated based on heat transfer theory and the natural cooling system for both floating and land-based photovoltaic systems. Actual measured weather data is used from two different locations, one at the Utrecht University campus and the other one at the North Sea, are used to simulate the systems thus making the comparison possible. Energy yield is calculated for these weather conditions. The results detailed in Chapter 2 show that the relative annual average output energy is about 13% higher at sea compared to land. However, in some months this relative output energy increases up to 18% higher energy yield at sea.

To have a precise understanding of the effect of open water on variable albedo, this is studied using the FPV simulation model. In Chapter 3 the effect of dynamic albedo is quantified on the generated energy of a floating offshore photovoltaic system, which is assumed to be installed at the North Sea. Albedo is modeled dynamically as a function of solar irradiation, wind speed and solar zenith angle at an hourly time resolution. The energy output of a floating offshore PV system is compared for two scenarios comparing (i) constant albedo and (ii) a modeled dynamically varying albedo. The quantified results show that the system performance in case of a varying albedo is larger by about 3% compared to using a constant albedo.

In order to maximize offshore renewable electricity generation, it has been suggested to construct hybrid systems based on FPV and offshore wind turbines/parks, combining the benefits of both. In Chapter 4, a techno-economic analysis is performed to assess the feasibility of adding an offshore floating solar

farm to an existing Dutch offshore wind farm in the North Sea, under the constraint of a certain fixed transmission capacity. The specific capacity of this cable that connects the offshore park to the onshore grid, is dimensioned for the rated power output of the wind farm. The wind farm capacity factor is assumed to be between 30% and 35%. The principle of cable pooling allows to add floating solar capacity. Using weather data it is found that adding solar capacity leads to forced curtailment due to the cable capacity, but this is quite limited as result of an observed anti-correlation of the solar and wind resource. For the economic part of the analysis, different scenarios regarding subsidy measures are considered for the calculation of net present value and levelized cost of electricity. Also, the optimum additional PV capacity for each scenario is computed. The results show that with higher cost per unit of rated output, optimum PV capacity decreases, but more promising subsidies lead to higher optimized PV capacities. As the aim of the chapter is not to be limited to a case study a methodology is developed for generalization of the techno-economic analysis of a hybrid solar/wind park. In this generalization the initial investment, system degradation, cable capacity, number of operational hours, and energy price are implemented to compute the optimum PV capacity regarding the net present value as an indicator for economic viability of the project.

Several issues, such as the presence of wind turbines in hybrid systems, bird droppings, effect of salinity of sea water, are likely to cause mismatch conditions, especially resulting from partial shading conditions. Partial shading has a non-linear effect on the performance of PV modules and systems. Different methods of optimizing energy harvesting under partial shading conditions have been suggested to mitigate this issue. In Chapter 5, a smart PV module architecture is proposed for improvement of shade resilience in a PV module consisting of 60 silicon solar cells, which compensates the current drops caused by partial shading. The architecture consists of groups of series-connected solar cells in parallel to a DC-DC buck converter. The number of cell groups is optimized with respect to cell and converter specifications using a least-squares support vector machine method. A generic model is developed to simulate the behavior of the smart architecture under different shading patterns, using high time resolution irradiance data. In this research the shading patterns are a combination of random and pole shadows. To investigate the shade resilience, results for the smart architecture are compared with an ideal module, and also ordinary series and parallel connected architectures. Although the annual yield for the smart architecture is 79.5% of the yield of an ideal module, we show that the smart architecture outperforms a standard series connected module by 47%, and a parallel architecture by 13.4%.

In Chapter 6, performance of a shade resilient smart module is studied under

a dynamic shading pattern. A smart module architecture is developed to mitigate the non-linear shading effect on the module performance. Partial shading decreases the output current of the shaded cells and affects the unshaded cells' output power. After distributing the module cells into small groups, based on a least square support vector machine optimization method, DC-DC buck converters compensate the decreased current levels, by adjusting the output current and voltage level from any individual group of cells. The system is simulated in the MATLAB Simulink environment. Results show that the module performs efficiently, and output power of the unshaded groups of cells never decreased because of the effect of shading of the other groups. Additionally, maximum output power is harvested from all groups simultaneously. Prototype hardware is designed and built to implement the proof of concept. The real-time results of hardware testing show that the smart module performs as expected and mitigates partially shaded conditions by extracting maximum power from each cell group, regardless of other cell groups' shading condition.

In summary, in this thesis several aspects of offshore floating PV have been investigated, including energy yield, integration in hybrid solar/wind systems, and mitigating potential shading effects. All in all, this thesis shows that offshore floating PV systems have many advantages, and a bright future is foreseen regarding its widespread deployment.

Samenvatting

Drijvende fotovoltaïsche zonne-energie (PV), ook wel floatovoltaïsche zonne-energie genoemd, is een relatief nieuwe manier voor het toepassen van PV-systemen, en deze toepassing maakt een snelle groei door. Floatovoltaïsche (FPV) systemen nemen geen land in beslag en zijn doorgaans compacter vergeleken met systemen op het land, met uitzondering van benodigde kasten voor omvormers. FPV heeft een zeer groot off-shore potentieel en daarmee kan FPV aanzienlijk bijdragen aan het koolstofarm maken van de energievoorziening. In dit proefschrift wordt deze nieuwe PV toepassingsvorm in detail bestudeerd, in het bijzonder met betrekking tot potentiële voordelen ten aanzien van energieopbrengst en integratiemogelijkheden.

In het eerste deel van dit proefschrift wordt een model opgesteld om de energieopbrengst te simuleren van een 3.7 kW FPV systeem bestaande uit 12 PV panelen in vergelijking tot een soortgelijk systeem dat op land is geplaatst. Voor een goede vergelijking wordt in het model ook rekening gehouden met het effect van golven op zee, windsnelheid en relatieve vochtigheid. De zeegolven zijn gemodelleerd in het frequentiedomein, gebruik makend van een golfspectrum. De zonneinstraling op een gekanteld oppervlak voor een drijvend PV systeem wordt berekend rekening houdend met de kantelhoek die beïnvloed wordt door de golven. Bovendien wordt de temperatuur geschat op basis van warmteoverdrachtstheorie en het natuurlijke koelsysteem voor zowel drijvende als landgebonden PV systemen. Gemeten weergegevens worden gebruikt van twee verschillende locaties, één op de campus van de Universiteit Utrecht en één op de Noordzee, om energieopbrengst van de systemen te simuleren en zo de vergelijking mogelijk te maken. De resultaten beschreven in hoofdstuk 2 laten zien dat de relatieve jaarlijkse gemiddelde energieproductie op zee ongeveer 13% hoger is vergeleken met land. In sommige maanden kan dit echter toenemen tot 18% hogere energieopbrengst op zee.

Om een beter begrip te verkrijgen van het effect van een variabele albedo op energieopbrengst van een FPV systeem is het FPV-simulatiemodel aangepast. In hoofdstuk 3 wordt het effect van dynamische albedo gekwantificeerd op de opgewekte energie van een drijvende offshore PV systeem op de Noordzee. Een variabele albedo is gemodelleerd als functie van zonnestraling, windsnelheid en hoogte van de zon met een tijdsresolutie van een uur. De energieopbrengst van een drijvend offshore PV-systeem wordt vergeleken voor twee scenario's, dat wil zeggen voor een constante albedo en een gemodelleerd dynamisch variërende albedo. De simulatieresultaten laten zien dat de systeemprestaties in het geval van een variërende albedo ongeveer 3% groter is in vergelijking met het gebruik van een con-

stante albedo.

Om de opwekking van hernieuwbare elektriciteit op zee te maximaliseren, zijn hybride systemen voorgesteld op basis van FPV en offshore windparken, waarbij de voordelen van beide worden gecombineerd. In hoofdstuk 4, wordt een techno-economisch analyse uitgevoerd om de haalbaarheid te beoordelen van het toevoegen van een offshore drijvend zonnepark aan een bestaand Nederlands offshore windpark in de Noordzee, waarbij de beschikbare transportcapaciteit een beperking is. De specifieke capaciteit van deze kabel die het offshore park verbindt met het onshore grid, is gedimensioneerd voor het nominale vermogen van het windpark. Er wordt uitgegaan van een capaciteitsfactor van het windpark tussen 30% en 35%. Het principe van kabelpooling maakt het mogelijk om FPV systemen toe te voegen aan het windpark. Gebruik makend van weergegevens blijkt dat het toevoegen van zonnecapaciteit leidt tot gedwongen vermogensbegrenzing vanwege de kabelcapaciteit, maar dit is beperkt vanwege een waargenomen anticorrelatie van de zonneinstraling en windsnelheid. Voor het economische onderdeel van de analyse worden verschillende scenario's met betrekking tot subsidiemaatregelen in beschouwing genomen voor de berekening van de netto contante waarde en elektriciteitskosten. Ook wordt de optimale toegevoegde PV-capaciteit voor elk scenario berekend. De resultaten laten zien dat bij hogere kosten per eenheid nominaal vermogen de optimale PV-capaciteit afneemt, maar dat hogere subsidies leiden tot hogere geoptimaliseerde PV-capaciteiten. Het doel van dit hoofdstuk beperkt zich niet tot een case study. Daarom is een methodologie ontwikkeld om de techno-economische analyse van een hybride zon/windpark te generaliseren. In deze generalisatie worden de initiële investering, systeemdegradatie, kabelcapaciteit, aantal operationele uren, en energieprijs meegenomen om een optimum te bepalen voor PV-capaciteit, waarbij de netto contante waarde wordt gebruikt als indicator voor economische levensvatbaarheid van het project.

De aanwezigheid van windturbines in hybride systemen, vogel uitwerpselen samen met het effect van het zoutgehalte van zeewater, zullen waarschijnlijk leiden tot mismatch-omstandigheden in zonnepanelen, vooral als gevolg van gedeeltelijke beschaduwing. Gedeeltelijke beschaduwing heeft een niet-lineair effect op de prestaties van PV-modules en -systemen. Verschillende methodes voor het optimaliseren van energieopbrengst bij gedeeltelijke beschaduwing zijn voorgesteld om dit probleem te verminderen. In hoofdstuk 5 wordt een slimme PV-module-architectuur voorgesteld ter verbetering van de schaduwbestendigheid van een PV-module bestaande uit 60 silicium zonnecellen, die de afname in stroom door gedeeltelijke schaduw kan compenseren.

De architectuur bestaat uit groepen van in serie geschakelde zonnecellen parallel aan een DC-DC buck-converter. Het aantal celgroepen wordt geoptimaliseerd

op basis van cel- en converterspecificaties met behulp van een kleinste kwadraten ondersteuningsvectormachine methode. Er is een generiek model ontwikkeld om het gedrag van de slimme architectuur te simuleren onder verschillende schaduwpatronen, gebruik makend van zonneinstraling met een hoge tijdsresolutie. In dit onderzoek zijn de schaduwpatronen een combinatie van random schaduwen en schaduw van masten. Om de schaduwbestendigheid te onderzoeken zijn de resultaten voor de slimme architectuur vergeleken met die voor een ideale module, maar ook voor standaard serie en parallel geschakelde celarchitecturen. De jaarlijkse opbrengst voor de slimme architectuur is berekend op 79,5% van de opbrengst van een ideale module. De slimme architectuur presteert 47% beter dan een standaard serie geschakelde module met 47%, en 13,4% beter dan een parallelle architectuur.

In hoofdstuk 6 worden de prestaties van een schaduwbestendige slimme module bestudeerd gebruik makend van een dynamisch schaduwpatroon. Een slimme modulearchitectuur is ontwikkeld om het niet-lineaire schaduweffect op de prestaties van de module te mitigeren. Gedeeltelijke schaduw verlaagt de uitgangsstroom van de beschaduwde cellen en beïnvloedt het uitgangsvermogen van de niet beschaduwde cellen. Op basis van de kleinste kwadraten ondersteuningsvectormachine optimalisatie methode, zijn cellen in de module verdeeld in kleine groepen. De DC-DC buck converters compenseren de verlaagde stroomniveaus door de uitgangsstroom en spanningsniveau van een individuele groep cellen aan te passen. Het systeem wordt gesimuleerd met MATLAB Simulink. De resultaten laten zien dat de slimme module efficiënt presteert, en het uitgangsvermogen van de onbeschaduwde groepen neemt niet af ondanks beschaduwing van de andere groepen cellen. Bovendien wordt maximaal uitgangsvermogen verkregen uit alle groepen tegelijk. Prototype hardware is ontworpen en gebouwd om een proof of concept te implementeren. De realtime resultaten van hardwaretests laten zien dat de slimme module presteert zoals verwacht en dat de effecten van gedeeltelijke beschaduwing worden verminderd door maximaal vermogen uit elke celgroep te halen, ongeacht het beschaduwingsniveau van andere celgroepen.

Tenslotte, in dit proefschrift komen verschillende aspecten van offshore drijvende PV systemen aan bod, waaronder energieopbrengst, integratie in hybride zon/windsystemen, en manieren om mogelijke schaduweffecten te verminderen. Al met al laat dit proefschrift zien dat offshore drijven PV-systemen veel voordelen hebben en er wordt verwacht dat in de toekomst deze systemen op grote schaal zullen worden ingezet.

Nomenclature

Abbreviations

Abbr.	Meaning
AM	Air Mass
BIPV	Building-integrated PV
BPD	Bypass diode
BWFZ	Borssele Wind Farm Zone
CF	Capacity factor
DIF	Diffuse irradiance
DIR	Direct irradiance
DMPPT	Distributed MPPT
DR	Dynamic reconfiguration
EA	Evolutionary algorithms
EEZ	Exclusive Economic Zone
FPV	Floating PV
G_M	Global maximum
GHI	Global horizontal irradiation
GTI	Irradiation on the tilted surface
Inc._Cond	Incremental conductance
IR	Infrared
JONSWAP	Joint North Sea Wave Project
LBPV	Land-based PV
LCOE	Levelized cost of electricity
LS-SVM	Least square support vector machine
MEPCM	Micro-encapsulated phase change material
MC	Mismatch conditions
MIE	Module integrated electronics
MOSFET	Metal-Oxide-Semiconductor Field-Effect Transistors
MPPT	Maximum power point tracking
NPV	Net present value
OSA	Ocean surface albedo
P-V	Power-Voltage
P&O	Perturb and observe
PS	Partial shading
PSO	Particle swarm optimization
PV	Photovoltaic
R	Reflective irradiance

Continued from previous page

Abbr.	Meaning
RBF	Radial base function
RES	Renewable energy sources
RPV	Rooftop mounted PV
SDE+	Stimulation of Sustainable Energy Production
SM-MPPT	Sweep Method MPPT
SP	Series parallel
STC	Standard test condition
SZA	Solar zenith angle
TCT	Total-cross-tied
UPOT	Utrecht photovoltaic outdoor test facility
VIS	Visible spectrum

Variables

Symbol	Meaning	Unit
$\alpha_W(\lambda)$	Absorption coefficient of clear water	[m^{-1}]
T_a	Ambient temperature	[^{o}C]
a	Amplitude	[a.u.]
$E_{PV,a}$	Annual generated energy	[kWh]
$E_{WF,a}$	Annual wind farm energy production	[kWh]
$T_{a,p}$	Apparent panel temperature	[^{o}C]
T_A	Apparent temperature	[^{o}C]
γ	Azimuth angle	[Rad]
F_{bl}	Blur factor	–
F_n	Cash-flow after n years	[€]
C	Cell	–
I_{in}	Converter input current	[A]
V_{in}	Converter input voltage	[V]
$E_{WF,N_{year}}$	Cumulative energy generated by the wind farm	[kWh]
$I_{MPP_{STC}}$	Current at Maximum power point in STC	[A]
D	Dew point temperature	[^{o}C]
D_h	Diffuse horizontal irradiance	[W/m^2]
r_b	Direct irradiance conversion factor	–
B_h	Direct normal irradiance	[W/m^2]
T_{db}	Dry bulb temperature	[^{o}C]
η	Efficiency	[%]
η_{Conv}	Efficiency of converter	[%]

Continued from previous page

Symbol	Meaning	Unit
η_{MPPT}	Efficiency of MPPT algorithm	[%]
ρ	Foreground albedo	–
Vd_BP	Forward voltage of diode which bypassed group of cells	[V]
f	Frequency	[HZ]
f_{WC}	Function of wind speed	–
E_Y	Generated energy	[kWh]
G_{GHI}	Global horizontal irradiation	[W/m^2]
g	Gravitational constant	[m/s^2]
E_m	Harvested energy from module m	[kWh]
H	Height	[m]
$E_{PV}(h)$	Hourly generated energy of one PV module	[kWh]
$E_{WF,h}$	Hourly wind farm energy production	[kWh]
G_p	Irradiation level of pixel p	[W/m^2]
G_s	Irradiation level under shadow	[W/m^2]
K	Kernel function	–
f_K	Kluchers' conversion factor	–
$R_{d,LJ}$	Liu-Jordan isotropic model transposition factors	–
m	Mass of substance	[kg]
P_{max}	Maximum output power	[W]
n_g	Number of cells in a group	–
N_G	Number of groups of cells	–
α_{SOA}	Ocean surface albedo	–
V_{OC}	Open circuit voltage	[V]
I_G	Output current of group G	[A]
V_{out}	Output voltage	[V]
P_{MPP}	Output power at maximum power point	[W]
A_{PV}	Panel area	[m^2]
β	Panel tilt angle	[^{o}C]
p	Pixel	–
R_{dd}	Ratio of diffuse to direct irradiation	[a.u.]
R_E	Ratio of output energy to ideal module	–
R_ϕ	Reflected irradiance	[W/m^2]
RH	Relative humidity	[%]
E_R	Rotating kinetic energy	[J]
σ	Roughness of the sea surface	[m]
F_{shaded}	Shaded fraction of cells	–

Continued from previous page

Symbol	**Meaning**	**Unit**
I_{SC}	Short circuit current	[A]
$G(h)$	Solar irradiation per hour	[Wh/m^2]
θ_z	Solar zenith angle	[Rad]
ζ	Solar zenith angle	[Rad]
σ	Standard deviation	
α	Surface albedo	–
β	Surface tilt angle	[Rad]
T	Time Period	[s]
τ	Torque	[N.m]
π_i	Total energy value	[€]
N_{shaded}	Total number of shaded cells	–
N_C	Total number of pixels	–
P_{total}	Total output power	[W]
Π_a	Total revenue	[€]
F_{tr}	Transparency factor	–
R_h	Transposition factor for ground reflection	–
$F_{unshaded}$	Unshaded fraction of cells	–
p_v	Vapour pressure of air (hPa)	[^{o}C]
$Vnon\_BP$	Voltage of group of cells which are not bypassed	[V]
λ	Wavelength	[nm]
v	Wind speed at 10 m height	[m/s]

Contents

1

Introduction

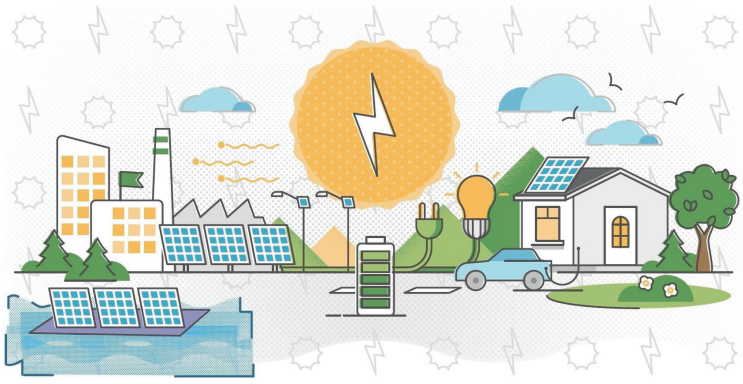

1.1 Motivation

In order to combat global warming and meet the targets set by the 2015 Paris Agreement, the world will have to rely increasingly on renewable energy sources. Electricity generation is one sector in which the move towards non-polluting sources can be highly effective. In the recent World Energy Outlook 2020 of the International Energy Agency (IEA) it is stated that solar photovoltaics (PV) is the "new king of electricity supply", in their Net Zero Emissions by 2050 (NZE2050) scenario, which assumes additions of PV to reach 500 GWp annually by 2030 [1]. Global energy related CO_2 emissions have been reported to be around 33 Gt in 2019, flattening after two years of increase and the record value of 2018. Renewable energy, mainly wind and PV, plays an important role in decreasing the CO_2 emissions from the power sector in advanced economies, also in IEA's NZE2050 scenario. The total emissions of the power sector have reached close to 13 Gt of CO_2 in 2019, a slightly lower level compared to 2018 (1.2% lower)[2].

According to the IEA, the global consumption of electricity has increased over the last decades from 7,623 TWh in 1980 to 24,739 TWh in 2018 [3]. IEA's NZE2050 scenario will lead to substantially larger electricity demand, up to twice the demand depending on a regional context [1]. Decarbonisation of the electricity sector therefore is of high importance, and PV as a clean and noiseless resource is one of the most desired options within the renewable energy resources [4, 5].

PV presently accounts for roughly 23% of the total of 2.54 TW globally installed renewable energy technologies [6], as a result of fast technological growth and increased investor confidence in PV installations [7, 8]. In fact, the year 2017 has been reported as a historic year for PV deployment globally as PV installed capacity has been the highest compared to any other power generation technologies, i.e., all conventional (fossil) fuels, and even other renewable resources [9, 7, 10]. As shown in Figure 1.1, solar PV is set to continue to be the fastest grower of all renewable energy sources in 2020, while its growth rate is decreasing [11]. Capacity growth 2020 was affected by the uncertainty coming from the Covid-19 pandemic. Nevertheless, in order to reach the proposed 500 GWp annual market in the NZE2050 scenario, annual market growth should be about 15%, as it is today.

PV electricity production is easy to measure for an individual power plant but much more complicated to compile for an entire country. This value depends on many factors like the time when the system is installed, the design and installation quality, e.g., the tilt and orientation angle for rooftop systems, or partial shading effects. For these reasons the electricity production is estimated for all countries around the globe [2]. It was reported that PV contributed roughly 3.0% to the

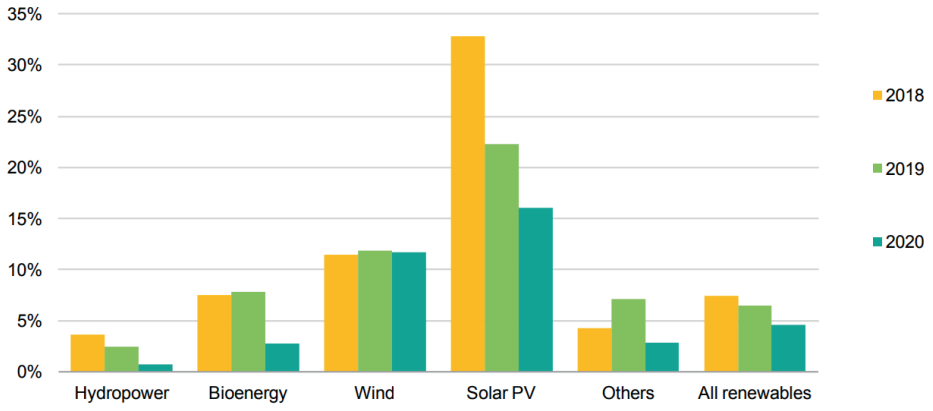

Figure 1.1 · Annual growth for renewable electricity generation by source, 2018-20 [11].

electricity demand in the world and to nearly 5.0% in the European Union.

1.2 PV system performance

Silicon solar cells have been introduced in 1954 with an efficiency of 6%, but today after almost 70 years of research and development the Si solar cells show a record efficiency of about 26.7% [12, 13, 14]. However, the performance of a PV system depends on the power output from the module, which is related to nonlinear cell characteristics varying with the ambient conditions [15, 16]. Analyses of real-world PV system energy yields reveal that the optimum performance is not always obtained and there are some aspects which can directly affect PV output energy, e.g., ambient temperature, partial shading, wind speed, soiling, humidity, air mass, etc. [17, 18]. The factors that affect the operation and efficiency of the PV systems are reviewed in [19, 20].

A study on the annual module performance over the European subcontinent shows that there are considerable differences in the relative performance at different geographical locations, with values ranging from 87% to 97% of the values that would be obtained if the module efficiency was always equal to that at Standard Test Conditions (STC)[1] [21]. The highest relative performance is found in regions with the lowest annual irradiation and it is due to the effect of typically low average ambient temperature in that region. As a further example, in [22]

[1]PV characteristics are measured at standard test conditions (STC), which are defined as 1000 W/m^2 irradiance, 25 ^{o}C cell temperature, and Air Mass (AM) 1.5 solar spectrum.

three types of solar PV module technologies, i.e., monocrystalline, polycrystalline and amorphous silicon have been investigated outdoors to check their performance variation with respect to the high relative humidity in Oman. Results show that with decreasing relative humidity the system efficiency increased. Also, it is found that for monocrystalline silicon the rate of increasing efficiency is higher. Another example is the performance of PV in a zero energy building in Singapore: results showed that the maximum generated power of rooftop arrays is close to their nominal capacity in some days, however maximum power for shaded arrays never reaches their nominal capacity during the year [23]. In another study in which PV performance in the Middle East and North Africa (MENA) region is investigated, it is shown that during the duration of the study, i.e., 192 days, the average efficiency reductions due to dust are 0.768%/day, determined using a multivariate linear regression model. Resulting energy and economic losses are 10.282 kWh/m^2 and 3.76 US\$/m^2, respectively [24].

Temperature

Once solar cells absorb sunlight, a significant portion of absorbed sunlight that cannot be converted into electricity instead generates heat, which heats up the module components and decreases the whole system performance [25]. This effect is expressed in so-called temperature coefficients, that detail the decrease of efficiency, and other module performance parameters. These are given in all data sheets of PV modules. Table 1.1 tabulates power temperature coefficient for different PV cell technologies. These values indicate how much the power decreases per degree change in the cell temperature. To this end, estimation of the solar cell temperature is essential. Various approaches are introduced for that and extensive reviews can be found in [26, 27, 28]. Ambient temperature is one obvious factor in this.

Table 1.1 · Power temperature coefficient of different PV cell technologies [29].

Technology	Temperature coefficient (%/K)
mono-crystalline silicon (c-Si)	-0.40
multi-crystalline silicon (mc-Si)	-0.45
amorphous silicon (a-Si)	-0.26
copper-indium-gallium-selenium (CIGS)	-0.36
cadmium-telluride (CdTe)	-0.25

Generally, there are three different modes for heat transfer, namely [14]:

- (i) Conductive heat transfer: this occurs when there is a temperature gradient within a solid. For a PV cell laminate of about 3 mm thickness [30], this

mode of heat transfer typically can be neglected.

- (ii) Convective: this occurs when there is a fluid in contact with a heated or cooled surface. According to the driving force behind fluid motion, two types of convection can be defined: natural convection and forced convection. Here, the fluid is ambient air.
- (iii) Radiative: this can be defined as the heat transferred by the emission of electromagnetic waves from a surface having a certain temperature. In [31], correlation methods for sky temperature calculations are studied.

To mitigate the disadvantageous thermal effect on PV performance, heat exchange with a cooler medium is one the primary options and this will provide an important improvement in system efficiency [32]. The idea of implementing water as a medium for cooling the panels will be discussed in this thesis in detail.

Non-uniform Irradiation

A fast variation in irradiation over the PV panel and cell surface will change the output power of the system and may lead to power instability for grid connected systems. Due to the nonlinear characteristics of the PV panel harvesting the optimum power both an appropriate maximum power point tracker (MPPT) algorithm is needed as well as a well designed system topology [17].

The MPPT is an algorithm which is developed to control the interface between the PV module and the load or grid. It usually is present in the inverter and/or converter to which PV modules are connected, and which provides AC energy to the grid. Developing this algorithm is an important issue, especially when a module does not receive uniform irradiation. The most familiar condition which leads to non-uniform irradiation coverage is called the partial shading condition (PSC). Partial shading may happen due to adjacent buildings or nature (trees), or it may happen due to inhomogeneous dust or dirt over the panel surface. Once the PSC occurs the output energy from cells within one module are not equal, and generally this condition is called a mismatch condition. To address this issue both the MPPT algorithm and the topology of the module and system should be studied, i.e. cell interconnections and/or module interconnections may need optimization. The MPPT algorithm should be able to find the global maximum of power because in the partial shading condition conventional PV modules that are designed with bypass diodes (BPD), the power-voltage characteristics will have multiple peaks instead of only one peak [16, 33].

Another method to mitigate the PSC in a PV system is to change the configuration of the PV system depending on (expected) PSC variation. PV system

configurations have been suggested to be changed via different interconnections of individual PV modules, which are typically from one of the following configurations: (i) series-parallel (SP), (ii) total-cross-tied (TCT), and (iii) bridge-linked [34, 35]. As power-voltage curves with multiple maxima occur because of the effect of bypass diodes, one way to mitigate partial shading effects is to divide the module into groups that consist of a small number of cells, while we note that the best option is to have one diode for each cell. Although more BPDs lead to shade-resilient modules [36], this can increase the number of local maximum peaks. Moreover, the efficiency losses with the BPDs are still significant [37].

For fast and dynamic PSCs a comparison between different MPPT method is discussed in [38]. However, for a precise approach in a dynamic PSC, it is required to implement a combination of different methods. We developed a smart shade resilient solar module which is discussed in detail in this thesis.

1.3 Floating PV

PV systems which are installed on water are called floating PV (FPV, floatovoltaics) systems. Although these are different from submerged PV systems the basics are similar. The basic principle of FPV is to profit from large existing water surfaces as installation location and profit from the water as a useful medium for managing a large plant of PV modules [39]. There is large Earth surface with intense solar radiation which would be perfect for PV system installations, however, if those areas would be used for PV systems they would not be available for other purposes, and land in industrialized zones is very expensive. Therefore, FPV has the potential to become the third most important type of PV in the world, following land-based and roof-top PV.

The first FPV system was built in Aichi, Japan [40, 41]. However, one year later another FPV system was built in California, USA over a water reservoir for a winery [41]. FPV deployment has grown slowly until 2014: the timeline of FPV system development is shown in Figure 1.2. Since 2014, interest in FPV systems is growing rapidly and even large FPV plants (i.e., with peak capacity in the tens and even hundreds of megawatts) are being installed or planned around the world [40].

FPV systems can be classified in three main groups: (i) canal top systems, (ii) reservoir/lake based floating solar systems, and (iii) offshore systems [42]. Thus, these systems could be installed over freshwater and ocean/sea surfaces. It is estimated that the potential energy which could be generated from freshwater installations is 6,069 TWh, which may cover about 25% of the entire world pro-

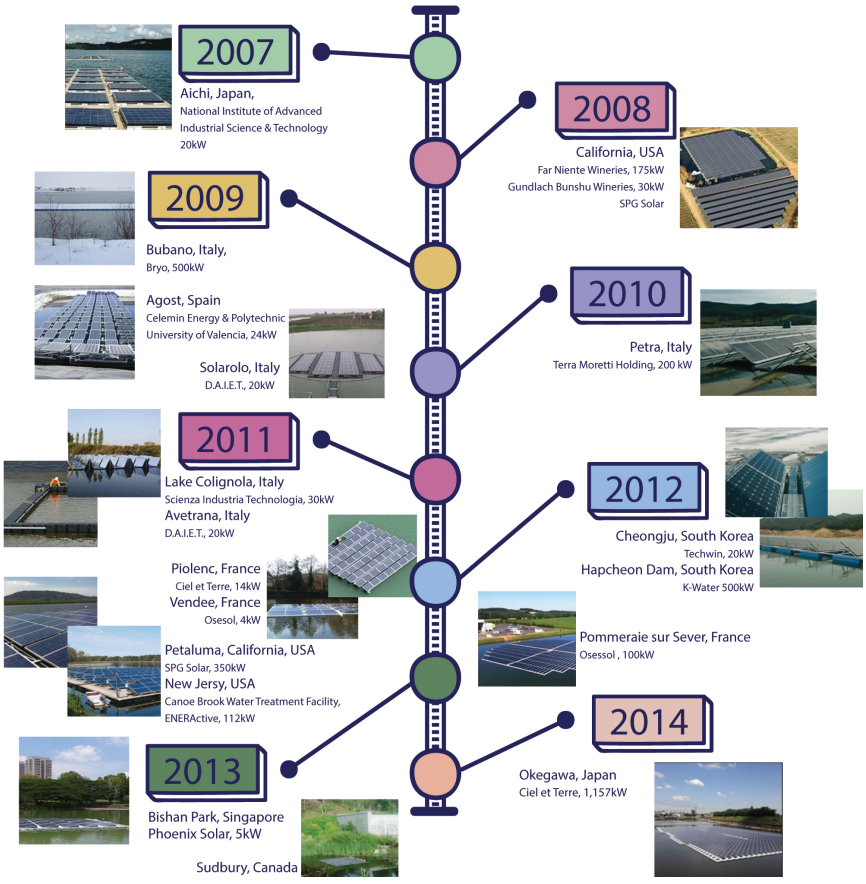

Figure 1.2 · Floating PV projects timeline between years 2007 and 2014 [41].

duction of electrical energy in 2015 which was 24,215 TWh [39, 43]. With about 70% of Earth's surface being water one may say that it is better to have offshore FPV systems rather than FPV systems over fresh water. However, we should note that although the open water surface compared to freshwater is very huge, there are two main challenges which should be taken into consideration: salt corrosion and wave impact. Nevertheless, both problems are not unsurpassable and can be managed, as shown in tests carried out by a research group in Malta [39, 44]. Note, in this thesis the salt corrosion issue is not covered.

The advantages of FPV

FPV system technology replaces the installation of photovoltaic power plants over valuable land. This is important for regions where land resources are scarce, land acquisition costs are high, or lands are undesirable for PV installations, e.g., when

PV conflicts with agricultural use. Thus, the main advantage of FPV systems is land saving, however they have some environmental and technical advantages as well. The environmental advantages consist of, but are not limited to: (i) integration with aquaculture, (ii) water quality improvement, (iii) reduced water evaporation. The noteworthy technical advantages are (i) higher energy yield, (ii) easier deployment, (iii) complementary operation for a hybrid energy resource such as with hydro power plants and (offshore) wind farms [45].

Environmental advantages

FPV systems can be added to aquaculture and fish farming [46] where it can replace the diesel generators typically used for auxiliary services, e.g., oxygen pumps, lighting [39]. An over-water system is a kind of PV system which is neither floating nor submerged, but the system is installed over water instead of land or roof, it can be fresh or shallow water. An example for over-water solar PV added to aqua-farming is in Coxi City in the Zhejiang Province in eastern China where a solar power station with a 200 MWp capacity has been installed above a fish farm, [47]. Shown in Figure 1.3, China's largest solar power station at a fishery site was officially connected to the grid early 2017. The solar modules were installed on the surface of the Zhouxiang and Changhe reservoirs in eastern China, roughly 150 km south of Shanghai [48]. Combining floating solar with fish farming is also explored in Norway and Singapore at near-shore conditions [40].

Figure 1.3 · China's largest solar power station at a fishery site, 2017 [48].

Other than over-water implementation of solar PV, the solar-powered artificial floating island (SAFI) was introduced by Chang et al. [49]. They add solar powered aerators to a conventional artificial floating island (AFI) and demonstrated

that a SAFI is able to improve the performance of the AFI by: (i) lysis of pollutants via raising dissolved oxygen to improve oxidation, (ii) homogenizing pH level and water temperature across water layers, and (iii) reducing electrical conductivity of water, which is more suitable for irrigation [50].

Also, as a result of FPV deployment a lower amount of sunlight will be reaching the water body, and thus algae growth is discouraged which leads to improvement of water quality [46, 40].

Evaporation represents a significant loss of water resources worldwide, as high as 40% [40]. In hot and dry climates, evaporation losses from water bodies represent a threat for the management of water resources, in particular for irrigation purposes as well as for power production [51]. A study in Spain showed that the FPV platform above the entire surface of a reservoir achieves an annual saving of 5,000 m^3 of water, which is 25% of the reservoir's storage capacity [52].

Technical advantages

An improvement of more than 10% in energy yield is reported in [53] and 12.96% is estimated through mathematical modeling [54]. There are plenty of reasons for an increase in overall efficiency of a FPV system compared to a land-based or rooftop PV systems.

One reason for this higher energy yield is the water cooling effect. As mentioned before, an increase in module temperature is the major loss factor for PV system performance, and decreasing this factor has a very important effect on energy yield. According to research in Singapore, the module temperature in FPV systems are generally 5 °C to 10 °C lower than similar modules mounted on rooftops, which helps to increase the energy yield [46]. It should be noted that the water temperature is not always lower than land temperature, e.g., in winter when the temperature on land may go below zero, sea temperature may be higher. As mentioned in [54] water temperature is not the only reason for cooling, both wind speed and relative humidity are also affecting apparent temperature for PV modules. Additionally, the wind speeds over open water tend to be larger than wind speed on land, thus also facilitating module cooling [40].

Another reason for higher energy yield is less partial shading on FPV systems. There are rarely obstacles present on water surfaces that cause shading and decrease the energy yield due to a shading effect [46, 40]. However, dust is another factor which leads to a decrease in energy yield, and while wind lifts dust and scatters it in the environment the deposited dust particles will result in partial shading and poor performance of PV cells and modules [55]. Another matter of importance are bird droppings, that lead to partial shading as well.

For systems which do not need complicated anchoring and mooring systems the process of installation of FPV is often simpler than compared to land-based systems [40]. Materials savings are possible as well, as 72% of the aluminum used in the PV industry is attributed to the construction and mounting facilities, while panel frames and other electronics need 22% and 6%, respectively [56]. On the other hand, floating systems need special designs to secure their floating on the water, but they generally do not require heavy equipment during construction [57].

Structural design

An installed floating PV system combines PV plant technology and floating technology. Depicted in Figure 1.4 [58], generally, FPV systems consist of the following components:

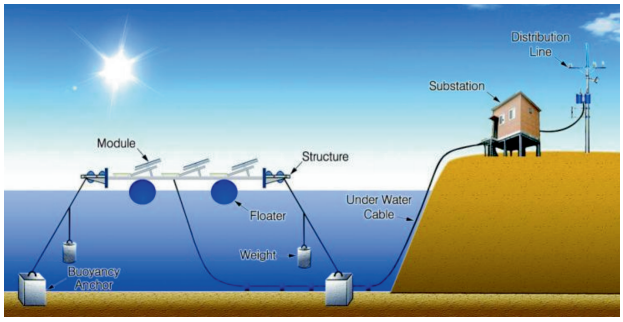

Figure 1.4 · Floating PV plants outline [58].

- Floating platform: this can be classified into two main categories: (i) pontoon, Figure 1.5a, (ii) raft, Figure 1.5b. A raft itself might be built out of either plastic, or plastic and galvanized steel, the latter option is useful to be assembled to construct a wide platform [39, 59, 58, 60]. In contrast with the raft structure, although pontoons are well-established and multipurpose technology, they are not good options for an optimum large scale FPV system [39]. Pontoons as rather expensive option are mainly used for small and medium size systems.

- Floats: Multiple plastic hollow floats which guarantee the buoyancy and stability of the FPV system. They are either made from MDPE (medium density polyethylene) or HDPE (high density poly-ethylene), which is known for its tensile strength, maintenance free, and UV and corrosion resistance. Glass fibre reinforced plastic (GRP) can also be used for construction of floating platforms [42, 52].

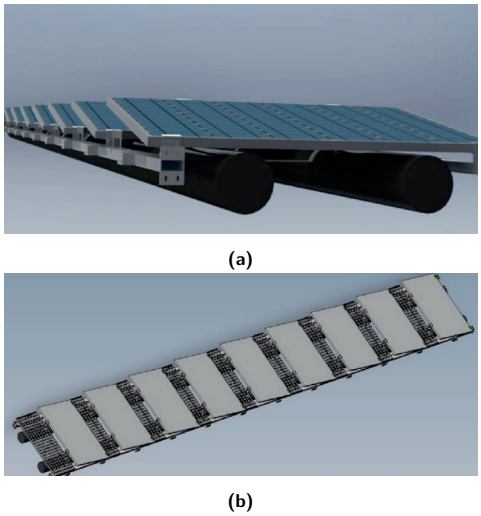

Figure 1.5 · (a) Pontoon with the steel pipes in black, (b) raft structure for a floating PV plant [61].

- Mooring system: Can adjust to water level fluctuations while maintaining its position in a southward direction [58, 42]. In the case of a floating solar system, the mooring system keeps the panels in the same position and prevents them from turning or floating away [62, 42].
- Ropes: Mooring system for floating platform can be done with nylon wire rope slings which can be tied to bollards on banks and lashed at each corner [52, 42].
- Anchoring system: Holds the floating cover and transmits horizontal forces to the sides of the reservoir.
- Solar PV module: PV modules implemented in FPV systems might be flat and rigid modules [61, 63] or thin film flexible floating PV [64, 65]. Almost in all of the FPV systems till now, Si crystalline solar PV modules are used [42]. However for metal corrosion especially over salty water new designs should be considered.
- Cables and connectors: Cables, MPPT converters, and other electronics needed in an FPV system need to be protected from humidity and water. For devices in an FPV system it should always be taken into consideration that the ingress protection (IP) code should be high enough. In [42] IP67 is recommended. Note that the first digit in the IP code refers to protection against solid particles, and the second one refers to protection against water and humidity. For instance in case of IP67, this means the device is both

dust tight and can be immersed in water up to 1 meter depth. For IP68 other than being dust tight the device can be immersed deeper than 1 meter. In many FPV systems, cabling is implemented above water [42]. However, with an appropriate design the system could have cables under water.

- Energy storage: Other than stand-alone PV systems which need an energy storage system, grid-connected systems in regions with high penetration of distributed generation, e.g., in European countries, energy storage may be required to reduce inadvertent stress on the grid, and provide an additional service for the regional grid [66, 61]. Although the main storage system for FPV is a battery pack, there are some other methods introduced, such as water/seawater pumped storage [67], and Compressed Air Energy Storage [61]. These non-battery storage systems could be also effective in decreasing the load on the transmission grid.

Offshore PV could be considered as the newest solution for PV deployment. For a country like the Netherlands, where land may have other priorities for use than solar PV deployment it is a potentially good solution to move solar modules from land to the North Sea surface. However, detailed studies on offshore PV performance installed over the North Sea is essential. These studies should comprise the effect of waves that may dynamically change the tilt and orientation of the module, and the water cooling effect that may change the panel temperature and affect the system performance ideally in a positive way.

1.4 Hybrid Power system

Regarding the aforementioned discussions FPV systems have a huge potential all over the world. However, these systems may take advantage of performing in a hybrid power system as well. For instance, hydro power or (floating) (offshore) wind energy systems could be very good options to combine with FPV systems. Adding FPV to the systems in which the grid connectivity, i.e. transmission lines, transformers, etc. is already present is more valuable.

In [68] the ability of a hydro power plant to act as a virtual battery for the FPV plant is studied. The hybrid power system in this research is designed such that in periods with high irradiation the FPV system generates electricity and transmits that to the grid directly, while the hydro power plant is idle. During this time either the reservoir accumulates (when there is an inflow stream) or just holds water that can be later used during times of low or absent solar irradiation. Thus, the reservoir performs as a storage system, which in this research is called a virtual battery. The feasibility of hybrid power systems consisting of hydro power

and FPV, resulting from the high flexibility of hydro power plant operation, is demonstrated in many studies. The focus on deploying FPV on hydro power reservoirs is due to the fact that they have lower potential cost integration, as grid connectivity is already available [68, 69]. However, the same argument is valid for other floating power systems.

The deployment of offshore wind farms has been ongoing since the 1990s, and has experienced a considerable growth in the last decade, especially in Europe [70, 71]. In [71] a hybrid system consisting of off-shore wind and off-shore floating PV is studied and the advantages of this combination are summed up as follows:

- The FPV system can fill up the required space between the turbine towers in the conventional off-shore wind farm. This combination increases the capacity density of the whole system. It follows that a combined offshore wind–solar farm can produce significantly more energy per surface unit area than an offshore wind farm. A recent study for the North Sea in addition shows economic advantages as well [45], with the concept of cable pooling as key: making use of an existing transmission cable that was designed for an offshore wind park only.

- In hybrid power systems with offshore wind and solar the intra-annual variation of the energy output reduces, thus addressing one of the advantages in marine renewable energy [71, 72]. Since there is often an anti-correlation between the solar and wind resource, it follows that hybrid systems combining FPV with offshore wind produce a smoother power output than conventional systems with either stand-alone wind or FPV. This is also a significant advantage in terms of power quality for the grid.

However, in these studies the effect of partial shading is not addressed and to this end, smart shade resilient modules have the potential to (further) improve the FPV energy yield.

1.5 Research question

The research gaps described above are addressed in this thesis by answering the following main research question:

> How beneficial would an offshore FPV system installed on the North Sea be?

We consider the following research questions:

1. How do weather conditions affect the performance of an offshore FPV system on open water, in particular, which parameters are of most importance?

2. How can an offshore FPV system on the North Sea be used by employing cable pooling within an existing offshore wind farm?

3. How can potential partial shading conditions be addressed in a generic way and how should a smart shade resilient module be designed?

In this thesis the feasibility and performance of an offshore FPV system on the North Sea will be discussed. The system is assumed to be installed about 50 km away from the shore of the Dutch side of the North Sea. Figure 1.6 shows the system under study.

Figure 1.6 · Offshore floating PV system under study (Photo courtesy of Oceans of Energy).

To provide a precise study many details are taken into consideration to establish the effect of wind, relative humidity, and dynamic albedo on FPV system performance. Moreover, for hybrid power systems such as an offshore wind-solar power system, the concept of cable pooling is explored, as well as potential partial shading issues. To limit effects of shading, we designed a smart module for mitigating power loss due to partial shading, which we denote as a smart shade resilient PV module. Development and testing of a prototype module will be described.

1.6 Thesis outline

Table 1.2 provides an overview of all chapters in this thesis, where and whether it has been published with contributing co-authors, and which research question they address.

In the first part of this thesis, **Chapter 2 to Chapter 4**, offshore FPV performance is simulated and results from the modeled system are compared with the land-based system. In **Chapter 2**, the performance of a 3.7 kWp PV system consisting of 12 panels, on land and at sea are modelled, simulated, and compared. To be able to have a fair comparison the effect of sea waves, wind speed and relative humidity is considered in this model. Sea waves are modeled in the frequency domain, using a wave spectrum. The irradiation on a tilted surface for a floating system is calculated considering the tilt angle that will be continuously affected by the sea waves. Moreover, the module temperature is estimated based on heat transfer theory and the natural cooling system for both floating and land-based PV systems. **Chapter 3** provides an additional detail to the offshore FPV system mathematical modeling. In this chapter the effect of dynamic albedo is considered. In most research the albedo value is considered as a fixed number however, this factor is a function of environmental aspects which are studied in detail in this chapter. In **Chapter 4**, a techno-economic analysis is performed to assess the feasibility of adding an offshore floating solar farm to an existing Dutch offshore wind farm in the North Sea, under the constraint of a certain fixed transmission cable capacity. The specific capacity of this cable, which connects the offshore park to the onshore grid, is not fully used due to the limited capacity factor of the wind farm. The principle of cable pooling allows to add floating solar capacity. The aim of the chapter is to find a generic methodology for such hybrid power system. In this generalization, the initial investment, system degradation, cable capacity, number of hours when each system is active, and energy price, are implemented to compute the optimum PV capacity regarding the net present value as an indicator for economic viability of the project.

In the second part of the thesis, **Chapter 5** and **Chapter 6**, a smart PV module is studied. The smart module is designed to mitigate shading effects. In **Chapter 5**, a smart PV module architecture is proposed for improvement of shade resilience for a PV module consisting of 60 silicon solar cells, which compensates the current drops caused by partial shading. The architecture consists of groups of series-connected solar cells in parallel to a DC-DC buck converter. The number of cell groups is optimized with respect to cell and converter specifications using a least-squares support vector machine method. A generic model is developed to simulate the behavior of the smart architecture under different shading patterns, using high time resolution irradiance data. Based on the design presented in **Chapter 6**, performance of a shade resilient smart module is studied under a dynamic shading pattern. Prototype hardware is designed and built to implement the proof of concept. The real time results of hardware testing shows that the smart module performs as expected and mitigates partially shaded conditions by

Table 1.2 · Overview of chapters

Chapter	Article title	Co-authors	Journal	Publication Status	DOI	Research Question
2	Simulation of performance differences between offshore and land-based photovoltaic systems	W. van Sark	Progress in Photovoltaics: Research and Applications 28 (2020) 873 - 886	Published, 2020	doi.org/10.1002/pip.3276	1
3	Effect of Dynamic Albedo Modeling on the Performance of Offshore Floating Photovoltaic Systems	W. van Sark	Solar Energy, Elsevier	Submitted, 2020	–	1
4	Pooling the cable: a techno-economic feasibility study of integrating offshore floating photovoltaic solar technology within an offshore wind park	D. Vaartjes, J. Meit, A. van Hoeken, M. Eberveld, H. Jonker, W. van Sark	Solar Energy, Elsevier	In press, 2020	–	2
5	Improvement of Shade Resilience in Photovoltaic Modules using Buck Converters in a Smart Module Architecture	A. De Waal, W. van Sark	Energies, MDPI 11 (2018) 250	Published, 2018	doi.org/10.3390/en11010250	3
6	Proof of Concept for a Novel and Smart Shade Resilient Photovoltaic Module	A. De Waal, W. van Sark	IET Renewable Power Generation 13 (2019) 2184 - 2194	Published, 2019	doi.org/10.1049/iet-rpg.2018.6127	3

extracting maximum power from each group of cells, regardless of the shading condition of other groups .

The results of this thesis are synthesized in **Chapter 7**. This chapter also explores the answers to the research questions, and presents several key recommendations for future research.

2

Simulation of performance differences between off-shore and land-based photovoltaic systems

This chapter is based on the paper:
S. Zahra Mirbagheri Golroodbari, Wilfried G. J. H. M. van Sark, *Simulation of performance differences between off-shore and land-based photovoltaic systems*, Progress in Photovoltaics, 28 (2020) 873 - 886.

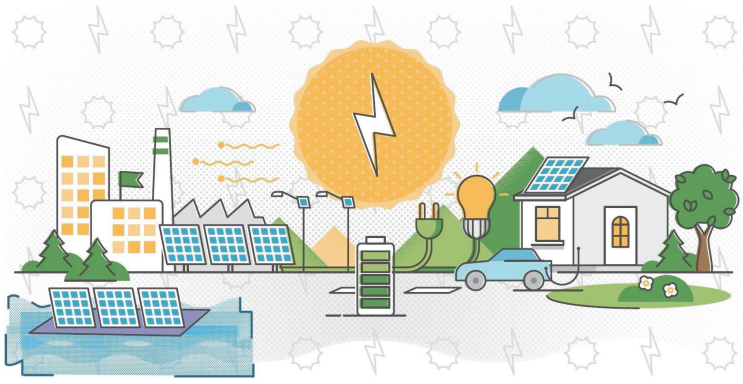

Abstract

The purpose of this study is to model, simulate, and compare the performance of a 3.7 kW photovoltaics system consisting of 12 panels, on land and at sea. To be able to have a fair comparison the effect of sea waves, wind speed and relative humidity is considered in this model. The sea waves are modeled in the frequency domain, using a wave spectrum. The irradiation on a tilted surface for a floating system is calculated considering the tilt angle that is affected by the sea waves. Moreover, the temperature is estimated based on heat transfer theory and the natural cooling system for both floating and land-based photovoltaic systems. Actual measured weather data from two different locations, one located at Utrecht University campus and the other one on the North Sea are used to simulate the systems thus making the comparison possible. Energy yield is calculated for these weather conditions. The results show that the relative annual average output energy is about 12.96% higher at sea compared to land. However, in some months this relative output energy increases up to 18% higher energy yield at sea.

2.1 Introduction

Photovoltaic (PV) solar energy generation capacity has been increasing significantly in the past decade. Its contribution to global electricity supply in 2018 was with 600 TWh almost 2.4%, which is predicted to increase to 22% in 2025, with potential up to 70% (40,000 TWh) in 2050 [73, 74]. However, development of large utility-scale PV system installations is limited due to (i) the cost and availability of land, (ii) decrease of efficiency at high operating PV cell temperature, and also (iii) potential environmental impact including biodiversity[59]. Therefore, a strong motivation is emerging for introducing both Building-integrated PV (BIPV) and floating PV systems, both on-shore and off-shore[75]. Offshore PV systems are categorized into installations (i) for ships, (ii) as floating PV (FPV), and (iii) on islands. In this study we will focus on off-shore FPV systems and their challenges.

Installation of FPV systems on water firstly saves land which may be otherwise implemented for agricultural use, and secondly the natural cooling potential of the water body may enhance PV performance, due to higher level of wind speeds off-shore, along with the presence of water. In addition to these advantages, a lower amount of obstacles causing shading loss and a lower amount of dust compared to land-based PV (LBPV) systems are further advantages. Moreover, due to the fact that more than 50% of the entire world population lives within 100 kilometers of an oceanic coast a FPV system installed on sea can be conveniently located to supply energy to these regions [76, 77]. Also, the extracted energy from FPV sys-

tems could be a great supply for off-shore platforms and ships, and would cancel out 3% global green house gas emission from them [76]. All this is leading to FPV systems becoming a hot topic of research at the moment.

FPV systems are categorized in four main groups with respect to their supportive structures [78]: (1) Thin-film: no strong pontoon is required as the supporting structure due to low weight of the thin film modules, (2) Submerged: it might be installed with or without pontoon, (3) Tilted arrays: needs rigid pontoons, and (4) a new approach using micro-encapsulated phase change material (MEPCM) based pontoon modules. In [41, 64] many different FPV systems which are built between 2007 and 2013 are reviewed. The common benefits from these installations were identified as (i) reducing water evaporation from the reservoir/pond on which these systems are located, and (ii) decreased algal growth. It should be taken into consideration that none of the reviewed research projects was installed at sea or ocean. The following seven different factors may indicate if a FPV system is designed optimally: *Modularity, Flexibility, Robustness, Safety, Optimum supportive structure size, Simplicity of installation, Minimizing the final costs* [79].

One of the FPV projects which fulfills all the mentioned factors above is the SERIS (Solar Energy Research Institute of Singapore) project located in Tengeh, Singapore [46]. In a comparison between the FPV system of this project and the typical rooftop mounted PV (RPV) systems in Singapore it was concluded that the module temperature of the FPV system is generally 5^oC to 10^oC lower than the RPV systems. As a consequence, the performance ratio is around 10% above that of the RPV system in Singapore. In a research project in South Korea a 100 kW FPV system is compared with normalized data from a 1 MW land based PV system on a close-by location [80]. The FPV system was installed over the Hapcheondam reservoir. It was assumed that the irradiation and temperature are the same on both locations. Their results showed that the average efficiency of the FPV system is 11% higher than the LBPV system in that location. In another research project, two FPV systems denoted as Floating, Tracking, Cooling, Concentrating (FTCC) systems are developed, one in Livorno and the other at a location near Pisa, both in Italy [63]. They developed a design to cool the panels using water, which increased the efficiency with 15%. It is concluded in this research that with their system considering the cooling system, reflection and sun tracker the FPV performs annually almost 30% better compared to a similar LBPV system.

A natural cooling system or water cooling has an important role in FPV system performance. In [81] performance of two submerged panels is compared with a reference panel in a nearby location, all panels are placed in horizontal position. The results show that the submerged panel at a depth of 4 cm below the

water level performed much better compared to the other two. Also, their results showed that the panel at a depth of 40 cm had the lowest output power for the same conditions, due to light absorption of the water body above the panel. The existence of water helps first to cool the panel and second to keep the temperature relatively constant.

In this chapter, we develop a model of a small FPV system consisting of 12 panels to be located on the North Sea. The modeling results will at a later stage be compared with the outputs from an experimental system installed on the North Sea. The panels are assumed to be placed on one steel pontoon which is fixed with four wire ropes to four buoys in its surroundings. The wire ropes limit the degree of freedom for the pontoon, in this way dealing with impact from sea waves. The following should be taken into consideration for modeling the FPV system: (i) Wind speed: the wind that blows over the sea area causes waves and also changes the apparent panel temperature ($T_{a,p}$) affecting the PV performance; (ii) Wave effect: each wave coming toward the pontoon has a certain energy that is able to cause movements of the pontoon and thus can change the orientation and the tilt angle of the panels located at the pontoon in a dynamical way; (iii) Relative humidity: like wind speed this factor affects $T_{a,p}$. The wave should be mathematically modeled based on these aspects, from which orientation and tilt angle can be calculated.

In this contribution, we will present a method using a flowchart. For its development, we need to study the wave characteristics which are used to derive a mathematical model for the dynamical tilt angle of the pontoon on which the panels are mounted. Both aforementioned issues are functions of wind data at sea. Then, we will compute the irradiation on the tilted surface. To be able to calculate panel performance both temperature and irradiation data is needed. Therefore, an equilibrium temperature is introduced which is computed from the estimated PV temperature and the fluid (water) temperature. Regarding the natural cooling system, the effect of wind and humidity is considered in the value of $T_{a,p}$ for the system. Finally, the energy yield is calculated. In the method section, all mathematical models and functions which are required will be described. In the simulation section, the above-mentioned flowchart is introduced and explained. In section 4 detailed results will be discussed. The chapter will be concluded in the last section.

2.2 Methodology

Modeling a FPV system needs to consider all effective above-mentioned aspects which are described in the introduction section. For calculating the energy yield

we need to compute the performance conditions, i.e., surface irradiation and cell temperature. In this study, we assume the FPV to be installed on a pontoon; therefore, both the tilt angle and the orientation may vary, albeit slightly. In this section, we will explain the method. First we will discuss the irradiation on the tilted surface. Instead of angular reflection losses, we are going to model the system more precisely and calculate the tilt angle in each time interval; because the angular reflection is a function of both latitude and tilt angle [82]. Then, we need to model the wave based on the wind characteristics blowing over the specific region at the North Sea. This is followed by a discussion on the heat transfer and the apparent temperature method. In this discussion the effects of both wind and humidity on temperature change will be considered .

Irradiation over tilted surface

Usually, there is one installed pyranometer for a group of panels, and global horizontal irradiation (GHI) is recorded. But, the irradiation on the tilted surface (GTI) determines the power generated by the PV panel. In this section we will describe how to calculate GTI using the tilt angle, GHI, and some other recorded data.

Global irradiation over the tilted surface (GTI) is calculated from Equation (2.1):

$$\mathrm{GTI} = \mathrm{DIR}_{\phi} + \mathrm{DIF}_{\phi} + R_{\phi} \tag{2.1}$$

where DIR_{ϕ}, DIF_{ϕ}, and R_{ϕ} are direct, diffuse, and reflective irradiance components, respectively, and $\phi = \{\beta, \gamma\}$, where β is surface tilt angle and γ is azimuth angle.
Direct tilted irradiance (DIR_{ϕ}) is calculated as follows:

$$\mathrm{DIR}_{\phi} = B_h \times r_b \tag{2.2}$$

where B_h is direct normal irradiance (DNI), and r_b is the direct irradiance conversion factor and calculated via

$$r_b = \max\left(0, \frac{cos\theta}{cos\theta_z}\right) \tag{2.3}$$

with

$$cos\theta = cos\theta_z cos\beta + sin\theta_z sin\beta cos(\gamma_s - \gamma) \tag{2.4}$$

where θ_z and γ_s are solar zenith and azimuth angles.

Many models have been developed to calculate diffuse tilted irradiance (DIF_ϕ). Their main difference is coming from the fact that these consider the diffuse irradiance being isotropically distributed over the sky dome or not. In this study we assume the anisotropic model called Klucher model (Kl). DIF_ϕ in this model is estimated via the following equation:

$$\mathrm{DIF}_\phi = D_h \times R_{dif}, \quad R_{dif} \geq 0 \tag{2.5}$$

where D_h is diffuse horizontal irradiance (DHI), and R_{dif} is calculated via the following formula:

$$R_{dif} = R_{d,LJ}\left(1 + f_K cos^2\theta sin^3\theta_z\right)\left(1 + f_K sin^3\frac{\beta}{2}\right) \tag{2.6}$$

where $R_{d,LJ}$ and f_K are the Liu-Jordan isotropic model diffuse irradiance transposition factors defined in Equation (2.7) and the Kluchers' conversion factor defined in equation (2.8), respectively[83].

$$R_{d,LJ} = 0.5 \times (1 + cos\beta) \tag{2.7}$$

$$f_K = 1 - \left(\frac{D_h}{G_h}\right)^2 \tag{2.8}$$

The classical approach to the modeling of the reflected irradiance (R_ϕ) assumes that reflected rays are diffuse and coefficients of reflection of the direct and diffuse rays are identical [84]. Therefore, R_ϕ is calculated from Equation (3.1):

$$R_\phi = \rho G_h R_h \tag{2.9}$$

where ρ is the foreground albedo = 0.06 calculated for the open ocean surface in American National Snow and Ice Data [85] and $R_h = 0.5(1 - cos\beta)$ is the transposition factor for ground reflection.

Wave model

Each wave can be seen as a combination of many small waves with different characteristics. Thanks to Joseph Fourier (1768-1830) for developing Fourier decomposition, all complex wave forms can be reproduced with an infinite sum, or series, of simpler functions. Mathematically, the complex wave $W(t)$ in the time domain can be described as in Equation (2.10):

$$W(t) = \sum_{k=1}^{\infty} A_k \cos\left(\omega_k t + \theta_k\right) \tag{2.10}$$

where A_k is amplitude (or Fourier coefficient), ω is angular frequency, and θ is phase angle.

Figure 2.1 shows a very simple example for wave decomposition; the wave in the bottom box, denoted by $f(t)$ in the figure, is the final wave which results from the summation of all single frequency waves (d_1 to d_8) with characteristics shown in the above subplots, where it can be seen that the wave frequencies are increasing from the first to the eight component. Note, A_k values differ slightly from each other. It is quite complicated to study the wave in the time domain, which is why in this study we discuss wave characteristics in the frequency domain. This so-called wave spectrum will be discussed in this subsection.

Wind is mainly responsible for wave generation at sea. A wave can be de-

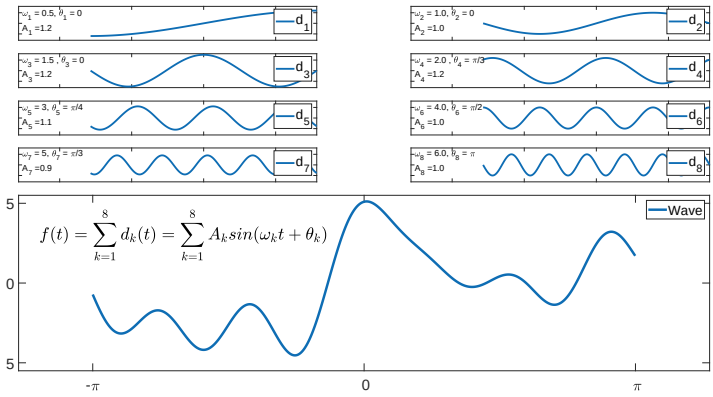

Figure 2.1 · Wave decomposition. The wave in the bottom box is composed of the waves shown in the eight top boxes.

scribed using frequency (f), wavelength (λ), Time Period (T), amplitude (a), and height (H), which is double the amplitude. In this model we considered the wave energy and its conversion to force. The amount of force from a wave may move the pontoon and is responsible for the tilted angle of the panel surface.
The energy density and power density of a harmonic wave can be calculated from the following equations [86]:

$$E_{Density} = \frac{\rho_{water} g H^2}{8}, \quad P_{Density} = \frac{E_{Density}}{T}, \tag{2.11}$$

where g is gravitational constant 9.81 m/s^2.
Following linear wave theory, wave energy per unit crest width for a specific wave is calculated as shown in Equation (2.12):

$$E = \frac{\rho g H^2 \lambda}{8} \quad \text{(J/m)} \tag{2.12}$$

Maximum power under ideal conditions is proportional with the calculated energy and per meter of the wave front and is equal to

$$P_{ideal} = \frac{1}{32\pi}\rho g^2 H^2 T \quad (\mathrm{W/m}). \tag{2.13}$$

However, obtaining these parameters for irregular waves or real waves should be calculated in a different way. To this end, the wave characteristics at fully developed open seas are generated by the so-called Joint North Sea Wave Project (JONSWAP) spectrum (JS) as shown in Equation (2.14) [87, 88]. This spectrum is a fetch-limited wind wave spectrum, which was developed for the North Sea by the offshore industry and is used extensively. The elevation $S(\omega)$ of (linear) fully developed open seas is described as

$$S(\omega) = \alpha \frac{g^2}{\omega^2} \exp\left[-5/4\left(\frac{\omega_p}{\omega}\right)^4\right] \gamma^r \tag{2.14}$$

$$r = \exp\left[-1/2\left(\frac{\omega - \omega_p}{\sigma\omega_p}\right)\right] \tag{2.15}$$

$$\alpha = 5.061\left(\frac{\omega_p}{2\pi}\right)^4 H_s\left[1 - 0.287\log\gamma\right] \tag{2.16}$$

where ω_p is peak spectrum angular frequency, γ is a peak enhancement factor and H_s is significant wave frequency, and $\sigma = 0.07$ for $\omega < \omega_p$ and $\sigma = 0.09$ for $\omega \geq \omega_p$.

For a real wave, which does not consist of only one sinusoidal wave with one frequency, the wave energy and maximum power, per unit meter, will be calculated as shown in Equations (2.17) and (2.18), respectively.

$$E = \rho g \int_0^\infty S(\omega) d\omega \tag{2.17}$$

$$P = \rho g \int_0^\infty v_g S(\omega) d\omega \tag{2.18}$$

where v_g is group velocity and for deep water conditions $v_g = g/2\omega$ [89].

With calculating this values and knowing the pontoon's weight and dimensions we are able to estimate the tilted angle for the pontoon as a function of time. Let us assume that the energy from wave is transferred to rotating kinetic energy which can rotate the pontoon e.g. about an axis in line with its length.

$$E_R = \frac{1}{2} I \omega_r^2 \tag{2.19}$$

where E_R is the rotating kinetic energy, I is moment of inertia, and ω_r is angular velocity for the pontoon. Figure 2.2 (a) and (b) depict the pontoon with length,

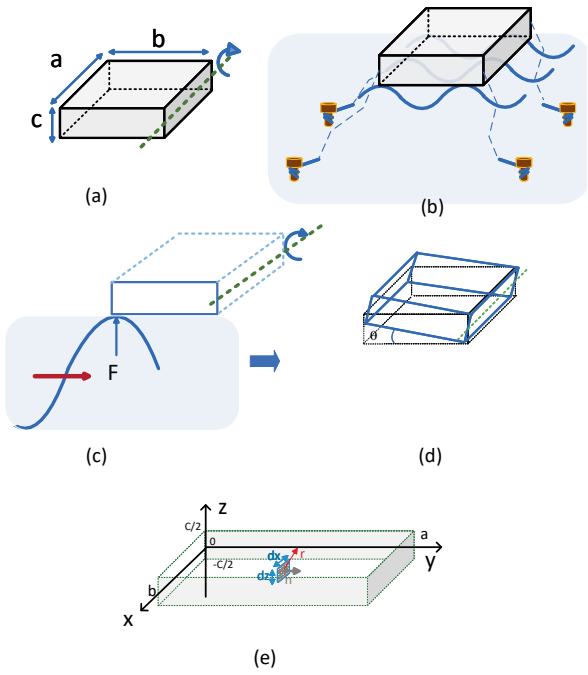

Figure 2.2 · (a) pontoon's dimension, (b) pontoon at sea level, (c) torque τ touches the pontoon and tries to rotate it around the shown axis, (d) pontoon rotated by θ, (e) coordinates and the pontoon dimensions.

width and height of a, b, and c, respectively. In the following, first we discuss how to calculate the moment of inertia and then explain how to use it for calculating the tilt angle.

The fundamental definition for moment of inertia is presented in Equation (2.20):

$$I = \int_0^m r^2 dm \tag{2.20}$$

where m is mass of substance, and r is the radius from the axis. It is assumed that the pontoon is symmetrical regarding the z axis shown in Figure 2.2 (e). Now, let us assume that the coordinates are chosen such that the point $z = 0$ is at the middle of the pontoon's height. A small rectangle inside the pontoon is considered while its normal vector is parallel with the y axis (rotational axis) and its radius from that axis is r. Regarding these assumptions the following proportional equation is valid:

$$\frac{dm}{dxdz} = \frac{m}{bc}; \tag{2.21}$$

Therefore, Equation (2.20) can be changed to

$$I = 2 \times I_{1/2} = 2 \times \int_0^b \int_0^{\frac{c}{2}} \frac{m}{cb} \left(x^2 + z^2\right) dzdx \tag{2.22}$$

By solving this, the moment of inertia for the described pontoon and the rotating axis is calculated as follows:

$$I = \frac{1}{3}mb^2 + \frac{1}{12}mc^2 \tag{2.23}$$

However, the moment of inertia for the pontoon such that the rotating axis is assumed to be on the x axis is calculated in Equation (2.24):

$$I' = \frac{1}{3}ma^2 + \frac{1}{12}mc^2 \tag{2.24}$$

For the assumed rectangular pontoon we have:

$$a = 5b \;\&\; a \gg c \;\&\; b \gg c \Rightarrow I' \simeq 5I \tag{2.25}$$

Therefore, comparing to rotation around the y axis, rotation around the x axis is negligible, for $a \gg b$. Thus, in this chapter, as shown in figure 2.2 (c), we only consider 2D motion for the pontoon and once the wave crest touches the pontoon, a perpendicular force makes a torque τ as in Equation (2.26):

$$\tau = \overrightarrow{F} \times \overrightarrow{r_1}, \;\; |r_1| = b \tag{2.26}$$

thus trying to rotate the pontoon clockwise, as shown in Figure 2.2 (d), which shows a change in tilt of θ.

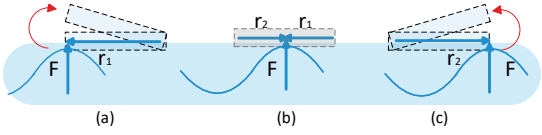

Figure 2.3 · Force and radius vector in different positions when wave crest touches for the first time (a) the left side (b) middle (c) right side, of the pontoon

Figure 2.3 shows that the wave forces move while the wave is moving forward. Therefore, for simplicity we assume that the wavelength and the width of the pontoon has the following relation:

$$\lambda \geq b \tag{2.27}$$

Hence, the variation for θ can be described as follows:

(a) When the crest of the wave touches the pontoon as shown in Figure 2.3

(a) torque is calculated as mentioned above in Equation (2.26), which causes the pontoon to rotate clockwise at an angle θ.

(b) The wave moves forward and touches the middle of the pontoon, this situation can be translated using linear algebra to the following equation,

$$\tau = \overrightarrow{F} \times (\overrightarrow{r_1} + \overrightarrow{r_2}),\ |r_1| = |r_2| = b/2 \tag{2.28}$$

due to the symmetrical characteristics of the pontoon the vectors $\overrightarrow{r_1}$ and $\overrightarrow{r_2}$ are in opposite direction and have equal magnitude so the total torque is equal to zero, which means that the normal vector for the pontoon at this scenario is $\pi/2$ and the pontoon makes an angle of $\theta = 0$.

(c) This scenario is similar to scenario (a), but the $\overrightarrow{r_2}$ is in the opposite direction which makes the pontoon to rotate anticlockwise at angle θ. In comparison with scenario (a), the absolute value of the tilt angle is the same, but the orientation of the pontoon is different.

Heat Transfer and Equilibrium Temperature

One of the main issues we need to consider in this model is the heat transfer for both systems. In the FPV system the pontoon is constantly in contact with the sea water, and in LBPV the platform which is assumed to be made exactly with the same material and in the same size is in contact with air. The heat transfer in two systems is discussed in this section. The equilibrium temperature should be calculated which is the temperature after heat transfer from the PV side to the fluid side which might be either water or air. Calculating this value needs some consideration for the PV side temperature which is not measured, therefore, we estimate the initial operating temperature of a PV cell using the Servant correlation [28], as follows:

$$T_c = T_a + \alpha\,(1 + \beta T_a)\,(1 - \gamma v)\,GTI \tag{2.29}$$

where T_a is ambient temperature, v is wind speed, and α, β and γ are constants that depend on the specific PV module structure. We need to solve the thermal equilibrium problem between the pontoon/platform and the fluid around these, following Equation (2.30), to calculate the equilibrium temperature:

$$m_p c_p \Delta T_p = m_f c_f \Delta T_f \tag{2.30}$$

where $m_{p,f}$ is mass of substance, $c_{p,f}$ is heat capacity and $\Delta T_{p,f}$ is temperature difference. Indices p, f denote pontoon/platform and fluid, respectively. The formula can be rewritten as, with T_{Eq} the equilibrium temperature:

$$m_p c_p (T_{PV} - T_{Eq}) = m_f c_f (T_{Eq} - T_f) \tag{2.31}$$

It should be taken into consideration that the PV panels after heat transfer perform at the equilibrium temperature, obviously in equilibrium $T_{Eq} = T_{PV} = T_f$. Note that due to the large heat conductivity of steel the heat transfer rate is fast.

Cooling Effect and Apparent Temperature

The recorded ambient temperature alone is not sufficient for performance analysis, as is evident from the Servant correlation [28] that also takes into account the effect of other weather conditions, e.g. wind speed (WS) and humidity. For example, in [21] the PV performance all over the world is studied considering the wind speed effect as well as ambient temperature and local irradiation. However, in this chapter a more generic overview is needed which is why the effect of humidity is also considered. We therefore use the so-called apparent temperature.

In [90], the following equation is implemented to incorporate the effects of air temperature, humidity and wind speed.

$$T_A = T_{db} + 0.33p_v - 0.7|v| - 4 \tag{2.32}$$

where T_A is apparent temperature (^oC), T_{db} is dry bulb temperature (^oC), v is the wind speed at 10 m height (m/s) and p_v is the vapour pressure of air (hPa) and can be computed from Equation (2.33) [91].

$$p_v = \exp\left(1.8096 + \frac{17.69D}{273.3 + D}\right) \tag{2.33}$$

where D(^oC) is Dew point temperature computed from the simple approximation formula,

$$D = T - \frac{100 - RH}{5}, \tag{2.34}$$

where RH is the relative humidity, where it is assumed that RH is larger than 50% [92]. In this work, the apparent temperature is implemented as the effective temperature rather than to consider not only bulb dry temperature, but wind speed and relative humidity as well.

2.3 Model set-up and simulations

Figure 2.4 depicts a flowchart according to which both systems are modeled. The flowchart has 14 numbered boxes, each of which represents a process, function or documented data. In this section, each box will be discussed and the mathematical model related to the box will be addressed regarding the method section. The implementation of the model is done using a MATLAB environment.

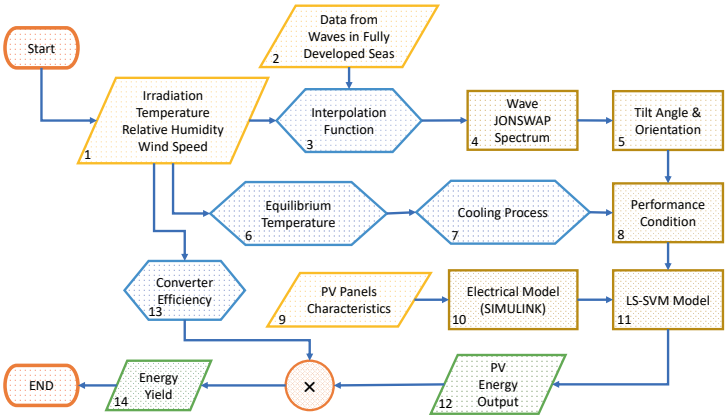

Figure 2.4 · Model Flowchart

Box1: Ambient Data

Measured ambient data are taken from both the Utrecht Photovoltaic Outdoor Test (UPOT) facility and the Royal Netherlands Meteorological Institute (KNMI) website, and are used to make the result statistically tangible [93, 94]. As mentioned in the flowchart, data in this part consists of (i) Irradiation (global horizontal, W/m^2), (ii) Temperature (^{o}C), (iii) Relative humidity (a.u), and (iv) Wind speed (m/s). The available recorded values for wind speed are maximum and minimum values per day. As we need data for our time resolution of one minute, an approximation is done. Assuming the fact that the data is normally distributed and by using the empirical rule in Equation (2.35), we approximated the data with the desired time resolution.

$$Pr\left(\mu - 2\sigma \leq X \leq \mu + 2\sigma\right) \approx 0.9545 \tag{2.35}$$

where X is an observation from a normally distributed random variable, μ is the mean of the distribution, and σ is its standard deviation.

Box2: Data from Waves in fully developed seas

For quantification of the waves using the wave model we implemented the recorded data in Table 2.1. This data specifies a variety of predicted wave properties for fully developed seas at different wind speeds [95]. With this table and with knowledge about the wind speed, the average period and wave height can be estimated with good accuracy.

Table 2.1 · Waves in fully developed seas [95].

Wind speed (km/hr)	Average Period (sec)	Wave height (m)
20	3.2	0.5
30	4.6	1.2
40	6.2	2.5
50	7.7	4.5
60	9.9	7.1
70	10.8	10.3
80	12.4	14.3
90	13.9	19.3

Box3: Interpolation function

Data tabulated in Table 2.1 is discreet and needs to be changed to a continuous function.Therefore, a cubic interpolation method is implemented to generate this continuous function.

Box4: Wave JONSWAP Spectrum

As discussed in the methodology section, modeling the wave in the time domain is complicated, so a frequency domain model is chosen. In this box, the wave JONSWAP spectrum is generated. The JONSWAP spectrum is mathematically shown in Equation (2.14). Using actual wind speed data using interpolation of data in Table 2.1 wave spectra are generated. It is assumed that the wave spectrum for every single day is unique. For instance, Figure 2.5 shows JONSWAP spectra for all days in August 2016, using wind speed data from KNMI [94]. Having a look at this figure can easily give us an intuitive impression about the days in which the sea is calm and we may have less strong waves, which is in fact the case for most of the days. However, later we will show how the waves change the tilt angle for the pontoon where the panels are assumed to be mounted on.

Box5: Tilt angle and orientation

By using the wave spectrum for each day the tilt angle can be computed using information in Section 2.2, and as a result, the irradiation over the tilted surface (GTI) is calculated, using the model of Section 2.2. Figure 2.6 shows the calculated tilt angle for the pontoon in the FPV system. The angles are estimated based on the wave spectrum shown in Figure 2.5. For most of the days, when the sea is calm, tilt angles vary only slightly between 0-3^o. For some days the tilt angles exceed 10^o, and only for one day tilt angles reach 20^o.

For calculating power in the i^{th} time window of the day we have the data

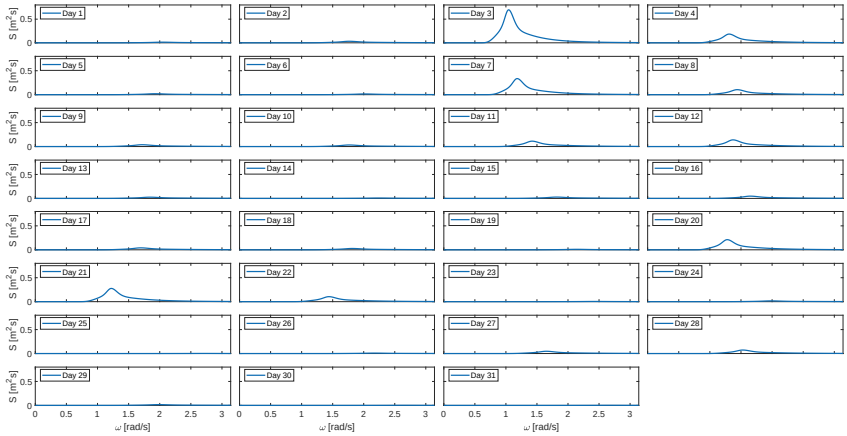

Figure 2.5 · JONSWAP spectrum (JS) for all days of August 2016.

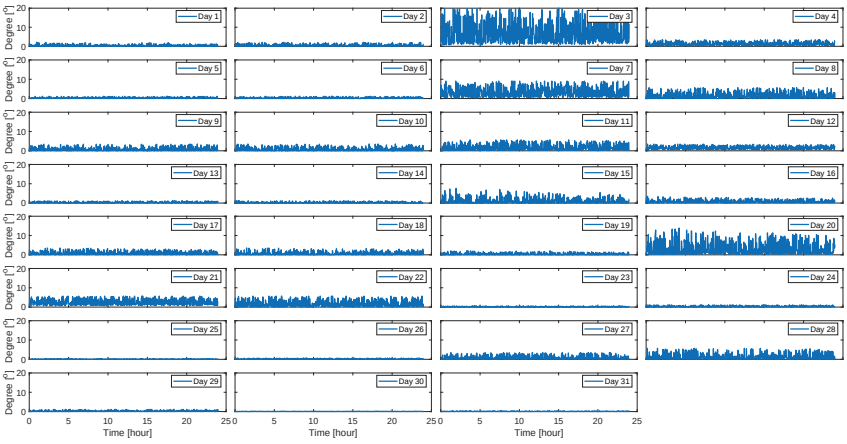

Figure 2.6 · The tilt angle of the pontoon for all days of August 2016.

set i consisting of panel orientation and tilt, which are considered in 2D such that the pontoon varies only between two orientations which are the south-east and north-west. The data set is shown in equation (2.36),

$$\left[\left(\beta_i, \gamma_1\right), \left(\beta_i, \gamma_2\right)\right], \tag{2.36}$$

where γ denotes the azimuth angle and $\gamma_1 = 135^o$ and $\gamma_2 = 315^o$ and β_i is the tilt angle in the i^{th} time period. This means that in this study, for each tilt angle we considered two azimuth or orientation values, one towards the southeast and other towards the northwest.

Simulating of this part is done by implementing the PV_LIB toolbox [96] in MATLAB environment.

Box6: Equilibrium Temperature

It should be taken into consideration that the cell temperature is different from the ambient temperature. Thus, as discussed in Section 2.2, the PV cell temperature is calculated using the Servant correlation, equation 2.29. The heat transfer process makes heat to transfer across the boundary of the system. Therefore, the PV equilibrium temperature should be calculated using Equation 2.31. Fluids around the pontoon/platform are infinite; however, in this study, we only consider that the same volume of the fluid is effective in heat transfer in a unit of time. For the FPV system, the sea water changes the PV initial operating temperature effectively as the pontoon is in touch with the water, but in LBPV the fluid is the air.

Box7: Cooling Process

As discussed in Section 2.2, to consider the effect of relative humidity and wind speed we impose the apparent temperature using Equation 2.32. Regarding the discussion in that section, the wind speed has a linear and relative humidity has a nonlinear relation with the apparent temperature.

Box8: Performance Condition

In this box we consider both GTI and working temperature for the PV panels. Regarding these information we can calculate the output power that is generated by the panels.

Box9: PV panels Characteristics

The PV panels characteristics at standard test conditions (STC), which are defined as 1000 W/m^2 irradiance, 25 ^{o}C cell temperature, Air Mass (AM) 1.5 solar spectrum, are shown in Table 2.2. This data is extracted from the specification data sheet of the used Exasun X60-BG310 module, which is a 310 Watt power module.

Table 2.2 · PV panel characteristics.

V_{OC} (V)	I_{SC} (A)	V_{MPP} (V)	I_{MPP} (A)	P_{MPP} (W)	Efficiency (%)	Temp Coeff Power (%/K)
39.9	10.3	32.9	9.4	310	19.35	-0.375

Box10: Electrical model

To simulate the behavior of the full PV system first one panel is modeled in MATLAB SIMULINK and a set of data with different irradiation and temperature is computed and recorded via this model. That is based on the PV panel characteristics and is used for data input to a least square support vector machine (LS-SVM) algorithm. In our system we use 12 identical panels, thus having a system capacity of 3.72 kWp.

Box11: LS-SVM model

The LS-SVM PV performance model is developed based on the LS-SVM algorithm [97]. The information extracted from the electrical model is used for training of the intelligent algorithm. The training data set of

$$T_{VM} = \{(x_1, y_1), \cdots, (x_l, y_l)\}, \tag{2.37}$$

where $x(j) = [G(j), T(j)]^{T_{VM}}$, $y(j) = P(j)$, $j = 1, \cdots l$ are recorded from the MATLAB SIMULINK file. In this data set, G is the irradiation level, T is ambient temperature, P is PV output power and j is the number of elements in the data set. The least square support vector machine uses the training data set (T_{VM}) to estimate the optimal nonlinear regression function $\hat{f}$, Equation (2.38), mapping the input data which are the performance conditions (from Box 8) to the PV output [98].

$$\forall\, G, T: \ [G \ \ T] \ \underset{\rightarrow}{\hat{f}} \ P \tag{2.38}$$

Figure 2.7 depicts performance of aforementioned module in wide range of irradiation and temperature. This PV performance is modeled implementing LS-SVM algorithm.

Box12: PV Energy Output

This box contains the computed output power for the panels in both systems. The time resolution of this data is one minute and thus the output energy is calculated.

Box13: Converter Efficiency

The modular system designed for this test subject is assumed to have one optimizer per panel. The optimizer used is a DC-DC converter, which is controlled controlled with a maximum power point tracking (MPPT) algorithm. The final voltage output in this system is assumed to be 24VDC on a DC Bus where all of the loads can be connected. The converter which is assumed to be used in this test set up is

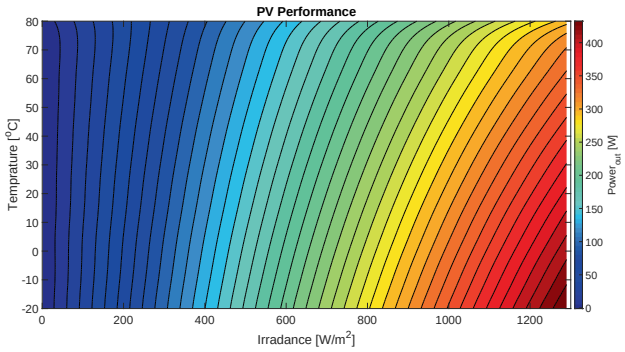

Figure 2.7 · PV performance model using LS-SVM

SmartSolar MPPT 75/15 designed by Victron Energy [99]. The optimizer controls the output power such that always the output power from each panel is maximum. However, its efficiency depends on temperature as well. The maximum efficiency for this specific optimizer is 98% according to its datasheet. A practical method for predicting the temperature-related power losses for buck converter is implemented in this study [100]. The apparent temperature for both systems is implemented in this model to estimate the converter efficiency at that level of temperature.

Box14: Energy Yield

Shown in equation (2.39), the energy yield is computed as a product of output power and converter efficiency.

$$E_Y = \left(\eta_{conv} \times \sum_{n=1}^{N} P_n \Delta t_n \right) \times 10^{-3} \tag{2.39}$$

where E_Y is generated energy in kWh, P_n is the power for the time resolution in W, Δt_n is the time resolution in minutes, N the total number of time intervals, n the time interval index, and η_{conv} is the converter efficiency. To calculate daily energy yield, $N = 1440$, as the time resolution is 1 minute.

2.4 Results and Discussion

In this section, we will review the results in detail. The results which will be discussed hereafter are extracted from the aforementioned model using the data for the year 2016. First, the effect of wind on both temperature and tilt angle will be shown and discussed. Thereafter, the equilibrium and apparent temperature results for both systems will be compared and then the tilt angle for the FPV system will be analyzed. Finally, the energy yield for both systems will be compared.

The data for LBPV is recorded at Utrecht University campus and data for FPV system from KNMI website [94, 93]. It should be noted that the irradiation data for December 2016 is not complete and is only available for 9 days.

At the beginning, let us compare both systems initially: Figure 2.8 depicts the average daily temperature at the locations where each FPV and LBPV systems are assumed to be installed, for the twelve months of the year. Also the water surface temperature for FPV at North Sea is included. It is clearly shown that while the air temperatures vary over a large range the sea water surface temperature changes only gradually every month. Minimum air temperature at LBPV is -1.1^{o}C which is roughly 4^{o}C higher than the minimum temperature at the FPV location. Similarly, the maximum air temperature is higher at the LBPV location. The minimum and maximum sea surface temperature are 1.8^{o}C and 16.7^{o}C, respectively. Figure 2.9 shows the apparent temperature at both locations for FPV

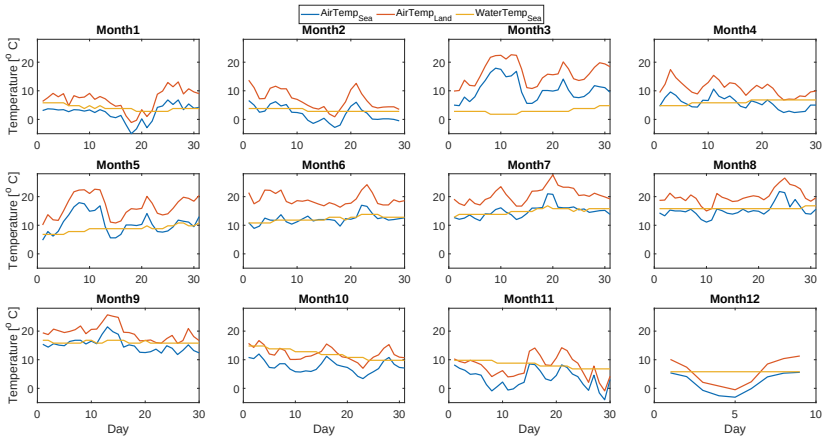

Figure 2.8 · Comparison of average daily temperature for both system locations and sea water temperature.

and LBPV systems. The apparent temperature at sea is much lower than on land due to a higher level of relative humidity in combination with higher wind speeds. As mentioned in section 2.2, the natural cooling system for FPV is driven by wind speed and relative humidity. From the data recorded in 2016, the average ambient temperature difference for the two locations is 5.05^{o}C, while the difference between the apparent temperature for the two locations is nearly twice larger at 9.36^{o}C. The average wind speed difference between two locations is 3.76 m/s also the relative humidity on average is 8.1% higher in the FPV location.

Figure 2.10 depicts equilibrium and ambient temperature for both FPV and LBPV systems, also it shows the sea surface temperature. The box plots confirm that all temperatures follow a similar trend during the year. However, the dif-

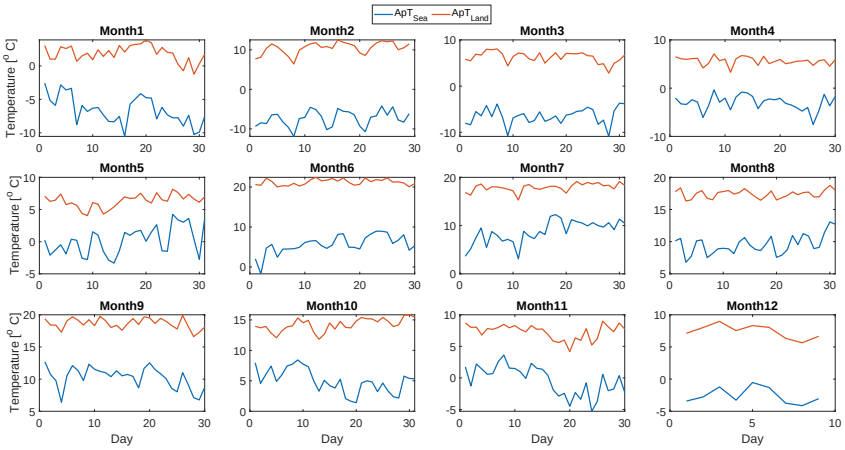

Figure 2.9 · Apparent air temperature for both systems.

ference between the equilibrium and ambient temperature for FPV compared to LBPV system, is significant. As shown in this figure, the sea surface temperature

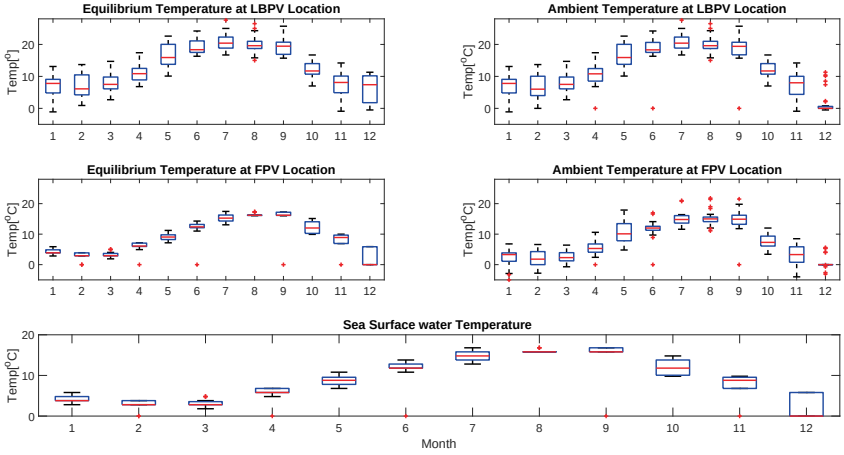

Figure 2.10 · Equilibrium and ambient temperature for both systems, and sea surface temperature, for the year 2016.

is close to the PV system equilibrium temperature. Regarding the heat transfer theory that is discussed in Section 2.2, Equation 2.31, this indicates how close the equilibrium is to the fluid temperature. As mentioned before, to limit the fluid with infinity volume, it is assumed that the effective volume of the fluid is as large as the platform/pontoon volume. To this end, the substance density and heat capacity of water, air (at sea level) and steel is compared in Table 2.3. Considering Equation 2.31 and the table context, it is clearly shown that the equilibrium

temperature in the FPV system is much closer to the sea surface temperature and in the LBPV system it is much closer to the PV temperature itself. However, the effect on the equilibrium temperature of wind and humidity is clear. Note that the variation of the equilibrium temperature for the FPV system is much smaller than the variation for the LBPV system (the boxes are much narrower).

Figure 2.11 shows the wind speed, relative humidity and also the relative dif-

Table 2.3 · Substances heat characteristics.

Substance	Water	Air	Steel
Density [kg/m^3]	1025	1.225	8050
Heat Capacity [J/K]	4200	1005	490

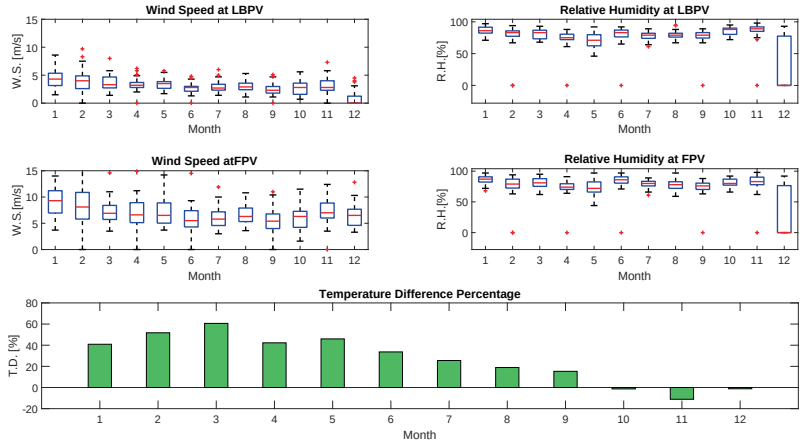

Figure 2.11 · Wind speed, relative humidity, and relative difference of equilibrium temperature for both systems, for the year 2016.

ference between equilibrium temperatures $\Delta T_{Eq} = (T_{Eq,LBPV} - T_{Eq,FPV})/T_{Eq,FPV}$, for both systems. Although the relative humidity is not significantly different for both systems, the wind speed is more variable for FPV system compared with the LBPV. It is shown that excluding three last months of the year, the equilibrium temperature considering the wind and humidity effect is much lower for the FPV system, the average of temperature difference is 28.5% when a maximum of 82%. For computing the energy yield from the FPV system the GTI calculation is also required. As discussed in Section 2.2, the irradiation should be calculated regarding the tilt angle that is zeros for LBPV system and changing due to the waves for FPV system. Figure 2.12 shows both estimated average tilt angle and average wind speed in 2016, monthly. It is depicted how the wind speed changes the maximum tilt for every month. The average tilt angle has more variation during the

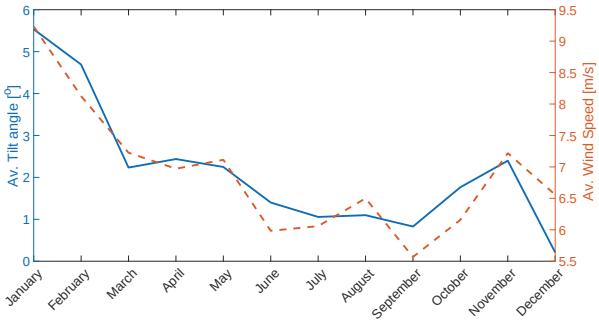

Figure 2.12 · Average tilt angle for the FPV system and the average wind speed for year 2016.

winter season, when the irradiation is much lower than other times of the year.

Energy yield is possible to be computed regarding both performance conditions, i.e. GTI and equilibrium temperature for both systems. Using the wave spectrum values for all days of year 2016 we can compare the GHI and the GTI of the FPV system for the whole year 2016 (we only had data for 9 days in December 2016), see Figure 2.13. The left axis in this figure shows both daily averaged GTI and GHI of the FPV system; the right axis shows the wind speed. It can be inferred from this figure that an increase in the wind speed can increase the GTI. This effect is more tangible in colder months of the year when the solar elevation angle is smaller.

Figure 2.14 shows the bar chart of the output energy for the year 2016 on the

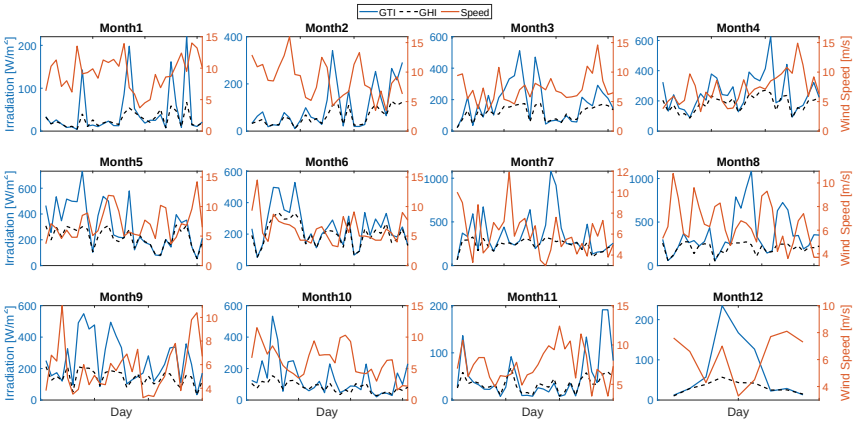

Figure 2.13 · Daily averaged GHI and GTI in comparison to wind speed.

left axis, and on the right axis the relative difference between output energy from

two systems on land and at sea is shown, ($[E_{FPV} - E_{LBPV}]/E_{LBPV}$). It illustrates that the FPV system in all months performs better compared to the land-based system. The highest difference is seen for the month June where the energy yield of the FPV system is 6% higher than the energy yield of the land system. In January both systems perform quite similarly and the relative difference is only almost 2%. On average, regarding this model and the 2016 data the FPV system performs 3.49% better than the LBPV system. This result is lower than reported in literature, which was 10% [46] and 11% [80]. The annual yield for the LBPV system is 4.43×10^3kWh (1192 kWh/kWp) which is 12.96% less than FPV system which yield 5.01×10^3kWh (1346 kWh/kWp) in this year. However, it should be taken into consideration that the GHI is not similar in both locations and as depicted in Figure 2.14, GHI is about 8.54% higher in FPV location. Note further, that the year 2016 was an exceptional year with a 5% higher annual irradiance than the 30-year average[94].

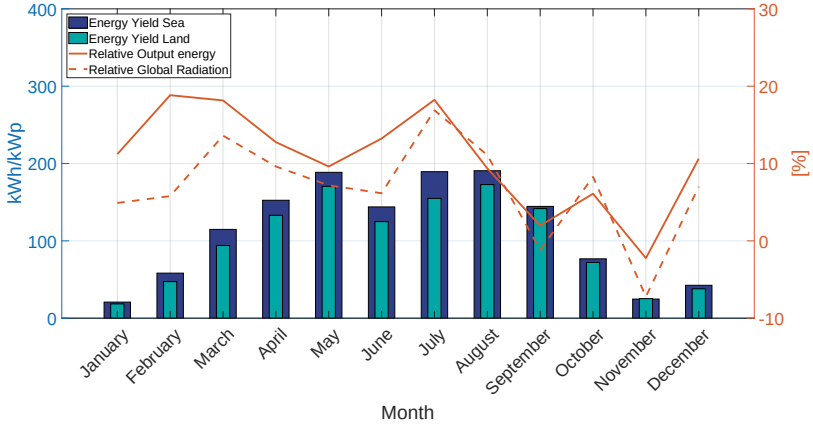

Figure 2.14 · left axis, normalized energy yield from two different systems. right axis, Relative output difference from two systems.

To account for differences in irradiation, we calculate the performance ratio, using the following equation:

$$PR = \frac{Y_f}{Y_r} \tag{2.40}$$

where Y_f is final system yield from PV panel and Y_r is reference yield.
Figure 2.15 depicts PR for both systems, the average PR for the LBPV during the year 2016 is 81.66% and for FPV is 3.15% more and equal to 84.75%. For most months PR values differ, and this reflects the temperature differences that occur in both systems.

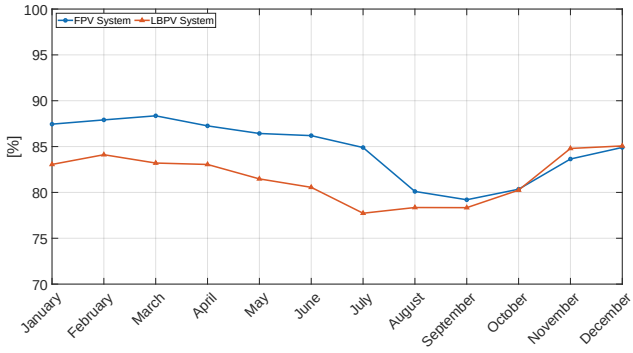

Figure 2.15 · Performance ratio for both FPV and LBPV systems

Mathematical modeling and simulations implementing actual weather data for comparison between two similar PV systems on land and sea show that different ambient conditions affect the energy yield of the systems. Although the wind speed simultaneously changes the tilt angle and as a result the panels are not always positioned at the optimum angle, the existence of water around the pontoon is a big advantage for improving the efficiency, as the panel temperature is lower and more constant as well. We do note that the effect of dust on the LBPV system and salinity of water is neglected in this model for simplicity.

2.5 Conclusion

A mathematical model for both land and sea PV systems has been developed in this work. To this end, both actual irradiation and temperature data is used for the modeling. A floating PV system is characterized by constantly varying tilt angles, in contrast to a land-based system (assuming no tracking), which complicates energy yield modeling. A model has been developed that allows the calculation of the tilt angle variation based on wave characteristics and how these are influenced by wind speed leading to a wave spectrum analysis. Moreover, for calculating the temperature of the PV systems both heat transfer theory and apparent temperature method are implemented to estimate an accurate equilibrium temperature, where the effect of wind speed, relative humidity and presence of water is taken in to account.

Our simulations show that the energy yield of both systems differs predominantly as a result of lower temperatures. We found that the system at sea performs 12.96% better on average on an annual basis than the land based system.

Acknowledgment

The authors gratefully acknowledge fruitful discussions with Brigitte Vlaswinkel and Allard van Hoeken (Oceans of Energy), and Anne de Waal (UU). This work is partly financially supported by the Netherlands Enterprise Agency (RVO) within the framework of the Dutch Topsector Energy (project Comparative assesement of PV at Sea versus PV on Land, CSEALAND).

3

Effect of Dynamic Albedo Modeling on the Performance of Offshore Floating Photovoltaic Systems

This chapter is based on the paper:
S.Z. Mirbagheri Golroodbari, W.G.J.H.M. van Sark, *Effect of Dynamic Albedo Modeling on the Performance of Offshore Floating Photovoltaic Systems*, Solar Energy (submitted).

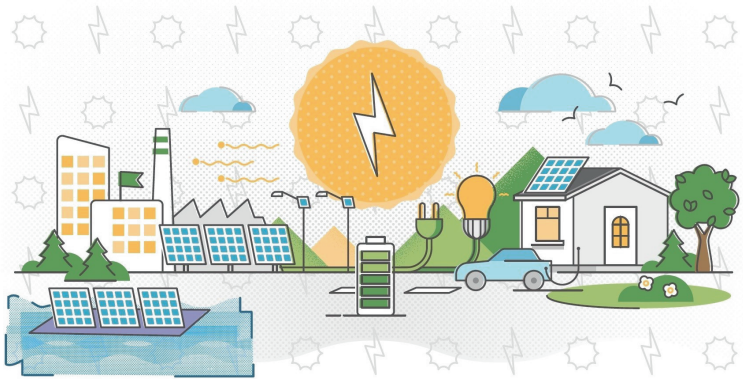

Abstract

In this chapter we quantify the effect of dynamic albedo on the generated energy of a floating offshore photovoltaic system, which is assumed to be installed at the North Sea. Albedo is modeled dynamically as a function of solar irradiation, wind speed and solar zenith angle at an hourly time resolution. The energy output of a floating offshore PV system is compared for two scenarios comparing (i) constant albedo and (ii) a modeled dynamically varying albedo. The quantified results show that the system performance in case of a varying albedo is larger by about 3.04% compared to using a constant albedo.

3.1 Introduction

Solar rays pass through the atmosphere and clouds before arriving at a surface on Earth. In addition, the environment surrounding such a surface affects the radiation measured on that surface. To determine the irradiance that is impinging on a photovoltaic (PV) solar panel, both direct and indirect radiation must be taken into account, with direct being radiation that passes in a straight line through the atmosphere to the panel and diffuse radiation that has been scattered by atmosphere and clouds. Figure 3.1 illustrates the various components of solar irradiance, including reflection from objects in the environment of the panel. In this chapter we focus on reflection from ocean surface water in offshore floating systems [39].

The classical approach to the modeling of reflected irradiance (R_ϕ) assumes that

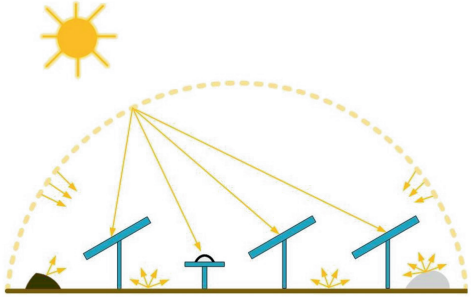

Figure 3.1 · Solar irradiance components, direct, diffuse and reflection.

reflected rays are diffuse and coefficients of reflection of the direct and diffuse rays

are identical [101, 54]. Therefore, R_ϕ is calculated from Equation (3.1):

$$R_\phi = \alpha \times G_h \times R_h \tag{3.1}$$

where α is the surface albedo and $R_h = 0.5(1 - cos\beta)$ is the transposition factor for ground reflection, with β the panel tilt angle [101]. In most assessment of PV energy yield, albedo is kept constant. In this research we aim to quantify the variation of the value of α for the ocean surface, which provides more accurate modeling of energy yield of floating offshore PV systems [54].

Albedo is defined as a non-dimensional, unitless quantity that indicates how well a surface reflects solar energy. In the oceans, the fraction of solar radiation penetrating the subsurface is controlled by the ocean surface albedo (OSA)[102]. Despite its importance, OSA is a parameter that receives insufficient attention from both an observational and modeling point of view and in most studies, it is assumed to be a constant (OSA$\simeq$ 0.06) for the open ocean surface [103]). It is indicated that the solar zenith angle (SZA) is the most prominent driving parameter for OSA, for instance in [104] LMDZ model for albedo is developed following the equation 3.2,

$$\mathrm{OSA}(\zeta) = \frac{0.058}{\mu + 0.30} \tag{3.2}$$

where ζ is solar zenith angle and $\mu = cos(\zeta)$.

Consequently for this model, OSA varies between 0.0446 for a sun at zenith and 0.193 for a sun at the horizon. However, it should be noted that there are some other parameters on which the OSA depends such as wavelength of ocean surface roughness, and atmospheric and oceanic properties [105, 102].

Albedo commonly refers to the "whiteness" of a surface, with 0 meaning black and 1 meaning white. In the oceans, the fraction of solar radiation penetrating the subsurface is controlled by the ocean surface albedo (α_{OSA})[102]. Therefore, we separate the ocean surface albedo into the direct ($\alpha_{O,DIR}$) and diffuse ($\alpha_{O,DIF}$) contributions as shown in equation (3.3)[105]:

$$\alpha_{OSA} = \alpha_{O,DIR} + \alpha_{O,DIF} \tag{3.3}$$

Given the wind speed, surface roughness and zenith angle $\alpha_{O,DIR}$ and $\alpha_{O,DIF}$ can be calculated explicitly, which will be explained in the following sections. A mathematical model developed by Cox and Munk [106] is implemented in this research which estimates a function to parameterise the mean contribution of multiple reflective facets at the ocean surface. This polynomial function is given in the section 3.2.

In this chapter we will study the effect of wind speed on surface ocean albedo.

Gordon and Jacob [107] separate the effect of wind speed in two different and opposite effects: (i) the albedo of the surface decreases only slightly with increasing wind speed which leads to increased roughness, (ii) increasing the wind speed over the ocean, however, results in another process which increases the surface albedo: the formation of white caps. The effect of wind is not a simple linear effect. Therefore, we need to study in more detail how the variation in the wind speed could change the surface ocean albedo and how this affects energy yield estimations for offshore PV, as is described earlier [54].

In this chapter, first we will discuss the mathematical model for quantifying the surface ocean albedo value in section 2. In section 3 we will compare the results from this model to the results implementing a constant albedo value. Finally, we will wrap up the chapter with a conclusion in section 4.

3.2 Methodology

The global irradiation on a tilted surface (GTI) determines the power generated by a PV panel. It is calculated using equation (3.4) [54]:

$$GTI = DIR_{\phi} + DIF_{\phi} + R_{\phi,\zeta} \tag{3.4}$$

where DIR_{ϕ}, DIF_{ϕ} and $R_{\phi,\zeta}$ are direct, diffuse, and reflective irradiance components, respectively, and $\phi = \{\beta, \gamma\}$ where β is surface tilt angle and γ is azimuth angle, and ζ is solar zenith angle.

As mentioned in the introduction the classical approach to model $R_{\phi,\zeta}$ assumes that reflected rays are diffuse and coefficients of reflection of the direct and diffuse rays are identical [84]. Therefore $R_{\phi,\zeta}$ is calculated using equation (3.1).

Albedo $\alpha \in [0, 1]$ is a non-dimensional, unitless quantity that indicates how well a surface reflects solar irradiance. It is reported that albedo for an open ocean α_{OSA} depends on a number of parameters, which include several atmospheric and oceanic properties, solar zenith angle (ζ), ocean surface roughness, which itself is a function of wind speed, and optical wavelength [105]. The incident solar radiation namely direct and diffuse, is first influenced by the presence of whitecaps, which exhibits different reflective properties from seawater. Then, the reflective properties of the uncapped fraction of the sea surface are determined separately for direct and diffuse incident radiation [102]. In this research for simplicity we neglect the effect of the subsurface or the ocean interior.

Whitecaps

The fraction of whitecaps (f_{WC}) can be generated from the disturbance coming from the breaking of waves due to the wind. This turbulence generates the foam at the sea surface which can change the albedo considerably [108, 102]. In this work, we use equation 3.5 to formulate the f_{WC} as a function of wind speed (v [m/s]) at height of 10 m above the sea surface [109].

$$f_{WC}(v) = 3.97 \times 10^{-2} \times v^{1.59} \quad | \quad v \in [2 \quad 20] m/s \tag{3.5}$$

Equation 6.18 is proposed in [110] as a polynomial relationship for solar spectral dependence of $\alpha_{f_{WC}}$.

$$\begin{aligned} \alpha_{f_{WC}}(\lambda) = 0.5 \times \frac{1}{100} \Big[& 60.063 - 5.127 \ln \alpha_W(\lambda) + 2.799 \left(\ln \alpha_W(\lambda)\right)^2 \\ & -0.713 \left(\ln \alpha_W(\lambda)\right)^3 + 0.044 \left(\ln \alpha_W(\lambda)\right)^4 \end{aligned} \tag{3.6}$$

where $\alpha_W(\lambda)$ is the absorption coefficient of clear water in m^{-1}. In this research the $\alpha_W(\lambda)$ values which are published in both [102, 110] are used for $\lambda \in [400 \quad 2400]$ nm.

The Roughness of the Sea Surface

An absolutely calm sea surface reflects the sun like a mirror at the horizontal specular point. However, usually there are thousands of "dancing" highlights. At each highlight there is a water facet, possibly quite small, which is so inclined as to reflect an incoming ray from the sun towards the observer [106]. Regarding this fact the roughness of the sea surface, so called σ, is estimated in equation (3.7) [106]. showing the dependence on wind speed.

$$\sigma^2 = 0.003 + 0.00512v \tag{3.7}$$

Fresnel surface albedo for Direct and Diffuse components

The major components of α_{OSA} are described by equations 6.19 and 6.20 which are the contribution of Fresnel reflection at the ocean surface.

$$\alpha_{O,DIR}(\lambda, \zeta, \omega) = r_F(n(\lambda), \mu) - \frac{r_F(n(\lambda, \mu)}{r_F(n_0, \mu)} \times f(\mu, \sigma) \tag{3.8}$$

where $\mu = \cos(\zeta)$, with ζ the incident angle, n is the wavelength dependent refractive index of seawater, r_F is the Fresnel reflectance for a flat surface and $f(\mu, \sigma)$ is a function that accounts for the distribution of multiple reflective facets at the ocean surface estimated in the visible spectrum (VIS). Values for variable $n(\lambda)$ are

extracted from [102, 105]. Also, it is assumed that $n_0 = 1.34$ calculated from the refractive index of seawater averaged in the VIS. Function $f(\mu, \sigma)$ is found from multiple regression in [105] as follows:

$$\begin{aligned} f(\mu,\sigma) = \big(&0.0152 - 1.7873\mu + 6.8972\mu^2 - 8.5778\mu^3 + 4.071\sigma - 7.644\mu\sigma\big) \\ &\times \exp(0.1643 - 7.8409\mu - 3.5639\mu^2 - 2.3588\sigma + 10.0538\mu\sigma) \end{aligned} \tag{3.9}$$

A simple expression for the calculation of α_{DIF} is implemented in this research using only surface roughness and refractive index as variables [105]:

$$\alpha_{O,DIF}(\lambda,\sigma) = -0.1479 + 0.1502n(\lambda) - 0.0176n(\lambda)\sigma \tag{3.10}$$

Considering the components of total OSA, i.e. $\alpha_{O,DIR}$ and $\alpha_{O,DIF}$, we may calculate the total OSA using the ratio of direct and diffuse irradiation:

$$\alpha_{OSA} = f_{DIR}\alpha_{O,DIR} + f_{DIF}\alpha_{O,DIF} \tag{3.11}$$

with f_{DIR} and f_{DIF} the direct and diffuse fractions in GTI, respectively. Like $\alpha_{O,DIR}$ and $\alpha_{O,DIF}$ these are wavelength dependent and are shown in equation 6.21. For simplicity in this research the contribution of the ocean interior reflectance to the ocean surface albedo is neglected [102].

$$\begin{aligned} \alpha_{O,DIR}(\lambda,\zeta,v) &= \alpha_{O,DIR} \times (1 - f_{WC}(v)) + f_{WC}(v)\alpha_{f_{WC}}(\lambda) \\ \alpha_{O,DIF}(\lambda,\zeta,v) &= \alpha_{O,DIF} \times (1 - f_{WC}(v)) + f_{WC}(v)\alpha_{f_{WC}}(\lambda) \end{aligned} \tag{3.12}$$

Regarding equation (6.21) the effect of whitecaps on the direct and diffuse albedo is formulated with $(1 - f_{WC})$ as coefficient which means when f_{WC} is increasing the effect of whitecap on albedo is becoming dominant. Finally, the sea surface albedo α_{OSA} is calculated using equation (3.3).

3.3 Results and discussions

In this section we will present and review the results in detail. The results which will be discussed hereafter are extracted from implementing the albedo model discussed in this chapter in the mathematical model developed in [54]. The mathematical model for the offshore floating PV system considers the following variables: (i) irradiation , (ii) wind speed, and (iii) relative humidity. For this model we considered variable tilt angles implementing Joint North Sea Wave Project (JONSWAP) spectra, as detailed in [54]. Data at hourly time resolution in this chapter is from the Royal Netherlands Meteorological Institute (Koninklijk Nederlands Meteorologisch Instituut) website [94].

Output energy for the same system is compared in two scenarios as follows:

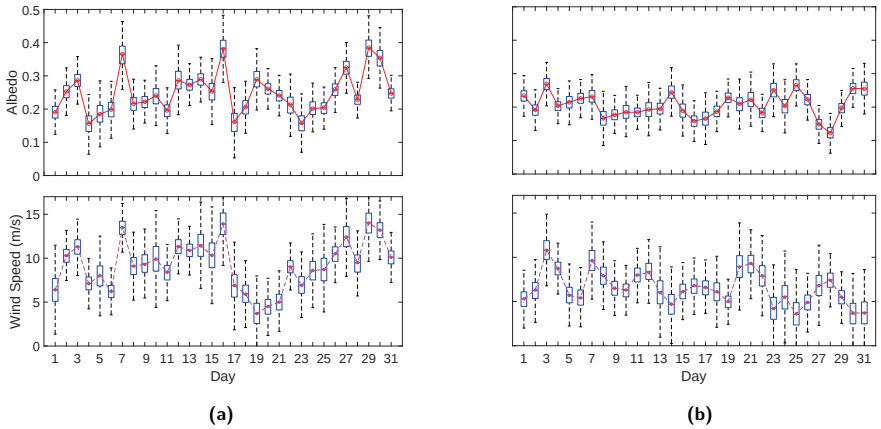

Figure 3.2 · Albedo and wind speed (m/s) during 2016 (a) January (b) August

(i) with constant $\alpha_{OSA} = 0.06$ as is calculated as the albedo for the open ocean surface reported by the American National Snow and Ice Data [85], and (ii) according to the more precise method as discussed in the methodology section to calculate albedo dynamically using wind speed and ζ. At first, we will discuss the relation between wind speed and albedo and after that we will review the difference between energy yield for the year 2016 considering constant and modeled albedo.

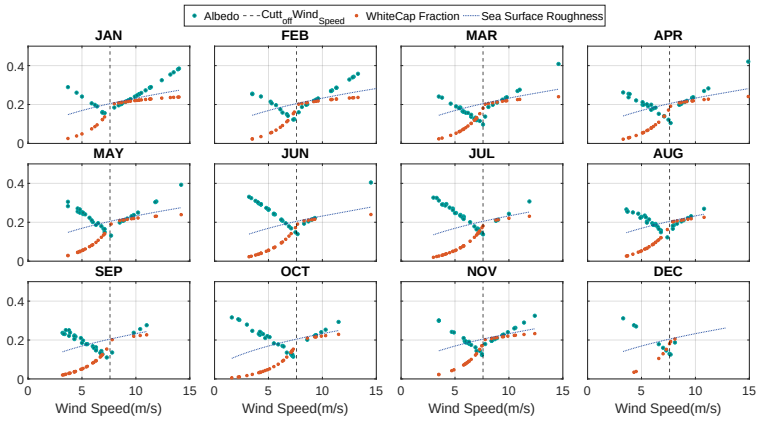

Figure 3.3 · Scatter plots of albedo and whitecap fraction as a function of Wind speed for the year 2016. For the threshold wind speed value (dashed line), see text.

Figure 3.2(a,b) shows box plots of the daily variation of albedo and the wind speed during January and August 2016, respectively. These two months are chosen randomly to depict the time trend of both wind speed and albedo during one

month with much higher solar zenith angle values compared to the other. The average value for albedo in January is $\overline{\alpha}_{OSA,Jan} = 0.25$ which is 0.044 higher than the value in August $\overline{\alpha}_{OSA,Aug} = 0.206$. Two main results may be concluded regarding this figure, (i) when the solar zenith angle is higher the average value for albedo is also higher, (ii) the trend of the wind speed is not completely followed by the albedo value trend in these two months.

For a deeper view let us discuss the whole year. Figure 3.3 shows the scatter plots for daily averages of albedo and wind speed for all 12 months of the year 2016, and also behaviour of sea surface roughness. This figure shows that albedo is larger in winter months compared to summer months and also the wind speed does not necessarily only increases the albedo value. Increasing the wind speed leads to larger sea surface roughness and decreasing albedo, however, by exceeding a certain threshold value for the wind speed the albedo starts increasing again. This increment is due to the formation of white caps on the sea surface which are more clearly visible during months with larger solar zenith angle. As shown in figure 3.3 there is a threshold point from which the effect of whitecap starts dominating the sea surface roughness. This threshold value can be easily found by considering the followings:

$$1 - f_{WC} = 1 - (3.97 \times 10^{-2} \times v^{1.59}) = 0 \tag{3.13}$$

Equation 3.13 gives $v = 7.61$ m/s, which is shown in figure 3.3 using a dashed dotted line.

Using the albedo data presented here in the performance model simulation [54], we arrive at the results shown in figure 3.4. Figure 3.4 shows the output difference in % for the energy yield of a floating PV system for the two different albedo scenarios for data of the year 2016 at Hoek van Holland (southwest of the Netherlands). It can be concluded that taking into account a varying albedo, the calculated PV system performance is larger in all months throughout the year, with about 3.04% on average, without a clear seasonal effect, compared to using a fixed value for α_{OSA}.

Increased performance is due to increased GTI. Figure 3.5 shows the ΔGTI shown in equation 3.14 comparing varying and constant albedo, calculated using Equation 3.14, and 2016 KNMI data.

$$\Delta_{GTI} = GTI_{constant\ albedo} - GTI_{modeled\ albedo} \tag{3.14}$$

Summing the months, annual GTI would be 46.5 kWh/m^2 higher if we consider the albedo with the studied mathematical model in this chapter. This difference will lead to the 41 kWh/kW$_P$ which is equal to 3.04% difference in performance

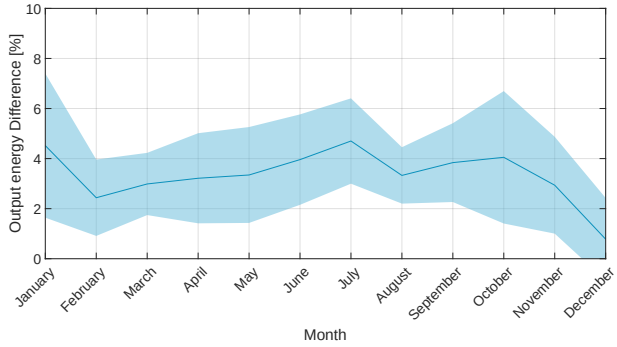

Figure 3.4 · The output energy relative difference in % between the system implementing a modeled albedo and a constant albedo for the location of the system.

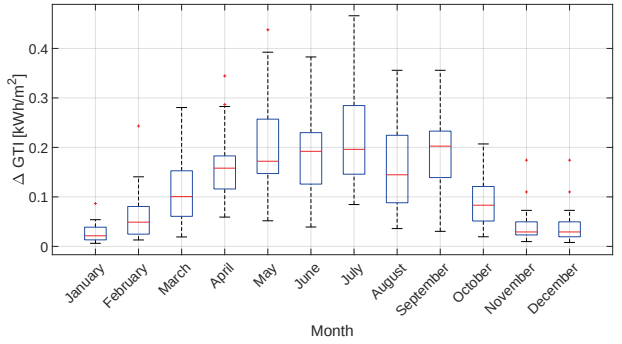

Figure 3.5 · The increase in surface irradiation considering modeled albedo and constant albedo.

in our modeled offshore FPV system. The annual energy yield computed by our FPV model discussed in [54] is 1346 kWh/kW$_P$. The rather small increase in performance due to including dynamically varying albedo can be understood realizing that the floating PV system is mounted horizontally in the water. The panel tilt is limited to 20° and we have shown in [54] that tilt angles are rarely above 10° only in case of high wind speeds. Additional reflected irradiation on horizontally located PV panels thus is limited. It can be expected that floating PV systems that are installed having a permanent non-zero tilt, will benefit more from including dynamically varying albedo, while it should be noted that increased performance of bifacial floating PV systems has been reported to be limited [46].

3.4 Conclusion

In this chapter, first a mathematical model for sea surface albedo is presented. It should be noted that the contribution of the ocean interior reflecting to surface albedo is neglected in this model. The modeled albedo is implemented in a fully mathematical model of an offshore floating PV system considering variable tilt due to the wave spectrum and wind speed. The results showed that albedo does not have a simple linear relation with wind speed. The effect of solar zenith angle is quite clear in this results. If the wind is strong enough to form whitecaps the albedo starts increasing and sea surface roughness is not dominant anymore. Comparing the floating PV system implementing constant and modeled albedo shows that compared to a fixed value for α_{OSA}, the PV system performance is larger by about 3.04% on average, without clear seasonal differences. This shows that dynamic albedo should be used in performance evaluations of floating PV systems.

Acknowledgements

This work is partly financially supported by the Netherlands Enterprise Agency (RVO) within the framework of the Dutch Topsector Energy (project Comparative assessment of PV at Sea versus PV on Land, CSEALAND).

4

Pooling the cable: a techno-economic feasibility study of integrating offshore floating photovoltaic solar technology within an offshore wind park

This chapter is based on the paper:
S.Z.M. Golroodbari, D.F. Vaartjes, J.B.L. Meit, A.P. van Hoeken, M. Eberveld, H. Jonker, W.G.J.H.M. van Sark, *Pooling the cable: a techno-economic feasibility study of integrating offshore floating photovoltaic solar technology within an offshore wind park*, Solar Energy 219 (2021) 65-74.

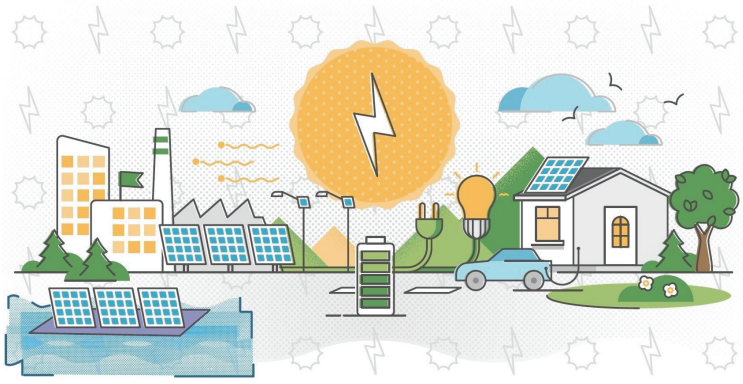

Abstract

In this paper, a techno-economic analysis is performed to assess the feasibility of adding an offshore floating solar farm to an existing Dutch offshore wind farm in the North Sea, under the constraint of a certain fixed cable capacity. The specific capacity of the cable that connects the offshore park to the onshore grid is not fully used due to the limited capacity factor of the wind farm. The principle of cable pooling allows to add floating solar capacity. Using weather data it is found that adding solar capacity leads to forced curtailment due to the cable capacity, but this is quite limited as as result of the anti-correlation of the solar and wind resource. For the economic analysis, different scenarios regarding subsidy measures are considered for the calculation of net present value and levelized cost of electricity. Also the optimum additional PV capacity for each scenario is computed. The results show that with higher cost per Wp, optimum PV capacity decreases, but more favourable subsidies lead to higher optimized PV capacities. As the aim of the paper is not limited to a case study a methodology is developed for generalization of the techno-economic analysis of a hybrid solar/wind park. In this generalization, the initial investment, system degradation, cable capacity, number of hours when each system is active, and energy price, are implemented to compute the optimum PV capacity regarding the net present value as an indicator for economic analysis of the project.

4.1 Introduction

Reaching greenhouse gas emission reduction goals requires massive deployment of renewable energy harvesting technologies such as solar and wind. Energy systems based on renewables are not only feasible, but already economically viable and decreasing in cost every year [111, 112]. Besides their intermittent character that poses a challenge for grid integration, another main issue of their increased share is their effect on land scarcity, especially in or close to densely populated areas such as the Netherlands [113, 114, 115]. Renewables generally require more land than fossil-fuel based electricity power plants, when excluding land use for mining. Hence, larger areas are needed to maintain similar or increased amounts of global electricity demand. Deployment of large wind parks and solar fields has been increasing, but also has met with increased public resistance. This has not only led to the development of offshore wind parks and increased interest in offshore floating solar systems, but also more attention is paid to measures to integrate solar fields in the existing landscape. Here multiple land use is key, while also biodiversity issues and agricultural aspects are being taken into account in their development [115, 116, 117]. Also, it has prompted the Dutch government to explicitly state that

deployment of photovoltaic (PV) solar systems should predominantly be done at roofs [118], while the huge potential of offshore PV has been recognized in a roadmap for PV systems and applications [119].

In the Netherlands, currently, four offshore wind farms are in operation with a total combined capacity of 957 MW. An additional 3,450 MW is planned to be developed by 2023 [120]. An even faster growth is seen for solar PV. At the end of 2019, nearly 7 GWp was installed [121], which made for a 5.4% contribution to the national electricity supply. For the realization of the national emission reduction goals for the Netherlands of 49% by 2030 and 95% by 2050 the installed renewables base should be increased substantially. A combination of 20 GW offshore wind, 11 GW on-shore wind, and 29 GW PVp would generate the projected electricity demand of 120 TWh in 2030. For 2050 this should be about doubled. Such large capacities require large areas of roof and façade surfaces and land for PV [119]. Due to land availability issues, floating PV has been suggested recently, and several floating PV systems are in operation globally [39]. These originally have been based on similar designs as used for land-based systems, as the water bodies on which these are deployed are relatively quiet in terms of wind and waves [68, 42]. The next more or less logical step is to take PV offshore. As wave and other weather conditions are much more severe at sea, different approaches are needed for large-scale floating PV systems. Much research in this field is being performed at the moment. One aspect is already found to be beneficial for performance, which is the cooling effect of (sea)water leading to higher energy yields [59, 54]. Beside the technical aspects, the capital- and operational expenditures will also play a role in future development. The floating panels are expected to be more costly than conventional PV panels, due to more corrosion resistant panel designs and extra floating and/or mooring components. Also, installation costs of the panels are expected to be higher. The construction of an offshore grid connection to transport the produced energy to the mainland is another important factor that is expected to increase the total costs per kWh.

Nevertheless, the Netherlands as many other countries surrounded with large bodies of water are considering offshore floating PV as a serious option for renewable energy supply. As an example, the recent Dutch national roadmap on PV potential states an overall potential of 200+ GWp of which most is in the built environment and on land, while it also defines an inland floating PV potential of 24 GWp, and an offshore potential of 45 GWp [119].

Given the large space available in between turbines of a large scale offshore wind park, as well as the already present or planned cable capacity to connect a wind park to the grid on shore, adding floating PV within such an offshore wind park may be a feasible option. The cable has been designed to transport

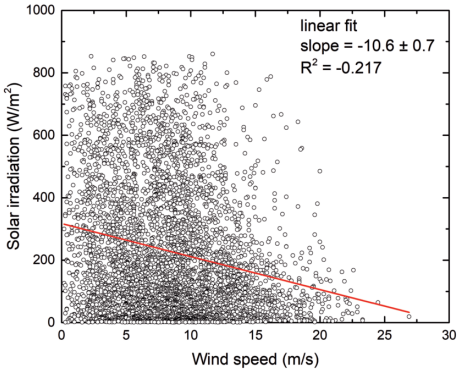

Figure 4.1 · Solar irradiance and wind speed correlation. Hourly data for 2005.

the maximum possible amount of power generated by the wind park, i.e., the rated wind park capacity, while capacity factors may be between 35% and 50% [122]. As shown in Fig. 4.1, a scatter plot of solar irradiance versus wind speed reveals that they are correlated negatively, albeit weak. Thus, adding solar can be expected to increase the cable capacity factor thus more effectively using the cable (also known as cable pooling), while providing less variable power, in a similar way as coupling wind farms and wave energy generators [123, 124]. In addition, costs for maintenance, operations and construction could be shared by integrating solar energy within offshore wind farms, leading to overall decreased capital and operational expenditures.

We do note that the actual area that an offshore PV park would need to generate 1 GWh is about 2-11 times smaller than required for an offshore wind park. Due to inter-turbine distances of at least 5 times the rotor diameter to limit wake effects, the power density of a wind park ranges from 5-10 MW/km^2, while it is about 100-200 MWp/km^2 for a solar PV park. Nevertheless, capacity factor differences lead to a energy density of about 15-44 GWh/km^2 for a wind park versus about 90-180 GWh/km^2 for a solar park in the Netherlands, with 35-50% capacity factor for wind [122] and 10% capacity factor for PV [125]. Hence, this difference in area usage would leave sufficient room for any maintenance ships required to sail through the wind park, and at the same time would lead to minimal ecological disturbances due to shading of the sea subsurface [126].

In this paper we will perform a techno-economic feasibility study of incorporating an offshore floating PV system in a planned wind park of 752 MW rated capacity in the North Sea, with a planned transport cable capacity of 700 MW. We note here that as the power production by the wind farm is mostly lower than the rated capacity, the cable capacity is not used fully. Even at rated capacity,

wake losses lead to sub-optimal usage of cable capacity. A decrease of efficiency and increase of downtime of the wind farm over its lifetime will result in a further sub-optimal usage of cable capacity, hence a solar park can make use of leftover cable capacity. In section 4.2, we will describe the hybrid wind solar park and present the methodology used to determine energy generation by PV and wind turbines, and how to find an optimum configuration in terms of economics. In section 4.3 results are presented and discussed. It also provides suggestions on how to generalize the results obtained, given site-specific meteorological conditions, and technical and economical aspects. Section 4.4 provides a conclusion and outlook for further research.

4.2 Method

In this section details of the case study wind farm Borssele are described, followed by a description of combining it with a possible floating PV system. Also, different scenarios for an economical analysis will be reviewed.

Wind park site description

We focus our analysis on a planned wind park, denoted as Borssele wind park I & II, based on the report published by the Dutch Enterprise Agency RVO [120]. This report contains a detailed description of the Borssele Wind Farm Zone (BWFZ), a collection of data regarding the physical environment of the Borssele sea area, detailed information on national subsidy grant related issues and a legal framework for application of this grant. The BWFZ is located at the southern border of the Netherlands Exclusive Economic Zone (EEZ) at 51.583° N, 3°E, approximately 500 m from the Belgium border, see Fig. 4.2. The first Siemens Gamesa 8 MW turbines with rotor diameter of 167 m have been installed recently by wind park developer Ørsted, and the park should be fully operational by the end of 2020 [127].

The BWFZ has an area of approximately 234 km^2, but it covers 344 km^2 with maintenance and safety zones included. The BWFZ is surrounded by a sand extraction area, piloting zone, shipping lanes and anchoring locations as well as Belgium wind farms, just south-west of the zone. Total planned rated capacity of those parks is about 600 MW of which about 230 MW is operational already.

Although existing infrastructure such as pipelines and telecommunication cables cross the BWFZ, cost of relocating these was too high, and as a consequence planning of the wind turbine construction is taking the existing infrastructure into account. On both sides of the Dutch-Belgian border a safety zone of 500 m

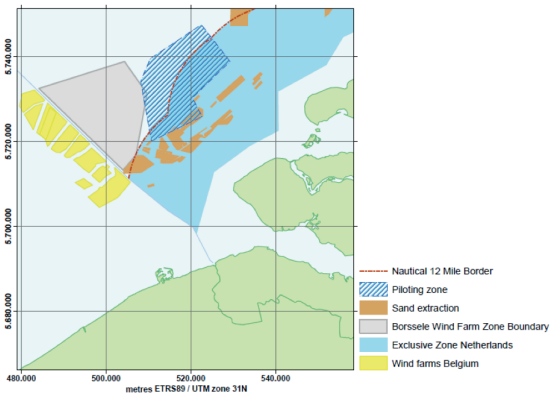

Figure 4.2 · The Borssele Wind Farm Zone and surrounding areas. Source: RVO [120].

is defined. The same safety zone of 500 m is applied to both sides of the cables and pipelines that run through the BWFZ. Between Borssele I & II, a shipping corridor is in place, going from east to west. The national transmission system operator (TSO) TenneT has planned to install two offshore substations: Borssele Alpha and Borssele Beta [128]. The substation Alpha will connect Borssele I & II to the onshore electricity grid via a 700 MW capacity cable.

System Modeling

In order to study the feasibility of the hybrid power system, which is described before, we need to use a precise mathematical model. With that model we will be able to perform a technical and economic analysis.

The goal of the technical analysis is to estimate the total energy production of the combined wind solar farm. The analysis is divided into three main steps:

1. based on historical wind data, the potential energy production of the Borssele I & II wind farm will be calculated;

2. based on historical solar irradiance data, the potential energy production of a floating PV system will be calculated for different PV system sizes;

3. these two data sets are then combined to estimate the total energy production of the complete system.

We use an hourly time resolution throughout this paper. The cable capacity of 700 MW limits the energy transmission from the offshore system to the mainland, so optimizing annual energy production should be performed using the 700 MW cable constraint.

In the following subsections we will first describe the wind park and the solar park model individually, which is based on a wind turbine model as well as a solar module model. The next step is the methodology for calculating the annual energy as well as energy per hour. After that, an economic analysis will be described, using different scenarios for subsidy schemes.

Offshore wind model

The modeling of the offshore wind park has two main steps: (i) calculating the optimal potential power output of wind turbines, and (ii) implementing the limitations of the wind park in which the turbines are part of. The offshore wind farm will consist of 94 Siemens Gamesa wind turbines of 8 MW capacity each. Figure 4.3 shows the power curve of such a turbine. The extracted specifications of the wind turbine from the power curve are cut-in speed of 3.5 m/s, cut-out speed of 25 m/s, and rated power wind speed of 13 m/s. To calculate the generated amount of power at a certain moment it is required to multiply the hourly wind speed data by the power curve.

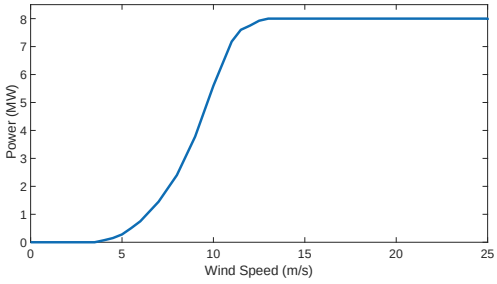

Figure 4.3 · Power curve of the Gamesa 8 MW wind turbine. [129]

Wind Farm Performance

The conversion of wind energy to useful electrical energy involves two processes: (i) the primary process of extracting kinetic energy from wind and conversion to mechanical energy at the rotor axis, and (ii) the process of the conversion into useful energy, mostly electrical [130]. One of the important issues in the first process is the wind turbine wake effect decreasing the total conversion efficiency of a wind park. Bulder et al. [131] have studied the wake effect and wind farm power density and they concluded that in general the higher the power density of a wind park, the lower the efficiency due to the larger wake effects. Wind farm efficiency of the Borssele location has been estimated in [131] considering a turbine capacity

of either 6 MW or 8 MW, and by wind farm power density, 6 and 9 MW/km^2. The wind farm design that is the most applicable for this research is expected to achieve an efficiency of 91.4% on annual basis, hence a 8.6% loss compared to combining single wind turbines. Wake effects are accounted for by adjusting wind velocities based on the model by Jensen [132, 133]. This leads to a park efficiency of 90%.

The hourly ($E_{WF,h}$) and annual ($E_{WF,a}$) wind farm energy production is shown in Eqs. (4.1) and (4.2).

$$E_{WF}(h) = N_{WT}\ E_{WT}(h) \tag{4.1}$$

$$E_{WF,a} = \sum_{h} E_{WF}(h) \tag{4.2}$$

in which N_{WT} is the number of wind turbines in the farm, which is 94 in this case, $E_{WT}(h)$ is the hourly (h) generated energy per wind turbine with respect to wind speed. All machinery experiences an unrecoverable loss in performance over time. The energy produced by a wind farm gradually decreases over its lifetime, due to falling availability, aerodynamic performance or conversion efficiency [134]. If capacity factors decrease significantly with age, wind farms will produce a lower cumulative lifetime output, increasing the levelized cost of electricity (LCOE) of the wind farm. Based on the research presented in [134] it is assumed that the level of degradation of the Borselle I & II wind farm's output is 12% over a twenty year lifetime (0.6% per year). Therefore, the Borssele wind farm energy production over time is calculated as shown in equation 4.3.

$$E_{WF,N_{year}} = \sum_{n=1}^{N_{year}} E_{WF,1} \times (1 - 0.006)^{n-1} \tag{4.3}$$

where $E_{WF,N_{year}}$ is the cumulative amount of energy generated by the wind farm, $E_{WF,1}$ the energy generated by the wind farm in the first year, n is the summation index and N_{year} is the total number of years the whole system is considered to be operational.

Solar Farm Performance

The modeling of the power output of the floating solar PV system is built on the same reasoning as with the offshore wind farm. First the optimal performance of the floating solar PV system was calculated, after which limitations were applied. Equations (4.4) and (4.5) are used to compute the annual generated energy from

one solar panel in the solar farm.

$$E_{PV}(h) = PR\ \eta_{PV} A_{PV} G(h) \tag{4.4}$$

$$E_{PV,a} = \sum_{h} E_{PV}(h) \tag{4.5}$$

where $E_{PV}(h)$ is hourly generated energy of one PV module (kWh), $E_{PV,a}$ is annual generated energy (kWh), $G(h)$ is solar irradiation per hour (Wh/m^2), A_{PV} is panel area (m^2), η_{PV} is panel efficiency, and PR is the performance ratio to account for system loss [20].

In this research, it is assumed that the solar panel is a 1.6 m^2 crystalline silicon panel which has rated maximum power point P_{MPP} of 300 Wp (hence η_{PV} = 18.8%). The efficiency is a function of temperature (T), the temperature coefficient of power used here is -0.375%/K, which is extracted from the specification sheet of an Exasun X60-BG300 module [135]. Temperature and other system losses including DC-AC conversion by inverters used are all accounted for in the performance ratio PR [20]. As an example, for the irradiation and temperature data for the year 2006 at the wind park location, Figure 4.4 shows DC performance ratio (PR), illustrating the effect of temperature, i.e., performance ratio is lower in summer than in winter[136]. In addition, the strong dips observed in summer are due to high ambient temperatures that occurred for short periods of time.

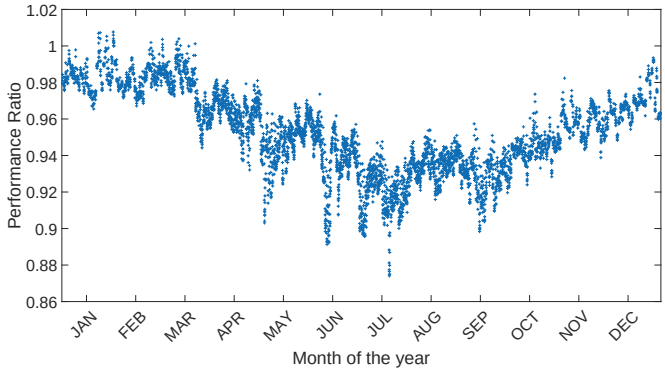

Figure 4.4 · PV module DC PR for the year 2006, illustrating the effect of temperature.

Equations (4.4) and (4.5) calculate the annual energy output of a single panel. In order to calculate the total energy output of the solar farm of a certain capacity, this result should be multiplied with the total number of solar panels N_{PV} corresponding with the installed solar capacity. For example, a 1 MWp system contains 3,333 panels, which would require an area of 0.0053 km^2, following a horizontal

design. Hourly and annual PV farm outputs thus are:

$$E_{PVF}(h) = N_{PV} E_{PV}(h) \tag{4.6}$$

$$E_{PVF,a} = N_{PV} E_{PV,a} \tag{4.7}$$

Except for the rotating blades of the wind turbines, shading effects on solar panels that would reduce solar park efficiency can be ignored. However, there is a decay of the efficiency of a solar panel over its lifetime. An accurate quantification of power decline over time, also known as degradation rate, is essential to all stakeholders, utility companies and researchers alike. A statistical approach based on historical data has been reported to quantify degradation rates [137]: the efficiency of solar panels reduces with 0.5 percent per year on average. The total energy production of the solar farm over its lifetime thus can be calculated in Eq. (4.8):

$$E_{PV,N_{year}} = \sum_{n=1}^{N_{year}} E_{PV,1} \times (1 - 0.005)^{n-1} \tag{4.8}$$

where $E_{PV,N_{year}}$ is the cumulative energy output of the solar panel over its lifetime, and $E_{PV,1}$ is the energy output of the solar panel in the first year. As above, the total energy output of the solar farm is calculated by multiplying with the number of panels, as in Eq. (4.7).

Capacity factor

The capacity factor is calculated using the following equation. It is equivalent to the amount of full load hours in a year.

$$CF = \frac{actual\ output\ (MWh)}{nominal\ power\ (MW) \times 365\ \times 24} \times\ 100\ (\%) \tag{4.9}$$

Optimizing the combined wind solar system

The main constraint in this research is that the power transmission cable has a maximum capacity of 700 MW which limits the total amount of power that can be produced by the floating solar panels and the wind park without congesting the power transmission cable. In this research, it is assumed that if the combined solar and wind power production is over 700 MW, the solar output will be curtailed to a value which can vary between 0-100%, meaning that they will not deliver full power to the grid at that time. Note that we have conveniently chosen an hourly time resolution. The power constraint of 700 MW thus translates to an energy

constraint of 700 MWh. The total energy production of the combined energy system is therefore calculated as follows, with C_{PV} the curtailment ratio (0-100%):

$$E_{tot}(h) = E_{WF}(h) + C_{PV}E_{PVF}(h) \leq 700 \text{ for } h \in [1, 8760] \tag{4.10}$$

The optimization problem here is defined as

$$\min\{\texttt{cost of electricity}\}, \textbf{ subject to } \{\texttt{cable constraints}\} \tag{4.11}$$

Economic analysis

The outcomes of the technical analysis give insight on the amount of energy that can be generated by integrating solar panels in offshore wind farms. The goal of the economic analysis is to evaluate the economic value of the produced energy and to provide insight on how much such an energy system may cost. Therefore, the first step of the economic analysis was to determine the value of the produced energy.

Determination of the value of energy

In order to calculate the value of generated electricity by the complete system, we consider the (i) market price, (ii) cost of grid connection, and (iii) value of renewable energy. The aforementioned issues will be studied in the following.

Market price

Since the energy market system is complex and many factors influence the energy price, which in addition can fluctuate considerably, we took average annual energy prices based on the Amsterdam Power Exchange (APX) market, now part of European Power Exchange (EPEX). The APX market distinguishes energy prices in a peak (8am - 8pm) and off-peak price (8pm - 8am). Table 4.1 shows the yearly APX price between 2010 and 2018. Average values are 52.9±7.8 €/MWh and 39.9±6.4 €/MWh for peak and off-peak prices, respectively. As there is a large uncertainty in predicting future energy prices, for simplicity the rounded average values of 50 €/MWh and 40 €/MWh for peak and off-peak prices are assumed, respectively. From now on in this paper, the market price is denoted as $\pi_{APX,i}$ with subscript i being p or op for peak and off-peak price, respectively.

Cost of grid connection

The cost of the grid connection of offshore wind farms is considered as social cost, meaning that the government is willing to pay this cost to facilitate the

Table 4.1 · Yearly average APX Price

Year	$\pi_{APX,p}$ (€/MWh)	$\pi_{APX,op}$ (€/MWh)
2010	56.01	39.41
2011	61.59	46.81
2012	58.18	42.45
2013	61.16	46.87
2014	48.36	37.22
2015	47.16	36.16
2016	39.30	28.32
2017	46.27	35.50
2018	57.97	46.77
Average	52.89	39.94

generation of offshore energy. This is also the case with the Borssele wind farm grid connection. The total grid connection cost of the Borssele location is $\pi_{og} = 0.015$ €/kWh [138].

Value of renewable energy

Despite the availability of several subsidy schemes to stimulate the development of renewable energy technologies in the Netherlands, there are no subsidies specifically designed for offshore floating solar systems yet. Since it is unclear what subsidies will be granted for this type of technology in the future, there are three scenarios developed with each a different level of subsidy.

Scenario one: No subsidies for offshore floating solar technologies

In this scenario the total energy value $\pi_{no,i}$ is calculated as follows:

$$\pi_{no,i} = \pi_{APX,i} + \pi_{og},\ i \in [p, op] \tag{4.12}$$

Scenario two: Stimulation of Sustainable Energy Production (SDE+)

Energy producers can receive financial compensation for the renewable energy they generate. It is not always profitable to produce renewable energy as the generation cost is higher than the market price. This price difference is the unprofitable part. The subsidy scheme SDE+ compensates the unprofitable component for some years, i.e. 15 years. The compensation depends on the renewable energy technology used. The SDE+ subsidy is an operating grant. The price for the production of renewable energy is capped (base sum). For the Borssele Wind Farm Location the base sum is set at $\pi_{SDE+} =$ €125/MWh [139]. Thus, the total

energy value $\pi_{BS,i}$ is calculated as follows:

$$\pi_{BS,i} = \pi_{SDE+} - \pi_{APX,i},\ i \in [p, op] \tag{4.13}$$

and the total price scenario 2 is

$$\pi_{SDE,i} = \pi_{APX,i} + \pi_{BS,i} + \pi_{og},\ i \in [p, op] \tag{4.14}$$

Scenario three: Maximum Subsidy (doubled SDE+)

It is assumed that because the floating solar technology is still in its development phase, the government is willing to grant the double amount of money per MWh compared with the amount that was reserved for the Borssele II location (scenario 2). For that reason scenario 3 assumes a cap of the subsidy of $\pi_{SDE+,max} = 250$ €/MWh (doubled SDE+) and the total energy value is calculated as follows:

$$\pi_{max,i} = \pi_{SDE+,max} - \pi_{APX,i},\ i \in [p, op] \tag{4.15}$$

and the total price scenario 3 (doubled SDE+) is

$$\pi_{2SDE,i} = \pi_{APX,i} + \pi_{max,i} + \pi_{og},\ i \in [p, op] \tag{4.16}$$

Prices for all mentioned scenarios per peak and off-peak are summarized in Table 4.2.

Table 4.2 · Different scenarios subsidy and price comparison

Scenario	Subsidy (€/MWh)		Price (€/MWh)	
	Peak	Off-Peak	Peak	Off-Peak
1: no subsidy	0	0	65	55
2: SDE+	75	85	140	140
3: doubled SDE+	200	210	265	265

Lifetime benefits

With the total value for the generated energy determined in the previous steps, the last step is the calculation of the total revenue of the combined wind and floating solar PV system over its lifetime. First the total revenue Π_a for each year was calculated by the following equation:

$$\Pi_a = \sum_h (E_p(h)\pi_p + E_{op}(h)\pi_{op}) \tag{4.17}$$

where $E_i(h)$ is hourly energy production (MWh), π_i is price of energy in €/MWh, and $i \in [p, op]$.

Assuming a interest rate of 3%, the net present value NPV of the benefits over the energy system's lifetime are then calculated with the following equation:

$$NPV = F_0 + \sum_{n=1}^{N_{year}} \frac{F_n}{(1+r)^n} \tag{4.18}$$

where F_n is cash-flow after n years, r is interest rate, n is summation index, and N_{year} it the total number of years. The inclusion of the F_0 term is important in the above formula. A typical investment project involves a large negative F_0 which is the initial investment, with positive future cash flows, a combination of revenues and the expenses which are expecting to return the initial investment. For this study we consider F_n as:

$$F_n = \Pi_{a,n} - Opex_n \tag{4.19}$$

where $Opex$ is expenditures for operation and maintenance and is assumed to be 2% of the initial investment which is higher that what is mentioned in [140] which is 1.35%. Therefore, equation 4.20 is derived as follows:

$$NPV = \sum_{n=1}^{N_{year}} \frac{\Pi_{a,n}}{(1+r)^n} - F_0 \times (1 + 0.02 \times N_{year}) \tag{4.20}$$

Thus, NPV is an indicator of how much value an investment or project adds to the firm.

Another metric of interest is Levelized Cost of Electricity or (LCOE), which can be defined as the NPV divided by the amount of generated energy E_{tot} during a system's lifetime, which is N_{year}:

$$LCOE = \frac{NPV}{E_{tot}} \tag{4.21}$$

where E_{tot} is the sum of total wind and solar energy, as given in Eqs. (4.3) and (4.8).

4.3 Results and Discussion

The results of the techno-economical analysis are divided into two main parts: (i) the technical analysis results and (ii) the economic analysis results. The technical analysis section provides information on the production potential of floating solar energy within the offshore wind farms. The economic analysis shows what the potential financial benefits are of integrating offshore solar and wind on the North Sea.

Meteorological data

The wind data used in this research was extracted from the KNMI North Sea Wind (KNSW) atlas [141], for the years 2005-2017. It provides validated data on a horizontal grid of 2.5 km spatial resolution. Within the Borssele wind farm area a total of 18 data points were used to calculate the average hourly wind speed of the whole area for each year separately, at the hub height of the turbine.

The solar data was extracted from the Copernicus Atmosphere Monitoring Service (CAMS) Radiation Service database [142]. This database provides hourly solar radiation data for the period of 2005-2017, expressed in Wh/m^2. Data was extracted for the latitude and longitude of the solar farm.

Technical Results

The main goal of the technical analysis is to provide reliable energy production data that can be used for the economic analysis. The first step was therefore to determine a base year that can be used to estimate the energy production potential over the system's lifetime.

Base year

For assigning the base year the average total production per year is compared considering data between years 2005 and 2017. Figure 4.5 shows that year 2006 is the best option as the solar and wind data both are the closest to the average values. We did not use a typical meteorological year as the correlation between wind and solar would be lost. We note that interannual variations in wind speed are large than solar irradiance variations.

Energy generation

Figure 4.6 shows scatter plots of the hourly energy generation of the combined wind and solar park of capacity 752 MW and 300 MWp, respectively, for the year 2006, using the methods outlined in Section 4.2. It can be seen that by adding solar capacity, more energy can be transported via the cable which thus is more effectively used. However, for some hours in the year the cable capacity of 700 MW is exceeded. Increasing the solar capacity from 300 MW upwards will lead to violations of maximum cable capacity to occur more often. For this particular year, we calculate a capacity factor of 46.49% and 14.05%, respectively. Table 4.3 shows the effect on adding multiples of 100 MWp solar capacity to the 752 MW wind park. For example, although the number of hours per year that cable capacity is

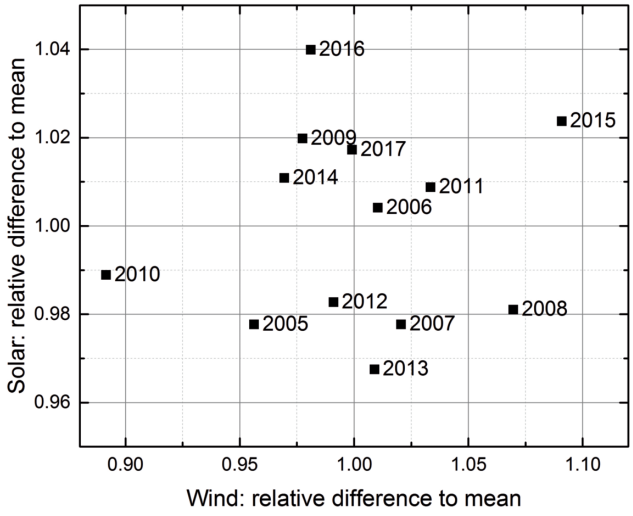

Figure 4.5 · Scatterplot of solar and wind resource compared to the mean of each resource. Annual solar irradiance (kWh/m^2/yr) and average annual wind speed (m/s) have been used.

exceeded is increasing to 12.07% for 300 MWp of added solar capacity, curtailed energy is only 1.72%.

Table 4.3 · Effect of adding multiples of 100 MWp PV capacity to the 752 MW wind park. The number of hours that cable limit is exceeded increases, as well as curtailed energy.

PV capacity (MWp)	number of hours >700 MWh	generated energy (GWh)	curtailed PV energy (GWh)	relative PV curtailment (%)
0	533	3063	0.00	0.00
100	1036	3186	18.03	0.56
200	1074	3309	37.86	1.14
300	1109	3433	58.94	1.72
400	1165	3556	81.99	2.31
500	1222	3679	107.28	2.92
600	1303	3803	136.57	3.59
700	1432	3927	172.51	4.39
800	1615	4050	218.98	5.41
900	1800	4174	279.11	6.68
1000	1956	4297	349.32	8.13

For the base year 2006, we find that for $G(h) \neq 0$ there were 4480 hours with non-zero wind speed. We find that for 83% of that amount of hours, the wind farm does not operate optimally (at full capacity), so the full cable capacity is not used thus allowing to add solar power. Full capacity (at rated power) occurs for 12% of that amount of hours, while no power is generated for 10% or these hours, as

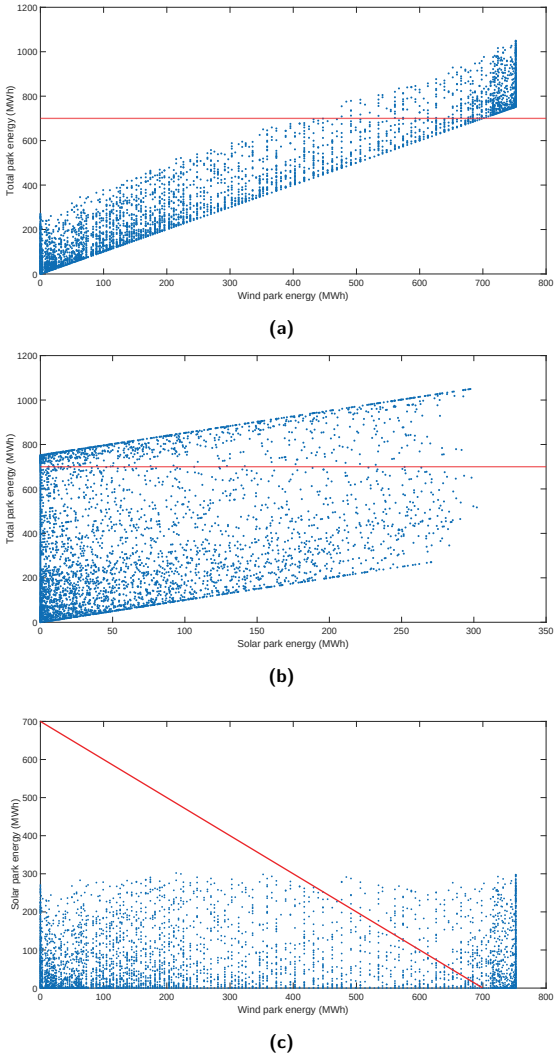

Figure 4.6 · Scatter plots for a combined solar and wind park of 300 MWp and 752 MW capacity, respectively, for the year 2006. For some hours the cable constraint of 700 MW (red line) is surpassed. (a) total park energy versus wind power, (b) total park energy versus solar power, (c) solar versus wind park energy.

the wind speed is lower than the cut-off wind speed (3.5 m/s). For the remaining 78% of hours power is lower than rated power. This is based on the power curve characteristics of the wind turbine (Fig. 4.3), i.e. full power production for wind speeds in the range of 13 to 25 m/s, and lower power or zero power production for wind speeds between 3.5 and 13 m/s, and 0 and 3.5 m/s, respectively. While the wind park efficiency is not 100% due to wake effects, hourly maximum produced

power can be larger than the cabling power limit of 700 MW. This occurs for 533 hours of the year leading to 41 GWh curtailed wind energy, or 1.3%.

Energy production over two decades

It is computed that the Borssele wind farm generates about 60,000 GWh over a period of 20 years. On average, the cable capacity factor is 49.94% without solar panels installed and increases linearly up to 88% with an installed solar capacity of 1.9 GWp. A cable capacity factor of 100% can be obtained for a solar capacity of 2.6 GWp. However, it should be noted that cable capacity is not our only constraint and we need to consider the economical analysis as well.

Economic analysis

The technical analysis shows that: (i) there is a large potential for floating PV panels within the Borssele I & II wind farm, (ii) there is a limitation on the extra energy that can be produced by adding more solar panels, and (iii) the marginal production potential decreases rapidly with increased installed solar capacity. However, it is necessary to estimate the economical benefits of this combination which we will discuss in this section. Figure 4.7 shows the net present value for different

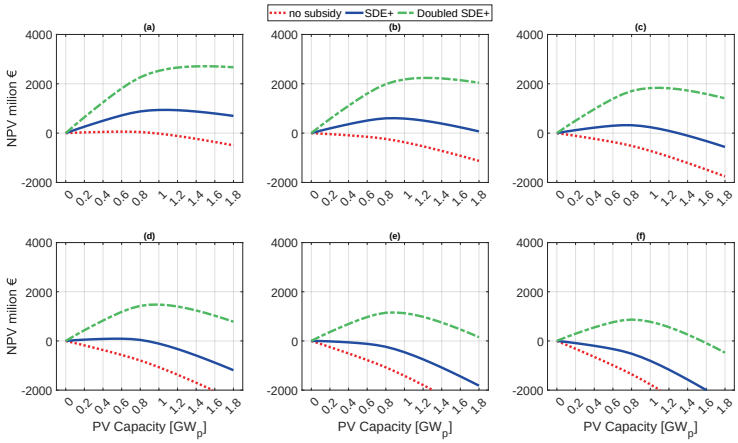

Figure 4.7 · NPV for different scenarios considering the initial investment: (a) 0.6, (b) 0.85, (c) 1.1, (d) 1.35 , (e) 1.6, (f) 1.85 [€/W_p]

scenarios. The initial investment for each Wp for a land based system is assumed 0.6€/Wp [140]. To have a better perspective for economic analysis we considered different variations for the initial investment for a floating system as

$$f_{0,FPV} = f_{0,LB} + \gamma, \ \gamma \in [0, 1.25] \tag{4.22}$$

where γ is an additional price value and $f_{0,FPV}$ and $f_{0,LB}$ are the initial investment for floating and land-based PV system per W_p, respectively. The upper limit is based on recent data reported in [143]. Figure 4.7 shows that the relation between NPV and PV capacity is not linear and related to the decrease of the marginal power production per extra installed MWp. This figure shows that a very slight change in initial investment for the first scenario (no subsidies) makes the $NPV < 0$. In the optimization problem for this study we should consider both NPV and the curtailment energy and solve the problem. Figure 4.8 shows the optimum PV capacity for different scenarios with different initial investments over the bar charts which is derived from Figure 4.7. Obviously, with higher cost per Wp, optimum PV capacity decreases, but more favourable subsidies lead to a higher optimized PV capacities. It is clearly shown that for solving this optimization problem many aspects should be considered which will be discussed more generally in the next subsection.

Generalisations

From the above we can generalize the optimization of combined wind and solar parks. Given site-specific meteorological conditions (wind, irradiation, temperature) one should calculate specific hourly energy generated $Y_W(h)$ and $Y_{PV}(h)$ in kWh/kWp, for both wind and solar capacity, P_{WF} and P_{PVF}, respectively. Optimization of the combined wind and solar park in combination with cable capacity P_{cable} can be done by calculating the additional energy from the solar power system as:

$$\begin{aligned} E_{opt,PV} = \sum_n \left(\sum_h P_{PVF} Y_{PV}(h) \times (1 - d_{r,PV})^n \right) - \\ \left[P_{cable} - \sum_n \left(\sum_h P_{WF} Y_W(h) \times (1 - d_{r,W})^n \right) \right] \end{aligned} \tag{4.23}$$

where $d_{r,i},\ i \in [PV, W]$ is degradation factor for system i, and referring to Eq. (4.17) specific hours of power generation are based on the peak and off-peak classification we used above:

$$Y_i = Y_{i,p} + Y_{i,op},\ i \in [PV, W] \tag{4.24}$$

The optimization problem is generalized in Eq. (4.25). NPV should be calculated as mentioned in Eq. (4.20),

$$\max\{NPV\},\ \texttt{for}\ \{P_{WF}, P_{PVF}\}\ \textbf{subject to}\ \{P_{cable}\ \&\ E_{opt,PV}\} \tag{4.25}$$

Two important constraints for this problem are the cable capacity and $E_{opt,PV} > 0$. In this study, the optimum additional floating solar energy system is discussed considering both technical and economical aspects. First, generated solar energy regarding the generated wind energy and cable capacity is calculated. To solve the optimization problem further information is required namely, initial investment per Wp for the floating PV system. Calculating NPV clarifies the economic analysis of the system. For an acceptable project we need to solve the problem $NPV = 0$, the system is profitable if $NPV > 0$. The aforementioned case study showed that the relation between NPV and PV capacity is not linear, which means that increasing the solar capacity does not necessarily lead to higher revenues or lower LCOE for the project. Figure 4.8 shows that this system without subsidy could be profitable only if:

$$f_{0,FPV} \leq f_{0,LB} \tag{4.26}$$

However, for the SDE+ scenario this system could be profitable even if:

$$f_{0,FPV} \leq 2.67 \times f_{0,LB} \tag{4.27}$$

and with doubled SDE+ the system is profitable for all considered values in this study.

Figure 4.8 indicates the optimum PV capacity for each scenario, derived from

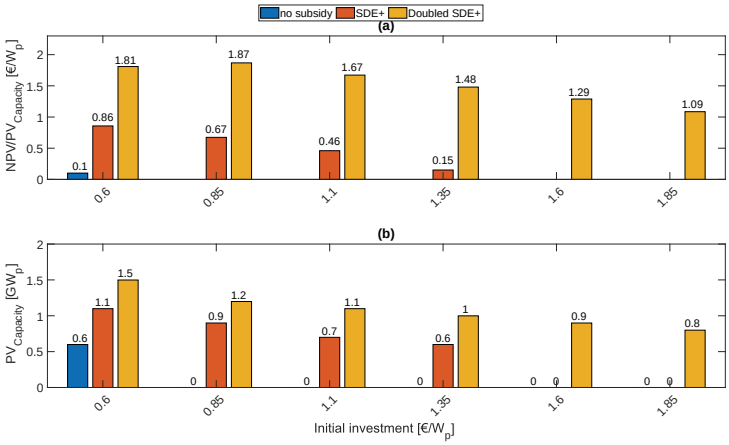

Figure 4.8 · (a) Ratio of NPV and PV capacity, (b) optimum PV capacity for the system based on initial investment [€/Wp].

Fig. 4.7. For this comparison the PV capacities between zero and 1.9 GWp are studied and a clear trend is observed. The ratio of NPV and PV capacity is decreasing with increasing initial investment. Also, the optimum PV capacity is

decreasing with increasing initial investment. It is clear that a subsidy is essential for this project in case the initial investment for the floating PV system is higher than 140% of the land-based PV system. The associated $LCOE$ values are shown in Fig. 4.9, and reflect the variation in NPV and PV capacity. Also, the higher the subsidy, the lower the $LCOE$. We note that these values compare well with recently published values [143], but also show that subsidies are necessary to obtain $LCOE < 0.05$ €/kWh, which are current generating costs of fossil-fuel based electricity generating plants in the Netherlands.

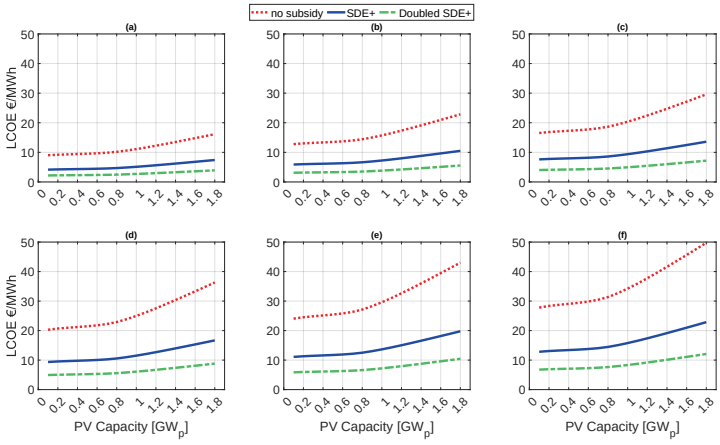

Figure 4.9 · Variation of $LCOE$ with PV capacity for different scenarios considering the initial investment: (a) 0.6, (b) 0.85, (c) 1.1, (d) 1.35 , (e) 1.6, (f) 1.85 [€/Wp]

4.4 Conclusion

The combination of an offshore solar PV system and a wind farm can be beneficial in technical and economical terms. At times with sub-optimal power generation by wind turbines the cable that transports electricity to the coast is not optimally used either. Adding solar capacity increases cable usage, which is known as cable pooling. We have calculated optimal wind and solar combined capacity given meteorological conditions in the North Sea, showing that curtailment of solar is quite limited.

The economical analysis showed that the profitability of integrating floating PV within offshore wind farms depends on two major factors: the marginal power delivered to the grid by floating PV and the costs of the solar system. Improving the marginal solar power delivered to the grid and decreasing the total costs for

the offshore FPV system would result in larger total benefits. We have also shown that subsidy is needed at present to support offshore FPV deployment.

Finally, our case study is further generalized realizing that meteorological conditions, in particular the anti-correlation of the wind and solar resource is determining, next to cost, the optimum wind-solar combination.

Acknowledgements

The authors gratefully acknowledge fruitful discussions with Brigitte Vlaswinkel (Oceans of Energy), Anne de Waal (UU), and Geert Harm Boerhave (RVO). This work is partly financially supported by the Netherlands Enterprise Agency (RVO) within the framework of the Dutch Topsector Energy (project Comparative assessment of PV at Sea versus PV on Land, CSEALAND).

5

Improvement of Shade Resilience in Photovoltaic Modules using Buck Converters in a Smart Module Architecture

This chapter is based on the paper:
S.Z. Mirbagheri Golroodbari, A. De Waal, W.G.J.H.M. van Sark, *Improvement of shade resilience in photovoltaic modules using buck converters in a smart module architecture*, Energies, 11 (2018) 250.

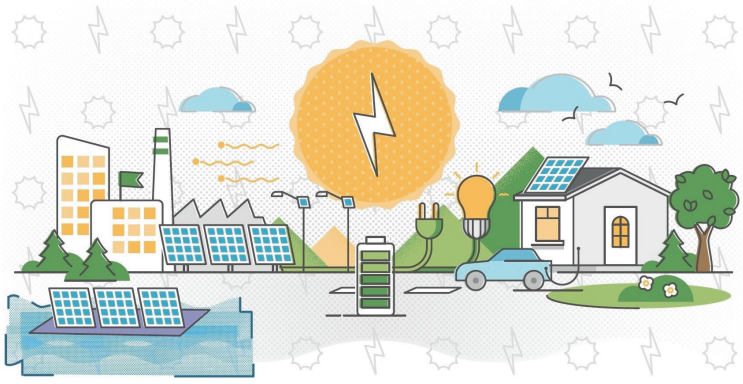

Abstract

Partial shading has a nonlinear effect on the performance of photovoltaic (PV) modules. Different methods of optimizing energy harvesting under partial shading conditions have been suggested to mitigate this issue. In this chapter, a smart PV module architecture is proposed for improvement of shade resilience in a PV module consisting of 60 silicon solar cells, which compensates the current drops caused by partial shading. The architecture consists of groups of series-connected solar cells in parallel to a DC-DC buck converter. The number of cell groups is optimized with respect to cell and converter specifications using a least-squares support vector machine method. A generic model is developed to simulate the behavior of the smart architecture under different shading patterns, using high time resolution irradiance data. In this research the shading patterns are a combination of random and pole shadows. To investigate the shade resilience, results for the smart architecture are compared with an ideal module, and also ordinary series and parallel connected architectures. Although the annual yield for the smart architecture is 79.5% of the yield of an ideal module, we show that the smart architecture outperforms a standard series connected module by 47%, and a parallel architecture by 13.4%.

5.1 Introduction

It is now commonly acknowledged that fossil fuel-based generation presents serious challenges to the environment, in terms of global warming, climate change, and society at large. It is also commonly acknowledged that renewable energy sources (RES) are viable, clean, and efficient alternatives. Amongst the RES, photovoltaic (PV) systems, which are maintenance and pollution free, [144, 145, 146], have been increasingly used as the main source of power generation in both standalone and grid-connected residential and large-scale systems [146]. Every year the solar industry is breaking new records and the global PV market grew significantly to at least 74,4 GW in 2016 [147]. Moreover, in 2016 solar installations contributed 39% of all new electric generating capacity, for the first time more than all other technologies [148].

Energy harvesting from a PV module under uniform irradiation is simply possible by connecting it to an inverter that implements a maximum power point tracking (MPPT) algorithm along with a DC-AC converter. The most frequently used MPPT methods are gradient descent based methods such as perturb and observe (PO) and incremental conductance (Inc_Cond); these conventional methods are also denoted as hill climbing algorithms [149]. MPPT algorithms are used to control the converter as an interface between the PV module and the grid and/or

load. However, irradiation is not always uniform, and partial shading (PS) conditions lead to module mismatches, which is one of the main issues in urban PV installations due to adjacent obstacles in buildings. This will become even more relevant in building-integrated PV, in particular façade-based systems. Partial shading has a strongly non-linear effect on PV outputs [150]. For a series connected PV module system even with a highly efficient MPPT algorithm partial shading may lead to almost 70% of power loss [151]. Based on the module architecture and system topology, a power-voltage (P-V) curve as a PV module characteristic may change from a concave curve with one global maximum (GM) to a curve with multiple local maxima, of which one will be the global maximum. The main challenge for this partial shading condition is to find the GM for maximum performance. The aforementioned conventional MPPT algorithms may not perform well under PS conditions. It is possible for conventional algorithms to be trapped on a local maximum [34, 152]. Many MPPT algorithms have been proposed for the PS condition [153, 154, 155, 156, 33], however they are complicated and/or require long tracking times.

An alternative way to mitigate the PS effects in a PV system is to change the configuration of the PV system depending on the variation of the shading pattern. PV system configurations have been suggested to be changed via different interconnections of individual PV modules, which are typically from one of the following configurations: (i) series-parallel (SP), (ii) total-cross-tied (TCT), and (iii) bridge-linked [34, 35]. In [157] an electrical array reconfiguration is proposed, which uses a switching matrix for changing the position of the PV modules and find the best configuration between those. This method is at the module level and implemented to maximize the available DC power by grouping modules with similar shading patterns.

Dynamic reconfiguration methods that are implemented on the module level and depend on an optimization algorithm may be very complicated and may perform at a sluggish pace. As curves with multiple maxima occur because of the effect of bypass diodes (BPD), one way to mitigate PS effects is to divide the module into groups of a small number of cells, while we note that the best option is to have one diode for each cell. Although more BPDs lead to shade-resilient modules [36], increasing the number of BPDs increases the number of local maximum peaks and subsequently a more accurate and complicated MPPT algorithm is required to find the GM of the module. Moreover, the efficiency losses with the BPDs are still significant [37]. One way to overcome this problem is to replace the ordinary BPD with an active BPD, which in fact is an electrical circuit consisting of MOSFETs (Metal-Oxide-Semiconductor Field-Effect Transistors).

Different configurations for module integrated electronics can be categorized

in the following groups: (i) Conventional systems, consisting of three BPDs per module and a central converter to change the output voltage level, (ii) Buck converters, to which normal PV modules are connected and thus the output current of the shaded module is to be controlled, (iii) Buck-Boost converters, in which configuration both current and voltage are to be controlled, and (iv) Voltage equalizers, which are a combination of different converter or even bidirectional converters to equalize the voltage by power processing [37, 158, 159].
In the present study to mitigate the PS condition, the following smart module architecture is proposed: a certain small number of solar cells are grouped and connected to a DC-DC buck converter. Connection of the buck converters then makes up the smart module. The converter is used to control the current level and also maximizes the harvested energy from the group of cells. To investigate the shade resilience different shading patterns are modeled. The performance of the smart module is tested under these shading patterns using a full year of measured irradiation data. To have a better understanding about the smart module performance the output of this module is compared with the following PV module architectures: (i) Series connected: an ordinary module with three groups of solar cells in series, there is one BPD for each group of cells to bypass the group in case of shading, (ii) Parallel connected: a module consists of three parallel strings where each string is ended with a blocking diode, (iii) Ideal module with one converter per cell, which is assumed as the ideal reference for comparison of the output of other modules. The model is developed in MATLAB. Shading patterns in the simulations contain two different varieties of shading, random and pole shading. To have an accurate understanding about the converter efficiency a least squares support vector machine (LS-SVM) as a machine learning method is implemented to find the exact value of efficiency with respect to input and output voltage and also output current. The same machine learning method is used to calculate the maximum extracted power at different times throughout the year. In all statistical analysis simulations, real data which is extracted from the Utrecht Photovoltaic Outdoor Test (UPOT) facility is used to make the result statistically tangible [93].
Generally, in the smart module architecture a buck converter in parallel with each group of cells controls the shaded groups' current by leveling down the output voltage of the converter, which simply means that the output current flow in all converters are equal. This strategy helps the shaded groups to perform efficiently while shaded. The series architecture bypasses the shaded groups because of the implemented BPDs. In parallel architecture, the lowest rated voltage determines the voltage output of the whole array, which means wasting power. In both parallel and series architectures, a fraction of power is wasted because of mentioned reasons, but in the smart module architecture all cells, even shaded ones, are pro-

ducing power efficiently and none of the cells is bypassed.
This chapter is organized as follows. Section 2 discusses the principle structure of the smart module electronics including an optimization for the best value of output. Section 3 provides different shading patterns for the architectures under study. In section 4, results from simulations in section 3 are discussed. Finally, section 5 summarizes the potential characteristics of the smart module in terms of shade resilience.

5.2 Smart PV Module Topology and Design

The proposed smart module architecture, as shown in Figure 5.1, consists of NG groups of cells with ng number of cells in each group. The total number of cells

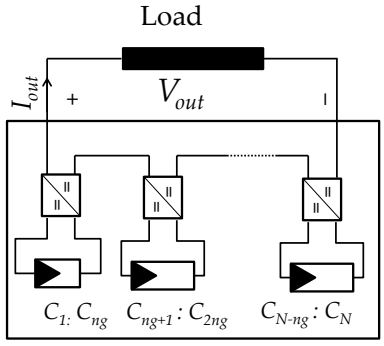

Figure 5.1 · Smart module architecture with ng cells in NG groups with electronic circuits.

in a module, N, is calculated as:

$$N = N_G \times n_g \tag{5.1}$$

PV cells in each group are connected in series and connected to a buck converter. The DC-DC buck converter is controlled via an MPPT algorithm to ensure maximum power extraction from the group. Series connected buck converters in the output of the module is due to current control. The test module for this simulation study consists of 60 monocrystalline silicon solar cells and we have access to each cell by two connection points for individual analysis. The characteristics at standard test conditions (STC is defined as 1000 W/m^2 irradiance, 25^{o}C cell temperature, Air mass (AM) 1 .5 solar spectrum) of the cells are: open circuit voltage (VOC) of 613 mV, short circuit current (ISC) of 7.92 A, maximum power (P_{max}) of 3.7 W, and efficiency (η) of 15.4%. In order to simulate a feasible system, many converters in the market have been studied and a comparison between

the most appropriate ones is shown in Table 5.1. The most suitable converter chosen for the module in this work is the LTM4611 converter from Linear Technology Corporation designs (Milpitas, CA, USA), because of the following reasons: (i) its voltage and current specifications are matched to the small groups of cells in the module; (ii) it has a higher switching frequency compared with Texas Instruments converters, which leads to better performance of the MPPT algorithm; and (iii) no extra element is required for this converter besides the chip itself, which leads to higher efficiency in the complete converter circuit. The converter efficiency de-

Table 5.1 · Comparison of different buck converters for the smart module. The colored row indicates the chosen converter.

Model	$V_{in_{min}}$	$V_{in_{max}}$	$V_{out_{min}}$	$V_{out_{max}}$	$I_{out_{max}}$	Switching Frequency	Options	Manufacturer
Unit	V				A	kHZ		
LM2744	1	16	0.5	12.8	20	50	Ext_Ref_Con[1]	TI[4]
LM2747	1	14	0.6	12	20	50	PbStUp[2] & OpClk[3]	TI[4]
LM2745	1	14	0.6	12	20	250	PbStUp[2] & OpClk[3]	TI[4]
LM2748	1	14	0.6	12	20	50	PbStUp[2]	TI[4]
LTC3713	1.5	36	0.8	32.4	20	1500	Ext_Ref_Con[1]	LT[5]
LTC3718	1.5	36	0.7	36	20	1500	Ext_Ref_Con[1]	LT[5]
LTM4611	1.5	5.5	0.8	5	15	835	Ext_Ref_Con[1]	LT[5]

1 Ext_Ref_Con: External reference controller, 2 PbStUp: Pre_Bias startup,
3 OpClk: optional clock, 4 TI: Texas Instruments (Dallas, TX, USA),
5 LT: Linear Technology Corporation designs (Milpitas, CA, USA).

pends on three different factors: input and output voltage, and output current. In Figure 5.2, the efficiency of the LTM4611 converter is depicted with these factors as parameters. The important problem is to find the optimum set of variables that lead to the maximum efficiency. To this end, the least squares support vector machine technique is implemented as a standard approach in regression analysis. This method allows to generalize the given data in the data-sheet, Figure 5.2. Therefore, all possible combinations of variables which are necessary for designing are made available in the form of a look-up table. In the following subsection, first the aforementioned method will be introduced and then its implementation for this problem is discussed.

LS-SVM for Efficiency Optimization

The least squares support vector machine method is used to generalize the performance of the LTM4611 buck converter [160]. Let us assume the training set T is a set of predetermined data:

$$T = \{(x_1, y_1), ..., (x_l, y_l)\} \tag{5.2}$$

where $x_i = [V_{in}(j), V_{out}(j), I_{out}(j)]^T$, $y_i = \eta(j)$ and $j \in [1, l]$ is the number of elements in data set T. The training set is collected from the datasheet [161]. The

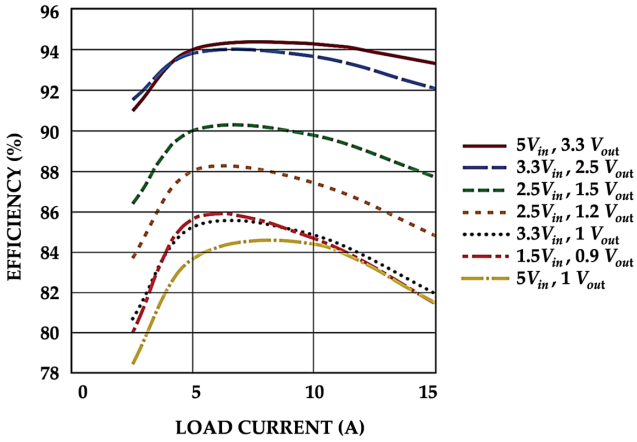

Figure 5.2 · Efficiency as a function of output (load) current for the LTM4611 converter.

LS-SVM uses the training data set T to estimate the optimal nonlinear regression function $\hat{f}$, as shown in Equation 5.3:

$$\hat{f}[x_{new}] = \sum_{i=1}^{l} \beta K[x_{new}, x_i] + b \tag{5.3}$$

where K represents a so-called kernel function and for this application, the Radial Basis Function (RBF) has been chosen as shown in Equation (3) , following [98, 160]:

$$K[x_{new}, x_i] = \exp\left(\frac{\|x_{new} - x_i\|^2}{2\sigma^2}\right) \tag{5.4}$$

where $x_{new} = [V_{in}, V_{out}, I_{out}]^T \notin T$ and the design parameters β and b are obtained by solving the matrix-vector equation shown in Equation (4):

$$\begin{bmatrix} 0 & \begin{bmatrix} 1 & 1 & \dots & 1 \end{bmatrix} \\ \begin{bmatrix} 1 \\ \vdots \\ 1_l \end{bmatrix} & [\Omega_{l\times l} + (\frac{1}{\gamma})I_{l\times l}] \end{bmatrix} \begin{bmatrix} b \\ \beta \end{bmatrix} = \begin{bmatrix} 0 \\ y \end{bmatrix} \tag{5.5}$$

Here, $I_{l\times l}$ represents the identity matrix and $\Omega_{l\times l}$ is a full matrix with computed elements from the training data as follows:

$$\Omega_{l\times l} = \exp\left(\frac{-\|x_q - x_r\|_2^2}{2\sigma^2}\right), \; q, r \in [1, l] \tag{5.6}$$

Table 5.2 · Overview of cell grouping and buck converter specifications. The colored columns indicate the cases that are selected.

Case Number	1	2	3	4	5	6	7	8	9	10
# Cells (ng)	60	30	20	15	10	6	4	3	2	1
# Groups (NG)	1	2	3	4	6	10	15	20	30	60
Vmpp (mV)*	29,412	14,706	9804	7356	4902	2941.2	1961.6	1471.2	980.8	490.4
Feasibility	No	No	No	No	Yes	Yes	Yes	No	No	No

* STC is considered as the highest reference.

Parameters σ and γ in Equations 5.5 and 5.6 are tuning parameters, which can be calculated using different methods, such as k-fold cross-validation, leave one out cross-validation, etc. [160].

The next step in the analysis is to check the feasibility of grouping cells in relation to the converter specifications. Table 5.2 lists the options under study, showing the calculated voltage at maximum power point for different cases of grouping. From the LTM4611 specification (see Table 5.1), only case number 5, 6 and 7 are feasible, as the other groupings lead to voltages outside the converter specifications.

Using all different possible combinations of variables extracted from the buck converter datasheet [161] the efficiency is computed. For instance, Figure 5.3 depicts the efficiency for input voltage Vin = 5 V, and Figure 5.4 shows how LS-SVM generalizes the data from Figure 5.3 to cover all different combinations of and in order to allow computing the efficiency. For the three different case numbers 5, 6 and 7 (Table 5.2), more information is presented in Table 5.3.

While the variation in irradiance leads to considerable linear variation in the

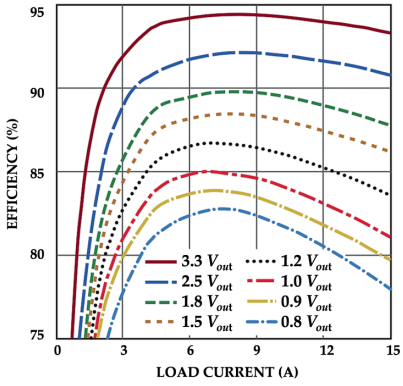

Figure 5.3 · Efficiency vs Load Current at Vin = 5 V.

output current at MPP, it influences the voltage at MPP only slightly ($\sim ln(I_{sc})$).

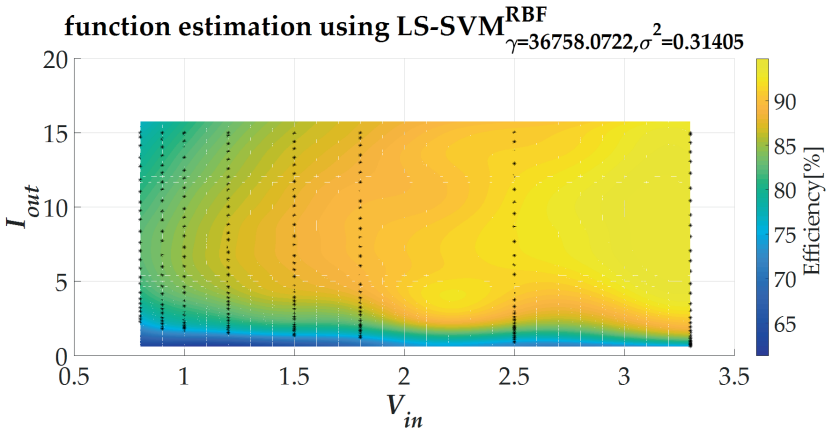

Figure 5.4 · Efficiency for all values of Vin and Iout at Vout = 5 V.

Table 5.3 · Specifications for three cases of grouping at STC.

Case Number	5	6	7
Number of Cells	10	6	4
Open Circuit Voltage (V)	6.13	3.67	2.45
Short Circuit Current (A)	7.92	7.92	7.92
Current at MPP (A)	7.54	7.54	7.54
Voltage at MPP (V)	4.902	2.941	1.961

Therefore, as a simplification, the input voltage for buck converter is assumed to be constant having the value as mentioned in Table 5.3. Although for lower irradiation levels the PV output voltage level in case 7 may not be suitable for this converter specification, all three cases are taken into consideration for comparison. The input current according to the DC-DC buck converter basics is calculated with Equation (5.7):

$$P_{out} = P_{in} \times \eta \Rightarrow V_{out} \times I_{out} = V_{in} \times I_{in} \times \eta \tag{5.7}$$

The above-described calculations lead to three contour graphs, one for each case, that are shown in Figures 5.5a-5.5d. From those, the following can be extracted:

1. Referring to the color bars, which are different per case, the highest maximum possible efficiency belongs to case 6, and the lowest maximum possible efficiency belongs to case 7.

2. The line $I_{in} = I_{MPPT}$ (where I_{MPPT} is the PV output current at STC) is depicted in all figures, thus the best possible efficiency for three cases can

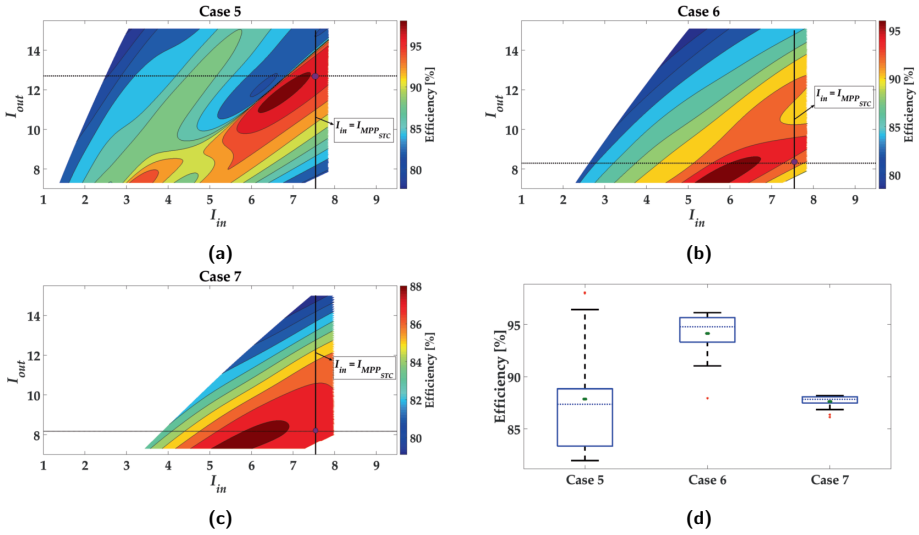

Figure 5.5 · Contour plots of efficiency as a function of input and output current: (a) case number 5, (b) case number 6, (c) case number 7. (d) efficiency variation with decreasing converter input current for 50%.

be found at intersections of these lines with the contour graphs. Therefore, the best possible efficiencies are 97.74% for case 5, 94.51% for case 6, and 87.69% for case 7.

3. It is clear that the best output current should be in the range of 11–13 A for case number 5, where $N_G = 6, n_g = 10$, and it should be 8–9 A for case number 6 with $N_G = 10, n_g = 6$, and 7–9 A for case number 7 with $N_G = 15, n_g = 4$.

4. To compare all three cases thoroughly, it is assumed that irradiation level is changed such that the PV output current changes by 50% ($\Delta I_{MPP} = 50\%$). Variation of efficiency in this situation is shown regarding the aforementioned converter output current range in Figure 5d. Although the maximum possible efficiency for case number 5 is higher, the range over which efficiency varies is wider. Also the average values for efficiency (shown in green dots in Figure 5.5d) indicate that the highest average value belongs to case number 6. That is the reason why case number 6 is chosen for the smart module grouping in this study.

5.3 Methodology

After designing the architecture and electrical topology of the smart module, let us discuss shading patterns and explain how the module is going to be modeled for this research. We consider the surface of the module to consist of $600k$ pixels, which means that each cell has $10k$ pixels (ignoring inter-cell distances for simplicity). The irradiation level on pixel p is called G_p and Equation (5.8) gives the value of this variable:

$$G_p = \begin{cases} G_{p,GHI} & \text{if it is not shaded} \\ G_{p,s} & \text{if it is shaded} \end{cases} \tag{5.8}$$

where $G_{p,GHI}$ is the global horizontal irradiance (GHI) at the pixel and $G_{p,s}$ the irradiance at the pixel under the shaded condition.

To calculate the irradiation level on each cell Equation (5.9) is used, the equation is extracted based on experimental results in a research study by Sinapis et al. [162]:

$$G_c = (F_{unshaded} \times G_{GHI}) + (F_{shaded} \times G_{dif}) \tag{5.9}$$

where $F_{unshaded} = (N_c - N_{shaded})/N_c$ is the unshaded fraction of cell C, $F_{shaded} = N_{shaded}/N_c$ is the shaded fraction of cell C, $N_C = 10000$ is the total number of pixels of cell C, N_{shaded} is the number of shaded pixel for cell C, G_{GHI} is the global horizontal irradiance, G_{dif} is the diffuse irradiance at the cell C. The most shaded cell in each group N_i determines the output current of that group Equation (5.10):

$$\forall G : I_G = f(min(G_C | C \in N_i) \tag{5.10}$$

Different Shading Patterns in This Model

The performance of the smart PV module needs to be tested under realistic shading conditions. In this study two different shading conditions are considered: (1) Random shadow, which might result from the effect of dust, bird droppings, snow, etc.; and (2) pole shadow, which is caused by a static obstacle during daylight, and which is mostly caused by pole shapes, chimneys, dormers, or a part of the building on the roof. Also, these shading conditions can be combined. In the following both types of mentioned shading conditions and the methods for generating them in the model will be described:

1. Random shape shading. The characteristics of this shading condition are: (i) probability of occurrence of this shading condition is equal for all surface pixels of the module; (ii) the shape of shading is arbitrary; (iii) random

shadows are not necessarily made by solid objects and consequently a transparency factor (F_{tr}) is defined as a random function, so that the shadow intensity is randomized; (iv) blur factor (F_{bl}) defines how wiped out the shadow borders and edges are. This blur factor is a function of the ratio of diffuse to direct irradiation (R_{dd}); (v) shadow intensity is a function of both the transparency factor and irradiance, see Figures 5.6a,5.6b.

2. Pole shading with the following characteristics: (i) pole shadow position is moving depending on the time of day, which means that the angle of the pole shadow with the module's x-axis is calculated as a function of time. The length of the pole itself is assumed to be very long so that always the pole shade covers the whole module; (ii) taking into consideration that pole shading occurs only during half of the day due to the sunlight angle, the shape of shading follows the shape of pole; (iii) shading intensity may vary depending on $G_{p,GHI}$ as the pole itself is a solid object; (iv) just as for random shading, the blur factor depends on the ratio of diffuse to direct irradiation, see Figures 5.6c,5.6d.

The blur factor is a function of the ratio of diffuse to direct irradiation and is determined using a 2D-Gaussian filter, Equation 5.11:

$$G(x,y) = \frac{1}{2\pi\sigma^2} \exp \frac{-(x^2+y^2)}{2\sigma^2} \tag{5.11}$$

where $x$and y are the distances from the origin in the vertical and horizontal axis, and σ is the standard deviation of the Gaussian distribution. In this model σ is a function of the ratio of diffuse to direct irradiation: $\sigma = f(R_{dd})$. As an example, the output power for the ten different groups in the module is shown in Figure 6 relative to the power at STC for each iteration: $\frac{P_G(i)}{P_{STC}}$.

Different Module Calculations

Total output power is computed regarding the module architecture and topology. In this section, the total output power for four different module architectures are mathematically formulated and details are discussed. The model simulates the formulated output power for all of the modules in order to allow for comparisons.

Smart Module

As shown in Figure 2.14, the smart module topology consists of some groups of PV cells connected in series and connected to a DC-DC buck converter. The DC-DC buck converter is used (i) to control the operating point on the MPP

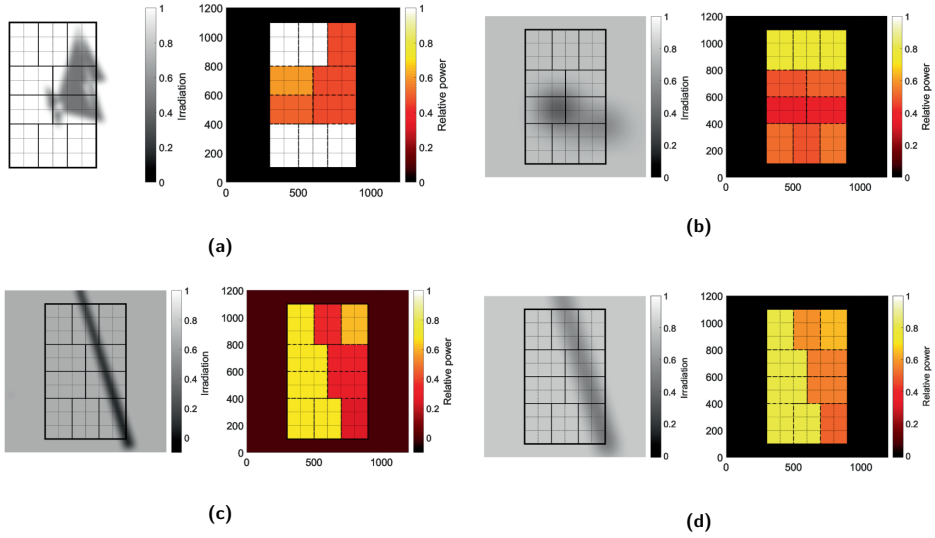

Figure 5.6 · Examples of shading pattern, (a) Random shading for higher R_{dd}, (b) Random shading for lower R_{dd}, (c) Pole shading for higher R_{dd}, (d) Pole shading for lower R_{dd}.

using an MPPT algorithm; and (ii) to control the output current flow. The series connection of buck converters on the output-side forces the converters to work with the same current flow in their output. The MPPT on the input-side of the buck converter controls the operating point to be located at MPP. The buck converter levels down the input voltage, so that the output current could be boosted for the shaded groups with the lower current flow, following Equation 5.12:

$$P_{out} = P_{in} \times \eta_{Conv} \tag{5.12}$$

where η_{Cpnv} is the converter efficiency. Total output power for the smart module is computed via:

$$P_{total-Smart} = \sum_{k=1}^{N_G} P^k_{MPP}(i) \times \eta_{Conv} \times \eta_{MPPT} \tag{5.13}$$

where N_G is the number of groups of PV cells, $P^k_{MPP}(i)$ is the maximum group output power $k \in [1 N_G]$ at iteration i, and η_{MPPT} is the MPPT algorithm efficiency. Note that in this model we assume η_{MPPT} to be constant at 95%. The LS-SVM method is used to calculate $P^k_{MPP}(i)$ by assigning $T = (x_1, y_1), \ldots, (x_l, y_l)$ where $x_j = [G(j)]^T$, $y_j = [V_{MPP(j),I_{MPP}(j)}]$, $j \in [1, l]$.

Parallel Strings with Blocking Diodes

The module with parallel-connected strings consists of three parallel strings where each string consists of 20 cells connected in series and ended with a blocking diode, see Figure 7. Normally this topology is implemented for strings of PV modules instead of PV cells. This module is controlled via a central converter with an MPPT algorithm to boost up the voltage level and control the operating point. Therefore, total output power is computed in Equation (5.14) [163]:

$$P_{total_parallel} = P_{Module_parallel_{MPP}}(i) \times \eta_{Central_{Conv}} \times \eta_{MPPT} \tag{5.14}$$

where $\eta_{Central_{Conv}}$ is the efficiency of the central converter, η_{MPPT} is the MPPT algorithm efficiency, and the maximum output power at iteration i, $P_{Module_{Parallel-MPPT}}$ is calculated in Equation (5.15):

$$P_{Module_{Parallel-MPPT}} = min(V^k(i)) \times \sum_{k=1}^{3} I^k(i) \tag{5.15}$$

Let us assume that the same MPPT algorithm is implemented for all PV mod-

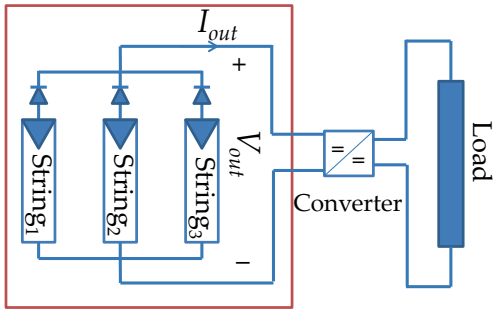

Figure 5.7 · Parallel strings with blocking diode.

ule architectures, which has the same efficiency $\eta_{MPPT} = 95\%$, as in the smart module architecture. The most appropriate converter topology which can be implemented for this module architecture is the boost converter to level up the voltage level, therefore for this study, a buck-boost converter, LT8390, is supposed to be implemented for both parallel and series connected architectures. Figure 8 depicts a variation of efficiency with respect to the input voltage and the output current (load current) for this very high-efficient converter [164]. The same LS-SVM method as mentioned for the LTM4611 is used to map the exact value of efficiency regarding the optimum module operating point.

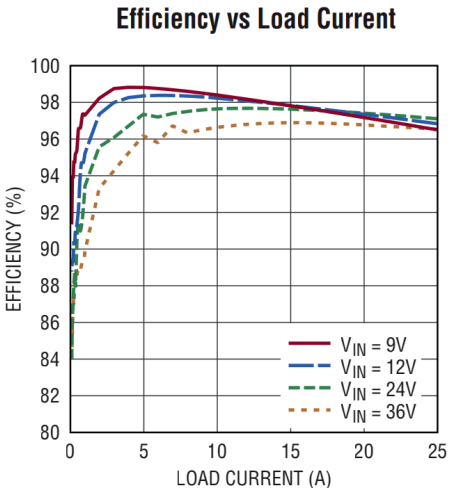

Figure 5.8 · Efficiency vs load current and input voltage for LT8390.

Standard Module, Series Strings with BPD

The standard module with series-connected strings consists of three series groups of 20 cells, where each group is equipped with one BPD, is shown in Figure 5.9. Therefore, each group of cells which is shaded would be bypassed via the BPD for preventing cell damage and hot spots and prohibiting the cell to perform as a load instead of a source. Finally, all three groups are connected in series and a central converter may be used to control the operating point. Therefore, total output power is computed using Equation (5.16):

$$P_{total_series} = P_{Module_series_{MPP}}(i) \times \eta_{Central_{Conv}} \times \eta_{MPPT} \tag{5.16}$$

where the maximum output power at iteration i, $P_{Module_series_{MPP}}(i)$ is calculated from Equation (5.17):

$$P_{Module_{Series-MPPT}} = max(I^k(i)) \times (\sum_{k=1}^{3} V^k_{nom-BP}(i) + \sum_{k=1}^{3} V^k_{d_{BP}}(i)) \tag{5.17}$$

where V^k_{nom-BP} is the voltage of none-bypassed group of cells and $V^k_{d_{BP}}$ is the forward voltage of diodes which bypasses the group of cells with lower current. It is assumed that the same MPPT algorithm and the same central converter are used as for the parallel-connected architecture.

The Ideal Module Case Study

Let us assume an ideal module, as reference for comparisons. In this ideal module for each cell a DC-DC converter is responsible to level up the current for shaded

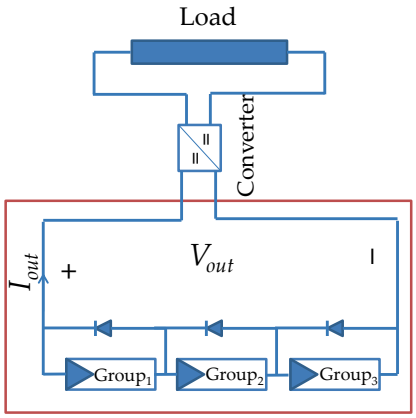

Figure 5.9 · Standard Module with three BPDs.

cells, thus the drop current because of shading is compensated (Figure 5.10). The

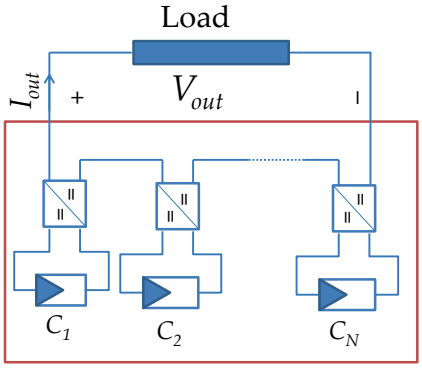

Figure 5.10 · The ideal module.

output power from the module is calculated in Equation (5.18), which is a summation of extracted power from all cell-converter modules:

$$P_{total_{Ideal}} = \sum_{k=1}^{N} (P_{MPP}^{k}(i) \times \eta_{Conv} \times \eta_{MPPT}) \tag{5.18}$$

where P_{MPP}^{k} is the maximum output power from cell k at iteration i, η_{Conv} and η_{MPPT} are assumed to be 100% and 95%, respectively, for the ideal module architecture.

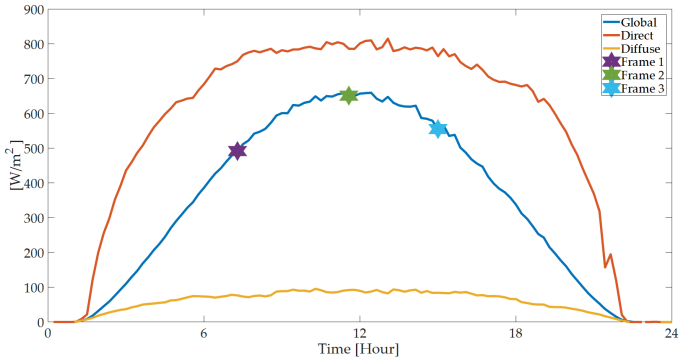

Figure 5.11 · Global, Direct and Diffuse irradiation levels on 7 September 2016.

5.4 Results and Discussion

The described model is implemented to simulate the behavior of the smart module as well as the other described architectures under different shading patterns. To understand which architecture is more shade-resilient, the harvested energy during a certain period is computed and compared for all architectures. To this end, experimental irradiance data is used as our model input, which is acquired at the Utrecht Photovoltaic Outdoor Test facility (UPOT) at Utrecht University campus in the center of the Netherlands. Irradiation measurements are done using four EKO MS-802 pyranometers (EKO Instruments, Tokyo, Japan), one EKO MS-401 pyranometer and one EKO MS-56 pyrheliometer; the measurement time is dependent on light intensity and varies from 10 milliseconds to 5 seconds. With these facilities, many variables are being measured every day like irradiation, temperature, humidity, etc. [165, 166, 167] For this research available data are (i) global irradiation level; (ii) direct irradiation level; and (iii) diffuse irradiation level for four months, i.e., January, March, June and September 2016. The following steps are followed in the analysis:

1. Figure 5.11 shows recorded data from UPOT at 7 September 2016. Three different time frames of 15 min in length are chosen to be discussed in this section and are pointed out in the figure.

2. Generate the shading patterns: following Section 5.3, two types of shadow must be generated depending on obstacles, R_{dd}, F_{bl}, F_{tr} and G_{GHI}. Figures 5.12(a-c) show different shading patterns and their effect on groups of PV cells for different architectures. Unlike in Figures 5.12b and 5.12c, which only have the effect of pole shadow, in Figure 5.12a a combination of both

pole and random shadows is shown. To observe all shading patterns during this day please refer to Figure $S1$ in the supplementary section.

3. Analysis of the effect of shading patterns on different architectures and cell groups. In this step the effective irradiation level for each group of cells in different architecture is computed precisely.

4. Maximum output power at each time frame is calculated using Equations(5.13)–(5.18). The output power for three time frames as shown in Figures 5.12(a-c) is given in Table 5.4. It is clearly shown that series connected architecture in time frame 1 performs very weak, that is the effect of BPDs in this architecture. The shade pattern in time frame 1 effects on both current and voltage significantly. The group of cells under much darker shadow are bypassed by BPD and current is very low because of the shading.

5. Each time frame simulates 15 min of the real world with the assumption of having a constant value of irradiation variables.

Table 5.4 · Output power in three time-frames.

Architecture	**Frame 1**	**Frame 2**	**Frame 3**
Ideal Architecture	48.35 (W)	84.23 (W)	116.54 (W)
Smart Architecture	18.49 (W)	69.00 (W)	108.85 (W)
Series Connected Architecture	0.84 (W)	30.95 (W)	112.35 (W)
Parallel Connected Architecture	4.51 (W)	62.97 (W)	113.42 (W)

Figure 5.13 depicts the output energy from different module architectures for different months of the year 2016. The output energy in January is the lowest compared to the other three months. In all three other months, it is clearly shown that the ideal module outperforms all other modules, which is the effect of both the architecture and the 100% and 95% efficiency that is considered for the converter and MPPT algorithm, respectively. For all three months of March, June, and September the second-best performing module is the smart module, followed by the parallel connected and the series connected module. Generally, the drawback of the parallel-connected module is its very low voltage compared to the series-connected module. For designing a practical PV system voltage levels need to be boosted up with a central DC-DC converter and then be controlled to be compatible with the load specifications. In contrast, the series-connected module, which performs worst of all architectures, does not need the boost up the level between load, which thus makes the whole system design easier and more cost efficient. Figure 5.14 shows the ratio of output energy from the modules with

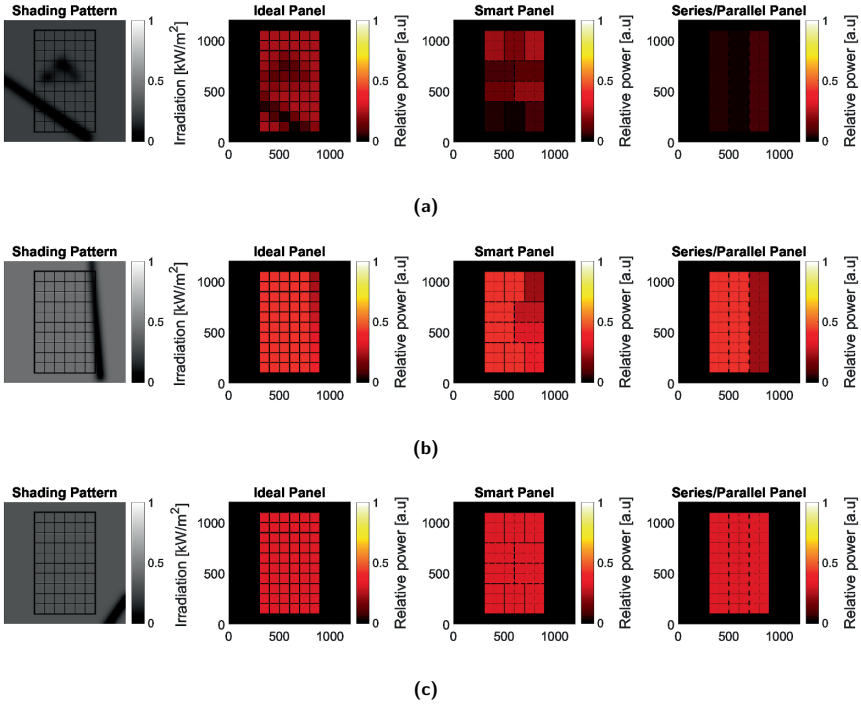

Figure 5.12 · (a) Combined pole and random shading pattern and effect of that on different architectures at time frame 1,(b) Pole shading pattern and effect of that on different architectures at time frame 2,(c) Pole shading pattern and effect of that on different architectures at time frame 3. Note that the shade is not cast on the panel.

respect to the output from the ideal module, Equation (5.19):

$$R_E(\%) = \frac{E_m}{E_{ideal}} \times 100, m \in [\text{smart,series connected, parallel connected} \quad (5.19)$$

Excluding January and the days with very low output energy the smart module performs much better compared to the rest of architectures excluding the ideal module. On the other hand, the series connected module for most of the time generates the lowest amount of energy. The summation of output energy and the average for the whole year 2016 are depicted in Figure 5.15. To sum up, the performance of the smart module outperforms all other architectures, except for the ideal module, for all months excluding winter time when the output energy in all types of architecture is almost zero. However, the series connected module as the most ordinary architecture implemented nowadays by most of the manufacturers is performing worst. Figure 5.16 shows the ratio between total harvested energy from smart module, series and connected modules compared to the ideal module. It shows that the smart module harvested almost 79.5% of the energy that the

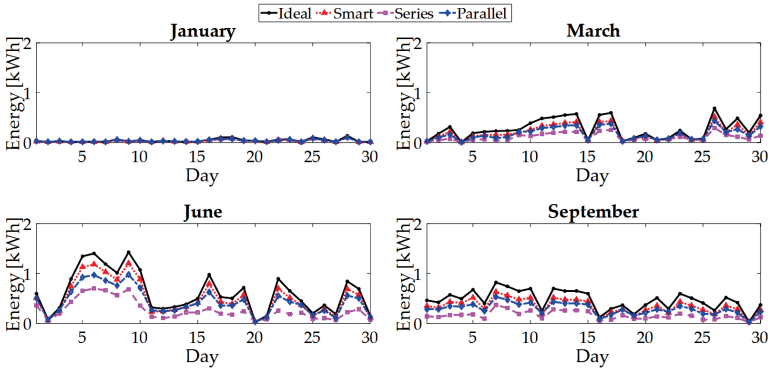

Figure 5.13 · Harvested energy at four different months of the year 2016.

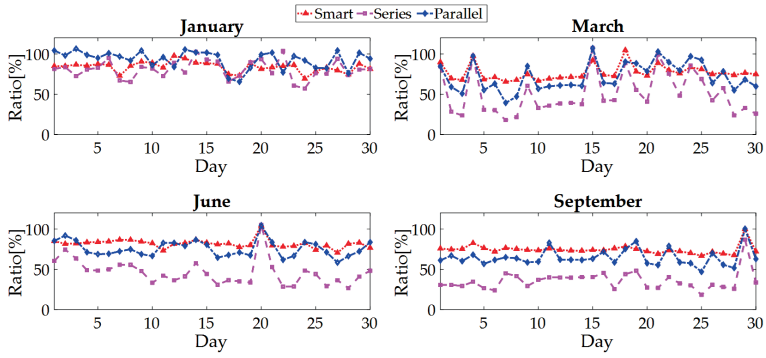

Figure 5.14 · The ratio of harvested energy of different architecture compare to ideal module at four different months of the year 2016.

ideal module harvests; the series connected harvested 42.2% and parallel connected yield 68.8% of total module capacity under the same shading patterns.The method discussed and improved in this study is based on the fact that even small amounts of power which can be produced by cells should be harvested. In other feasible architectures, series and parallel, there are always some energy losses due to the electrical connections. In parallel connection, as the lowest voltage group always determines the module output voltage a fraction of power is lost. As shown in Figure 5.16 this energy loss is almost 31.2% of total capacity. For series connection, once the BPDs (used for safety reasons), are forward biased in anti-parallel position with shaded groups of cells those groups are bypassed and the module output voltage is decrease. This behavior of BPDs wastes some energy, and this loss is more than half of total capacity: 57.8%. For the smart module, although there is some loss in the electronic circuits due to converter efficiency the final loss compared to the other architectures is reasonably low. According to the results

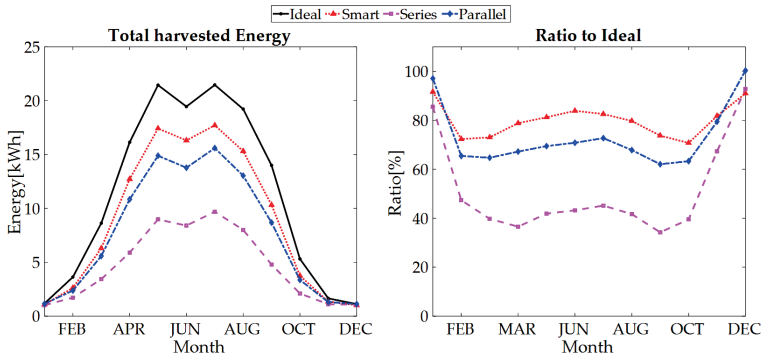

Figure 5.15 · Perspective of total harvested energy during different months in 2016.

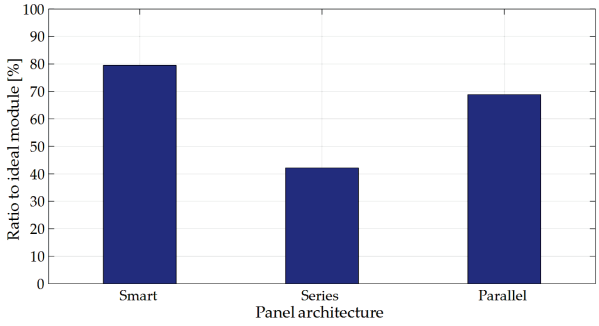

Figure 5.16 · Ratio of total harvested energy from smart module, series and connected modules compared to the ideal module under shading patterns.

in Figure 5.16 only 20.5% of energy is lost compared to the ideal module. More importantly, the smart PV module performed 47% and 13.4% better, compared to the series connected and the parallel connected architectures, respectively. The energy loss for the smart module strongly depends on the following factors: (i) optimization of the grouping (number of cells in each group); (ii) converter choosing; and (iii) load current. It should be noted that the actual power rating of the modules, i.e., watt-peak determined under standard test conditions of 1000 W/m^2 actually is the same (or very similar) for all three architectures. For unshaded conditions throughout the year, also the energy rating (kWh/kWp) would be the same (or similar). However, for shading conditions, the harvested amount of energy clearly differs. In fact, it could be recommended to develop new standards to test modules under standardized shading conditions.

The addition of electronic elements in a module will lead to additional cost, which should be offset with additional energy harvested under shading conditions.

Let us consider the tradeoff between cost and harvested energy comparing both ordinary and smart modules. As the most commonly-used architecture in the market is the series connected architecture, we compare the series connected module with the proposed smart module. According to [168], a public awareness agency funded by the Dutch government, the price of buying a PV system is 1.5 €/W of which panel cost is about half. Thus, a typical panel of 220 W would costs about €170. For transforming an ordinary panel to a smart one we need to purchase 10 micro converters, a microprocessor, and some electronics elements. In this study the designed micro converter is LTM4611, which costs €16, the microprocessor is about €25 and the rest of elements costs roughly €35. To sum up, the final expenditure for a smart panel is about 1.66 times more than an ordinary panel, but as Figure 18 shows under the shading patterns, the annual harvested energy from smart module is 1.89 times more than the series connected. Thus, the economic payback time for a smart module compared to an ordinary series connected module (in shading conditions) is shorter. Note that cost of electronic components are based here on purchasing small amounts. It can be expected that large volume purchases lead to substantial limited additional costs for smart module architectures. Finally, besides the increased resilience to shading effects, it can be expected that the occurrence of hot spots in smart modules will be limited as well. In a further experimental study, we will investigate that using Infrared (IR) thermography.

5.5 Conclusions

To mitigate partial shading effects on the performance of PV modules, a generic model is developed that is able to evaluate smart PV module architectures. In this chapter the proposed architecture consisted of a number of PV cell groups, and a DC-DC buck converter for a group of PV cells is implemented to amplify the current of shaded groups. This converter was chosen after investigation of characteristics of appropriate micro-converters in the market with respect to the PV cell specifications. This resulted in the choice for the Linear Technology LTM4611 converter. The LS-SVM method was used (i) to generalize the behavior of the converter efficiency; and (ii) to optimize the group size of PV cells. In summary, the optimum grouping for the designed specifications was 10 groups of 6 cells. After the smart module was designed, the effect of shading patterns was studied. A model for shading patterns was developed with two types of random and pole shadows based on actual measured irradiation data. Simulations demonstrated that the average amount of generated energy of the smart architecture was almost 79.5% of the energy generated by the ideal PV module. Compared with series

connected and parallel connected architectures, the smart PV module performed 47% and 13.4% better, respectively. Moreover, the smart module economic payback time compared with the most commonly-used architecture in the market is expected to be shorter.

5.6 Supplementary Materials

The following are available online at www.mdpi.com/link.
Figure S1: Shading pattern and different architecture behaviors during the day 7 September 2016. Photographs of experimental system.

5.7 Acknowledgments

The authors gratefully acknowledge fruitful discussions with Rudi Jonkman and Robert van der Sanden (Heliox), Lenneke Sloof (ECN), and Hamed Yousefi Mesri (UMC). This work is partly financially supported by the Netherlands Enterprise Agency (RVO) within the framework of the Dutch Topsector Energy (project Scalable Shade Tolerant Modules, SSTM).

6

Proof of Concept for a Novel and Smart Shade Resilient Photovoltaic Module

This chapter is based on the paper:
S.Z. Mirbagheri Golroodbari, A.C. De Waal, W.G.J.H.M. van Sark, *Proof of Concept for a Novel and Smart Shade Resilient Photovoltaic Module*, IET-Renewable Power Generation, 13 (2019) 2184-2194.

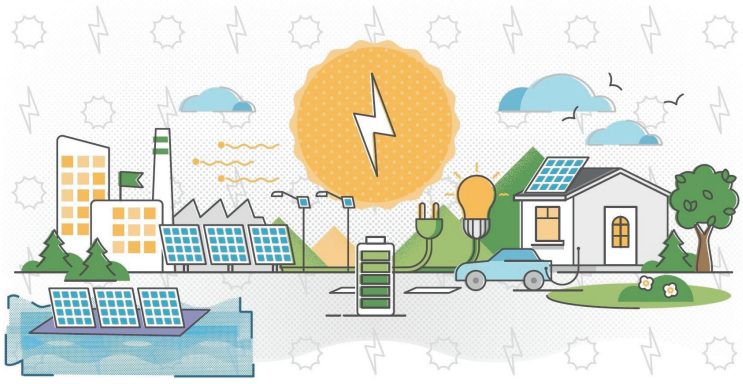

Abstract

In this paper, performance of a shade resilient smart module is studied under a dynamic shading pattern. A smart module architecture is developed to mitigate the non-linear shading effect on the module performance. Partial shading decreases the output current of the shaded cells and affects the unshaded cells' output power. After distributing the module cells into small groups, based on a least square support vector machine optimization method, DC-DC buck converters compensate the decreased current levels, by adjusting the output current and voltage level from any individual group of cells. The system is simulated in the MATLAB Simulink environment and the output results is presented. Results show that the module performs efficiently and output power of the unshaded groups of cells never decreased because of the effect of shading on the other groups. Additionally, maximum output power is harvested from all groups simultaneously. Prototype hardware is designed and built to implement the proof of concept. The real time results of hardware testing shows that the smart module performs as expected and mitigates partially shaded conditions by extracting maximum power from each group, regardless of other groups shading condition.

6.1 Introduction

Every year the solar industry is breaking new records, e.g. the global Photovoltaic (PV) market grew significantly to at least 74.4 GW in 2016 [147]. In the year 2017, 29 countries exceeded the gigawatt (GW) mark and as a result the global PV market rose for the first time to at least 98 GW, which is more than 32% increase in a year [169]. However, analysis of energy yields reveals that the optimum performance is not always obtained and it is affected by the ambient conditions, and shading is a prominent cause of performance loss [18]. Thus, to harvest energy from a PV module, proper maximum power point tracking (MPPT) is needed, as well as DC to AC conversion. Minimizing the effects of shading on modules has been proposed by several authors such as by usiing complicated MPPT algorithms, dynamic reconfiguration (DR) methods, voltage equalizers, etc. [149, 34, 37, 170, 171].

As an interface between module and load, a MPPT is implemented to both control and maximize the output PV power via a MPPT algorithm. A significant number of MPPT algorithms have been presented in the literature, which can mainly be categorized in three different groups: (i) "Quasi seeking" known as offline methods, which depend on the physical aspects of the module and mathematical models, e.g. curve-fitting, open circuit voltage or short circuit current

methods [172, 173]; (ii) "True seeking" also called online methods, which are based on measured data from the panel. Most of the conventional MPPT algorithms which are basically gradient descent based and also denoted as hill climbing algorithms are classified in this group, e.g. perturb and observe (P&O) and incremental conductance (Inc. Cond) [174, 175, 176]; (iii) Hybrid methods which are either categorised as a combination of online and offline methods [177, 152, 178] or are responsible for both MPP tracking and output voltage controlling [179, 180]

It is indicated in many studies that conventional MPPT methods perform much better under non-shaded conditions and other methods are either imprecise or knotty [177, 152]. A concave power-voltage (P-V) curve as a characteristics specification of a PV module could be changed due to performance of bypass diodes (BPDs) in mismatch conditions (MC). The nonlinear effect of MC changes the P-V curve to a cluster of concave curves; as a result instead of only one maximum, the P-V curve has several local maxima and only one global maximum (GM). One may say that a solution to mitigate MC effects, is to equip every single cell with one BPD, while we noted that although more BPDs lead to shade-resilient modules [36], first, the consequential efficiency losses with the BPDs should be considered and also, the number of BPDs has a direct relation with the number of local maxima [37]. It is indicated in much reports that the conventional MPPT methods may fail to find the GM or recognize the first local maximum instead of that [152, 177]. To mitigate the MC or partial shading condition (PSC) researchers either developed the conventional methods [181, 182] or frequently turned to implement AI e.g. evolutionary algorithms (EA), Fuzzy logic (FL) methods, genetic algorithm (GA), particle swarm optimization (PSO), etc. Aside from the complexity of AI methods, it can be concluded that the nonlinear effect caused by MC, will either decrease the efficiency and accuracy of the MPPT algorithms or give a sluggish performance [183, 177].

An alternative solution for the nonlinear effect of MC is to change the PV configuration which is known as dynamic reconfiguration (DR)[171]. These methods, mostly implemented on the module level, clearly utilize an optimization algorithm. These algorithms are to find the optimum configuration to mitigate shading effects by choosing between (i) series-parallel (SP); (ii) total-cross-tied (TCT); and (iii) bridge-linked module connection schemes and may be very complicated and markedly slow [184, 34].

Another alternative for mitigation of nonlinear MC effect is called distributed MPPT (DMPPT), where first divide the cells in the module in smaller groups of cells and then instead of using a passive BPD implement an active BPD for each group of cells. An active BPD is an electrical circuit consisting of Metal-Oxide-Semiconductor Field-Effect Transistors (MOSFETs), which could be controlled via

a duty cycle as the control signal. Such a configuration from now on is referred to as module integrated electronics (MIE) in this work. MIEs can implement either (*i*) a buck converter, (*ii*) a buck-boost converter, or (*iii*) a voltage equalizer[37, 158]. In conventional modules, the cells are divided in some groups (mainly three) of series connected cells and each group comes equipped with one BPD; then, the module supplies power to the MPPT converter, and the MPPT algorithm optimizes the amount of harvested energy. MIEs using buck or buck-boost converters are o potential interest to control current or voltage and current of the shaded group. Voltage equalizers, which are a combination of different converters or even bidirectional converters to equalize the voltage by power processing.

In literature, there are several number of MPPT algorithm developed by researchers to maximize the harvested energy from the PV system. In [185], to track the MPP, the PV module instantaneous power is compared to a varying power reference generating by the MPPT algorithm. The algorithm is based on two-loop control approach. The inner loop uses a sliding-mode strategy and the outer loop is based on the MPPT algorithm generating the appropriate value of the static conductance required by the inner loop. However, because of the following reasons this method is not recommended for a small group of cells: (i) the complexity of this method making the tracking time long and (ii) the voluminous electronics circuits makes it impossible to mount it at the junction box. Researchers in [186] propose a PSO-based maximum power point tracking algorithm for dynamic environmental conditions. However, the simplicity and pace of algorithm is very important for a system with few number of cells and low voltage level.

There are quite a number of studies on DMPPT in published papers. In [187], single-switch voltage equalizers using multi-stacked buck-boost converters are implement to mitigate the MC issues. The proposed voltage equalizers can be derived by stacking capacitor-inductor-diode (CLD) filters on traditional buck-boost converters, such as SEPIC, Zeta, and Ćuk converters. Although this technique is easy to install as it does not need local sensors and communication system, but it does not guarantee that all solar modules or cells perform at MPP. To make sure that the technique can both mitigates the MC and also performs at MPP, in [188] a distributed PV system architecture is proposed, the system requires one sensor,and the SS-MPPT method is implemented for this architecture [189]. The authors develop a new architecture to reduce the cost for the system, but the complexity of the system and relatively slow MPPT algorithm are drawbacks of this method.

In this chapter, we employ the method for mitigating the partial shading condition as one of the most frequent mismatch and performance loss conditions. The main idea is to design a panel consisting several group of cells, such that each

group is equipped with one individual micro converter for MPPT algorithm. The novelity in this research is that this method is in the panel order and the final control circuit is small enough to be mounted at the back of the panel in the junction box, thus smart panel can be a more efficient replacement for the conventional panel. The smart panel can be implemented standalone or grid-connected e.g. on the roof tops or facades for the building-integrated photovoltaics (BIPV) systems.

The smart module in this study is a MIE which is designed as follows. First, a least square support vector machine (LS-SVM) algorithm is used to optimize the number of cells per group, a generic study on this optimization and design and also, annual analysis with real data for year 2016 with different shading pattern is published in [184]. Each group of cell supplies power to a micro-converter which is controlled by means of a sampling-based MPPT algorithm (Sweep Method MPPT (SM-MPPT)). This algorithm implements two main functions, $SubGradients$ and $find(D_{max})$, to maximize the harvested energy. The $SubGradients$ function is implemented to recognize the change either in temperature or irradiation level which can cause the output power to vary. The $find(D_{max})$ is a sampling function which accurately finds the optimum duty cycle for the selected group of cells. Because of the system topology, the output current flow in all converters is equal as all converters are in series in their outputs. This strategy extracts as much power as each group of cell could generate, even though some groups may be very heavily shaded. The conventional system bypasses the shaded groups because of the implemented BPDs, but in the smart module architecture all cells, even shaded ones, are producing power efficiently and none of the cells is bypassed.

In this study, we will discuss in details about the topology, MPPT algorithm and electronics circuit design of the system. To investigate the feasibility of the smart module the MATLAB/SIMULINK environment is used to simulate the module and to test both its maximum power point tracking time and accuracy. Also a hardware prototype is built as a proof of concept. The prototype shows (i) how energy harvesting from each group individually is possible, (ii) how each group of cells could follow the irradiation change, (iii) to find the maximum power regardless of connected load. The hardware is tested under a partial shading condition and data from all groups of cells is recorded.

This chapter is organized as follows: Section 2 discusses the design, and control of the system, all details about the MPPT algorithm and variable assignments are in this section. Section 3 shows the simulation results, and Section 4 describes the hardware design as well as discusses the recorded data. Section 5 closes the chapter with conclusion and recommendations.

Table 6.1 · Specifications for one cell

V_{MPP}	I_{MPP}	V_{OC}	I_{SC}	FF	Efficiency (η)
$0.49V$	$7.54A$	$0.61V$	$7.92A$	0.765	16.4%

Table 6.2 · LTM4611 specifications

Vin_{min}	Vin_{max}	$Vout_{min}$	$Vout_{max}$	$Iout_{max}$	SF*
$1.5V$	$5.5V$	$0.8V$	$5V$	$15A$	$835Hz$

* Switching Frequency

6.2 Methodology

The optimum number of cells per group and converter selection has been found regarding the following issues: (i) PV cell characteristics, (ii) available micro DC-DC converters in the market, (iii) efficiency of the smart module under different shading patterns. This optimization part of our study has been published in [184], and is briefly explained in the following subsection.

Specifications of PV cell and the chosen buck converter are shown in Table 6.1 and Table 6.2. Regarding the available micro DC-DC converters in the market the best option which was compatible with our PV cells was the one from Linear Technology: LTM4611 [161].

Least Square Support Vector Machine

For a generic study about the system, it is required to generalize the performance of the LTM4611 buck converter. To this end, the converter should be modeled with a regression function regarding its inputs (x) and outputs (y). The Least Square Support Vector Machine (LS-SVM) is a good method to use as it constitutes a set of related supervised learning methods which are used for both classification and regression analysis[97]. In a generic study in [184] we used the LS-SVM method to find the aforementioned regression function. The study is briefly introduced in the following two paragraphs.

A a set of predetermined data from the converter datasheet is considered as the training set and is called T:

$$\begin{aligned} T &= \{(x_1, y_1), \ldots, (x_l, y_l)\} \\ x_j &= [V_{in}(j),\ V_{out}(j),\ I_{out}(j)]^T, y_j = \eta(j) \end{aligned} \tag{6.1}$$

where $j \in [1, l]$ is the number of elements in data set T [161]. The training data set T is used to estimate the optimal nonlinear regression function $\hat{f}$, as shown in

Equation (6.2).

$$\hat{f}(x_{new}) = \sum_{i=1}^{l} \beta K(x_{new}, x_i) + b \tag{6.2}$$

where K represents a so-called kernel function and for this application, the Radial Basis Function (RBF) has been chosen as shown in the following

$$K(x_{new}, x_i) = exp(\frac{-\|x_{new} - x_i\|^2}{2\sigma^2}) \tag{6.3}$$

where $x_{new} = [V_{in}, V_{out}, I_{out}]^T \notin T$, and the design parameters β and b are obtained by solving the matrix-vector equation shown in Equation (6.4):

$$\begin{bmatrix} 0 & \begin{bmatrix} 1 & 1 & ... & 1 \end{bmatrix} \\ \begin{bmatrix} 1 \\ 1 \\ \vdots \\ 1 \end{bmatrix} & \begin{bmatrix} \Omega_{l\times l} + (\frac{1}{\gamma})I_{l\times l} \end{bmatrix} \end{bmatrix} \begin{bmatrix} b \\ \beta \end{bmatrix} = \begin{bmatrix} 0 \\ y \end{bmatrix} \tag{6.4}$$

Here, $I_{l\times l}$ represents the identity matrix and $\Omega_{l\times l}$ is a $l \times l$ full matrix with computed elements from the training data as follows:

$$\Omega_{l\times l} = exp(\frac{-\|x_q - x_r\|^2}{2\sigma^2}), q, r = 1, \cdots, l \tag{6.5}$$

Parameters η and γ in Equations (6.4) and (6.5) are tuning parameters, which can be calculated using different methods, such as k-fold cross-validation, leave one out cross-validation, etc [97].

For a panel of sixty cells there are only three possible combination of cells considering the cells and converters specification. Implementing the LS-SVM method for optimization made us conclude that the combination of six cells per group was the optimum case [184]. Therefore, a panel of sixty cells, with individual access to each cell, was divided into ten groups of cells, and buck converters will harvest energy from all groups of the cells.

In this chapter, design and simulation of the hardware prototype, as well as the energy harvesting method will be discussed. The architecture of the smart panel which is used in this study is depicted in Figure 6.1. The energy harvesting method in this study is a sampling-based maximum power point tracking algorithm, and will be discussed in detail in this section. Moreover, the electronics circuits required for this study are designed and prepared by us from scratch.

Architecture

Figure 6.1 shows the architecture of the smart panel. The total number of cells in the module is N and calculated as $N = N_G \times n_g$, where N_G is the number of groups in a module and n_g is the number of cells in each group. The micro-converter, for each group, is individually controlled via duty cycle $D_i, i \in [1, N_G]$ which is computed via the SM-MPPT algorithm. As mentioned above, the optimum values

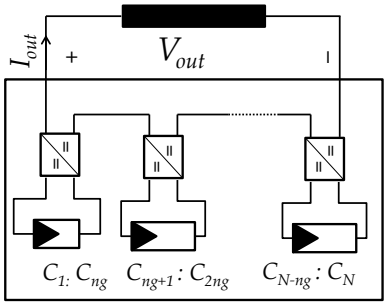

Figure 6.1 · Smart module architecture

for N_G and n_g have been calculated as $N_G = 10$ and $n_g = 6$ [184]. Therefore, as the same architecture will be used for the hardware design, we followed the same numbers in this study as well.

PV cell model

A PV cell is modeled with a current source, I_{PH}, in parallel with a diode, D; R_P and R_S are a resistance in parallel and series with that combination, respectively. More accurate models contain two or three diodes [190]. The equivalent circuit of the one-diode model is displayed in Figure 6.2.

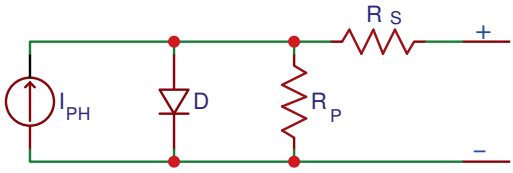

Figure 6.2 · PV cell equivalent circuit

$$I_{PV} = I_{PH} - I_D - I_{R_P} \tag{6.6}$$

$$I_{PV} = I_{PH} - I_s(\exp(\frac{V_{PV} + IR_S}{mV_T}) - 1) - \frac{V_{PV} + IR_S}{R_P} \tag{6.7}$$

$$V_T = \frac{N_s K_b T}{q} \tag{6.8}$$

where I_{PH} and I_s are the photon and saturation current of PV module, respectively, K_b is the Boltzmann constant, m is the diode ideality factor, T is the reference temperature (K), q is the electron charge, and N_s is the number of cells connected in series. Due to the small voltage level of PV cells it is necessary to connect them in series to boost up the voltage level.

Buck converter model

A block diagram of a basic buck converter is depicted in Figure 6.3. The output voltage of this converter is computed as

$$V_{out} = d \times V_{in}, \ d \in [0, 1] \tag{6.9}$$

where d is the duty cycle and therefore, $V_{out} \leq V_{in}$. The converter is modeled

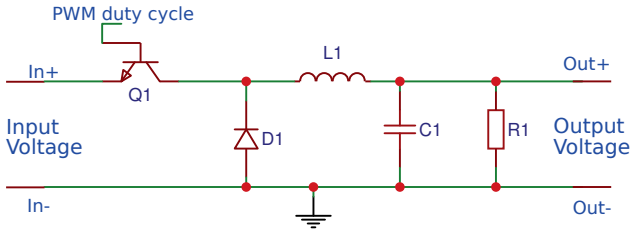

Figure 6.3 · Block diagram of a basic buck converter.

using the state space averaging method [191]. Therefore, the converter can be described by a single equation approximately over a number of switching cycles. The equation includes both the independent voltages and currents and also the duty cycle ratio. State equations are derived considering the on/off time of the switch Q_1 and diode D_1 as follows:

$$if \begin{cases} Q_1 : on & \Rightarrow \dot{x}(t) = A_1 x(t) + B_1 u(t) \\ Q_1 : off & \Rightarrow \dot{x}(t) = A_2 x(t) + B_2 u(t) \end{cases} \tag{6.10}$$

where $x(t)$ is state variable vector and $A_i, B_i, i \in [1, 2]$ are system matrices and $u(t)$ is the system input. The general state space model of the system is calculated as

$$\begin{cases} \dot{x}(t) = Ax(t) + Bu(t) \\ y(t) = Cx(t) + Du(t) \end{cases} \tag{6.11}$$

where A and B are defined as follows:

$$\begin{cases} A = dA_1 + (1-d)A_2 \\ B = dB_1 + (1-d)B_2 \end{cases} \tag{6.12}$$

Considering inductor current (i_L) and capacitor voltage (V_c) describing x like $x = [i_L \ V_c]^T$, $y(t) = [0 \ \ 1] \ x(t)$ and applying Kirchoff's laws we will have matrices for state space model of the system in Equation 6.13.

$$A = \begin{bmatrix} 0 & \frac{-1}{L_1} \\ \frac{1}{C_1} & \frac{-1}{R_1 C_1} \end{bmatrix}, \ B = \begin{bmatrix} \frac{d}{L_1} \\ 0 \end{bmatrix}, \ C = [0 \ 1], \ D = 0 \tag{6.13}$$

The transfer function of the buck converter is defined as linear mapping of the Laplace transform of input $U(s) = \mathcal{L}\{u(t)\}$ to the Laplace transform of output $Y(s) = \mathcal{L}\{y(t)\}$ and is derived in Equation 6.14.

$$G(s) \times U(s) = Y(s) \tag{6.14}$$

$$G(s) = C(sI - A)^{-1}B + D \tag{6.15}$$

Regarding the built in inductor and capacitor values in LTM4611 and the possible external capacitor for the system mentioned in [161], the transfer function for the system, in the s-plane, is derived as stated in Equation 6.16.

$$G(s) = \frac{d \times 5 \times 10^{13}}{s^2 + 5 \times 10^5 \ s + 5 \times 10^{13}} \tag{6.16}$$

The settling time for a linear system to step changes in the input can be approximated by the following formula

$$t_s = 4/\sigma \tag{6.17}$$

where σ is the absolute of the real value of the most dominant pair of the complex conjugate poles. Regarding the above-mentioned calculations, in this system the settling time for the buck converter itself is 16μs. However, as we would like to implement the chip and noting that the chip consists besides the buck converter also some other units without enough technical information to model, the settling time for the full chip needs to be investigated. In the following subsection, LTSpice software is used to investigate the exact settling time for the chip which is expected to be longer the the buck converter settling time.

Sweep Method MPPT Algorithm

In this study, a sweep method MPPT (SM-MPPT) algorithm as a sampling-based method is proposed. The sampling frequency (f_{sp}) in this algorithm is related to

the settling time of the LTM4611. As mentioned before, LTSpice software [192] is implemented to study the step response of LTM4611 with different output voltage levels, using micro-converter data from its datasheet [161].

Figure 6.4 shows step responses to the input voltage $V_{in} = 3.2$V with dif-

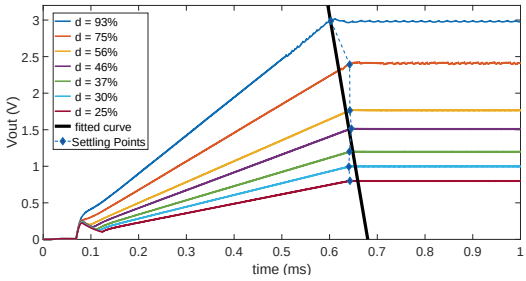

Figure 6.4 · Step response of LTM4611 with $V_{in} = 3.2$V

ferent duty cycles that cause different output voltage levels. The blue points in the figure indicate when the dynamic system reached the steady state condition. With linear curve fitting technique, the function for the black line in the figure is computed with the following equation $V_{out} = (3.8 \times 10^4)t + 26$. By solving this equation the maximum value for settling time is $t_{s_{max}} = 0.6842$ms. Thus, the minimum value for the sampling frequency, $f_{sp_{min}}$, can be calculated from $f_{sp_{min}} = 1/t_{sp_{max}}$ where $t_{sp_{max}}$ is the maximum value for the sampling time and wer find $t_{sp_{max}} = t_{s_{max}} = 0.6842$ms; as a result, in the SM-MPPT algorithm f_{sp} is set to $f_{sp} \leq 1.4$kHz which is compatible with the chosen converter, as the sampling frequency is specified as 835 Hz (Table 2).

The SM-MPPT algorithm is based on a high-frequency sampling method and by sweeping the duty cycle over the entire search space, the optimum operating point can be found. Shown in Figure 6.5, the algorithm starts its work with initialization and continues with two main functions of $find(D_{max})$ and $SubGradients$. The $find(D_{max})$ function is implemented to find the optimum duty cycle for the ongoing condition in one iteration. Each iteration consists of $n \in \mathbb{N}$ samples. Two other coefficients k and m are used to adjust the duty cycle precision; in this simulation, with $n = 10$, $m = 5$ and $k = 2$. Additionally, the sampling frequency as mentioned before depends on the converter settling time and is equal to 1.4kHz.

The $SubGradients$ function is implemented to check if the operating point is moved. This may occur because of either an irradiation or temperature change.Two sub-gradients $\partial P/\partial V$ and $\partial P/\partial I$, as stated in equations 6.18 and 6.19 are used to indicate if the operating point moves.

$$\frac{\partial P}{\partial V} = \frac{P_{t+t_{sp}} - P_t}{V_{t+t_{sp}} - V_t} \tag{6.18}$$

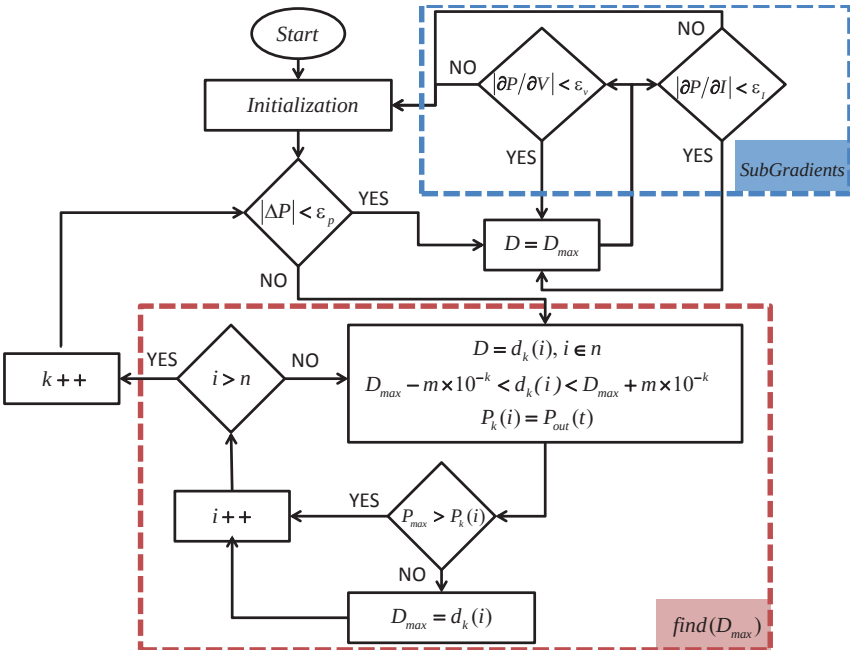

Figure 6.5 · Sweep method MPPT algorithm flowchart

$$\frac{\partial P}{\partial I} = \frac{P_{t+t_{sp}} - P_t}{I_{t+t_{sp}} - I_t} \tag{6.19}$$

where $\Gamma_j, \Gamma \in (V, I, P)$ is the output variable at time j and V, I, and P are voltage current and power, respectively; t_{sp} is the sampling time and equal to $t_{sp} = 1/f_{sp}$. If the *SubGradients* function recognizes that the operating point is moved, the algorithm restarts from the initialization step. Duty cycle (D) as the control signal for micro-converter, is generated n times in each iteration,

$$D = d_k(i), i \in n \tag{6.20}$$

The output power from the PV cells group is compared with previous output powers in the iteration. The maximum power and its matching duty cycle are recorded as P_{max} and D_{max}, respectively.

$$P_k(i) = P_{out}(t) \tag{6.21}$$

6.3 Simulations

The smart module has been simulated in MATLAB Simulink environment for a dynamically changing shading condition, which is caused by a moving object casting a shadow on the smart module. The PV cell and buck converter models are implemented in the simulation as discussed in the methodology section.

Results and discussions

It is assumed that the object moves in three time windows within 0.2s, and the performance of smart panel is studied in these time windows (TW). Figure 6.6 shows the position of shadow in each TW, it shows the position of shading the module. As shown in this figure, smart module consists of ten groups of six cells, numbered 1 to 10, and the conventional module consists of three series strings, shown in red with PS_i, $i \in [1,3]$. Figure 6.7 depicts output power from both modules. The darker shades on PS_1 and PS_2 is the reason why these two strings are bypassed with the BPDs and the only effective string is PS_3 in the depicted PSC.

In this condition, we assume that global horizontal irradiance is $GHI =$

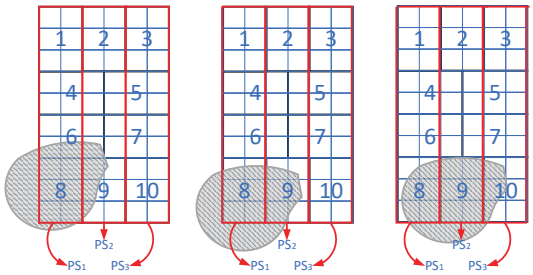

Figure 6.6 · Shadow position for the three time windows

$1000\text{W}/m^2$ and diffuse irradiance is equal to $G_{dif} = 700\text{W}/m^2$. The irradiance over the cell is calculated with equation 6.22 [162]:

$$G_c = (F_{shaded} \times G_{dif}) + (F_{unshaded} \times G_{GHI}) \tag{6.22}$$

where F_{shaded} and $F_{unshaded}$ are shaded and unshaded fractions of the cell area. Also, the cell with the lowest amount of irradiance determines the output from each group, in the smart module, or string, in the conventional module. A brief comparison between the conventional (C) and the smart (S) module in this test is tabulated in Table 6.3. $P_{Out_S}(W)$ and $P_{Out_C}(W)$ indicate the output power extracted from the smart and conventional module, respectively. It can be concluded

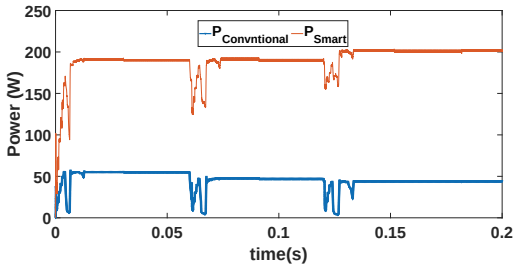

Figure 6.7 · Output power of the smart (orange line) and conventional (blue line) module

that the smart module topology extracts 3.5 times more energy, on average, from the same cells, compared with the conventional series string module topology.

Table 6.3 · Smart and Conventional module performance in the partial shading conditions for the three time windows of Figure 6

TW	F_{shaded}	$F_{unshaded}$	P_{Out_S}(W)	P_{Out_C}(W)
1	15%	85%	190.1	55.3
2	14%	86%	190.6	46.6
3	18%	82%	201.2	44.3

Figure 6.8 depicts the PV cell-groups output power, voltage and generated duty cycles for DC-DC micro converters for all ten groups in the three time windows, respectively. The chain of events in the simulation results of this case study is as follows:

At $t \in (0, 0.06)$s the SM-MPPT algorithm finds the best duty cycle for all ten groups. Results show duty cycles, output power, and converter output voltage are the same for the unshaded groups of cells with the same irradiation level.

At $t \in (0.06, 0.12)$s, the change in the shading pattern affects the irradiation level on four groups. SM-MPPT recognized the change in the operating point of four groups and found new MPPs for them. Also, it did not change the duty cycle for the unshaded groups.

At $t \in (0.12, 0.2)$s, the change in the shading pattern affects the irradiation level only on three groups and the duty cycle changed only for these groups.

Moreover, the shaded groups perform at their optimum power points and maximum power is harvested from all ten groups in all three different shading patterns. Because the converters are connected in series the converter output voltage is changed in case of a change in operating point to continue supplying the same output current.

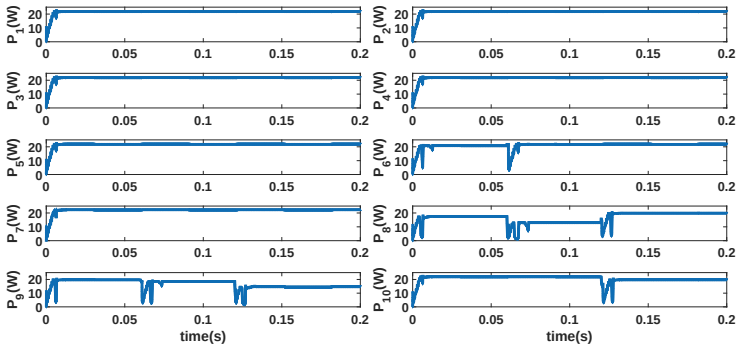

(a)

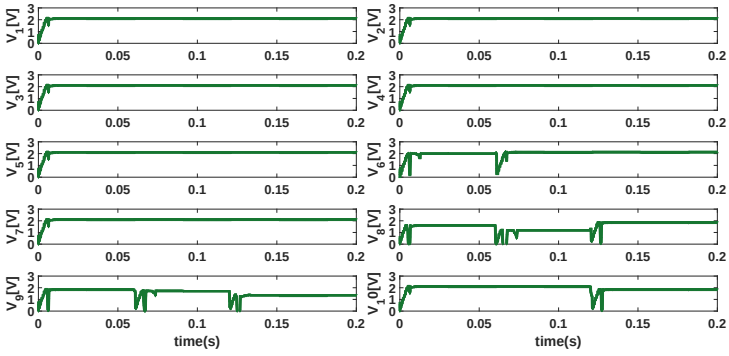

(b)

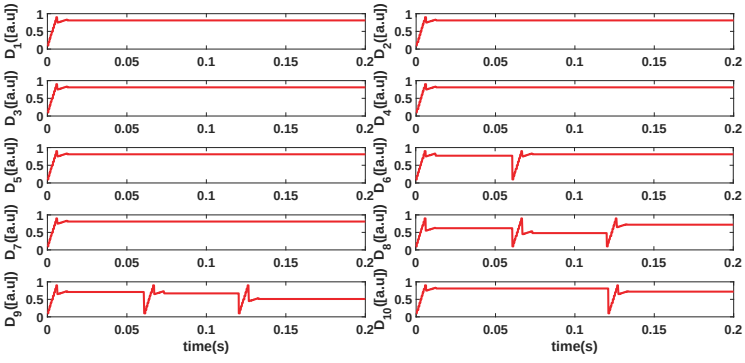

(c)

Figure 6.8 · Output from all ten group of cells.(a) Power, (b) Voltage, (c) Duty cycles

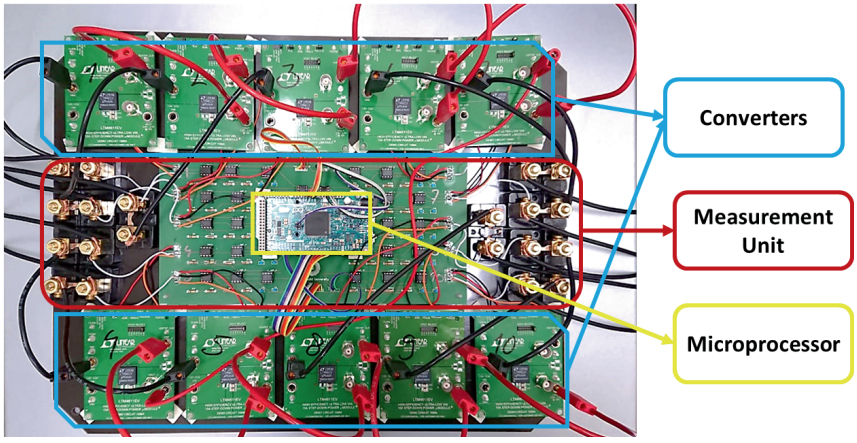

Figure 6.9 · Prototype board

6.4 Hardware

A photograph of the developed hardware is shown in Figure 6.9. The prototype board dimension is 20x30 cm, the prototype hardware consists of three different units:

i) The measurement unit: this part of the prototype is designed to measure the voltage and current of all ten groups of the PV module, the measured values are transferred to the microprocessor.

ii) The microprocessor: this unit is used to process the transferred data from the measurement unit, and to generate the reference signals to control all ten converters.

iii) Buck converter: each group of cells is equipped with a DC-DC buck converter, which is controlled with a control signal generated with the MPPT algorithm explained above.

In the following all above mentioned units will be discussed individually in different subsections.

The measurement unit

This unit consists of ten sub-units that measure data: each sub-unit measures output voltage and output current from one group of cells. Figure 6.10 illustrates the schematics of a sub-unit. A voltage divider with combination of $R_1 = 100k\Omega$ and $R_2 = 1k\Omega$ is used for sensing the voltage and a shunt resistor RSA-10-10 10A/100mV is implemented as the current sensor. Shunt resistors are much more

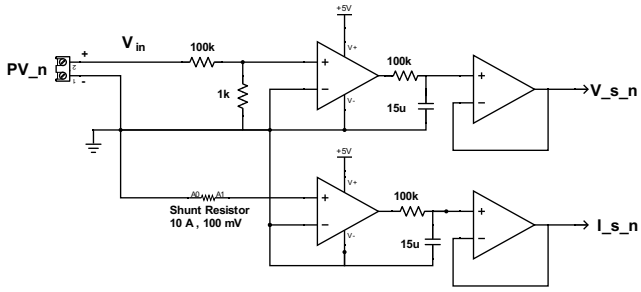

Figure 6.10 · Voltage, current sensor circuit

robust compared to a Hall effect current sensor and also generate much lower noise while sensing, which is the reason why an RSA is chosen for generating the current value signal.

Figure 6.10 depicts a two-level signal processing circuit where both sensed signals are first amplified and then noise is filtered out for preparation of the signal to the microprocessor. The Integrated Circuit (IC) AD626ANZ is a Single-Supply Differential Amplifier [193], and is implemented in each sub unit in the two-level circuit.

The microprocessor

A 32-bit Acorn RISC Machine (ARM) core microcontroller is used for data analysis and MPPT algorithm implementation for all groups. Inputs of the controller are voltage and current signals, and the main outputs are control signals for the DC-DC converters.

There are all together 20 signals to be read and processed in the microprocessor, but the aforementioned microcontroller has only 12 analog input pins. To mitigate this issue, one multiplexer (MUX CD74HC4051E [194]) is implemented per five signals in the circuit to read the signals from each group and write the respective signal to the microcontroller input gates. The MUX is controlled via a data selector signal which is generates in the ARM. Once the signal is sent, the ARM reads the signals, processes them and calibrates the exact value of voltage and current. Then, it implements the calibrated data in the SM-MPPT algorithm. Finally, converter control signals will be written to the assigned digital outputs. These control signals are generated for the converter control and will be discussed in the next subsection in greater detail.

Buck converter

As discussed in [184] for this study the LTM4611 is selected from the available DC-DC buck converters in the market. In this prototype a demo board for this converter is implemented. In this demo board, the converter could be controlled via its duty cycle, and the duty cycle itself is a function of a feedback resistor (FBR). Therefore, a digital potentiometer is implemented as an interface to control the duty cycle and as a result to control the converter outputs. In this study the MCP4161-502EP is used for this purpose, which is connected in series with a 20kΩ resistor could change the FBR in the range of [20, 25]kΩ, while the input signal of that could change from 0 to 255. This range for FBR is calculated from converter specifications where it could perform correctly regarding the range of its supplied voltage[161].

Practical test results and discussions

To investigate the feasibility of the smart module we tested the module under a partial shading condition at the PV lab at Utrecht University campus, and record data for about one hour. In Figure 6.11, the variation of shadings is roughly depicted in three TWs of $t_1 \in [0, 20]$ min, $t_2 \in [20, 40]$ min, and $t_3 \in [40, 60]$ min over the panel surface during the data logging. The maximum irradiation level measured on the panel surface within the one hour data logging duration is 350W/m^2, this value is measured with a pyranometer, which was located on the top of the module. It should be taken into consideration that Figure 6.11 shows only the starting point of the TWs, while the solid and pole shadows move during each TW to reach the next frame.

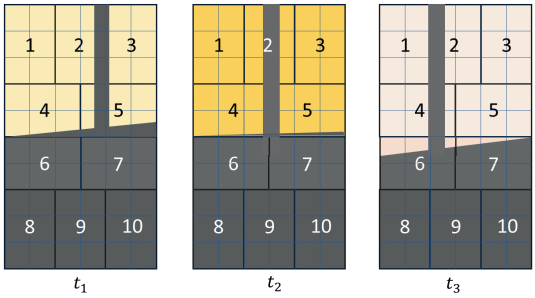

Figure 6.11 · Shades move in three time windows

In this figure only the pole and solid obstacles' shades are shown and shades from adjacent tree leaves which moved randomly and rapidly are not depicted. These particular causes of shades can be seen in Figure 12, where the panel at six

different shading conditions is depicted. The photos could give some idea about how the shadings move over the panel surface. The location of the panel is selected under a very random shading condition to investigate the performance of the smart panel under very random and fast changing conditions. Figure 6.13 shows output power from each group of cells in real time. Figure 6.14 and Figure 6.15 depict output for both voltage and current from each group of cells, respectively. These figures illustrate the effect of shading and the performance of the SM-MPPT algorithm. Output power shows how the MPPT algorithm extracts maximum power from each group of cell, output voltage illustrates how the duty cycle, as the control signal, controls the voltage and output current shows how the varying irradiation changes the output current. In following, regarding the aforementioned figures, performance of smart panel during each TW will be discussed in details.

The chain of events for this practical testing will be discussed in the following paragraphs. We will use the following three abbreviations to identify the type of shading that is affecting the module: (i) pole shade (PSh), (ii) solid obstacle shade (SOSh), (iii) tree leaves shades (TLSh).

At $t_1 \in [0, 20]$ min: In this time window nor group G_1 covered with PSh neither SOSh, but sometimes during this TW this group is covered with TLSh, for instance at t_1 between 8 and 11 min. Groups G_2, G_3 and G_5 are under PSh, however, group G_5 also is covered with SOSh, and also G_2 and G_3 are covered with TLSh randomly. G_4 is partially covered with SOSh and the rest of groups are covered completely with this shadow. G_4 and G_5 are rarely covered with TLSh in this TW.

Table 6.4 shows the average output power from each group of cells, from which G_4 extracted the maximum amount of power during this TW and its average power is $2.14W$. Other best groups are G_5 and G_1, with 1.87W and 1.27W output power. Figure 6.13 shows how the output power varies from the first moment till the end of this TW. For example, G_4 starts with very low output power and as a result of the movement of SOSh the output power from this group increased remarkably. The average output power from the whole module in this TW is 7.13W, however, for a conventional PV module the output power in this condition would be related to the output from the most shaded groups namely G_8, G_9, and G_{10} and would have been almost 1.75 W.

At $t_2 \in [20, 40]$ min: Groups G_1 and G_3 in this TW are only under coverage of TLSh. The PSh in this TW covers three groups: G_2, G_4, and G_5. This shade moves during this TW towards the left. The rest of the groups are under SOSh, however, this shade moves during this TW downward.

As tabulated in Table 6.4, G_5 extracted the maximum average power within

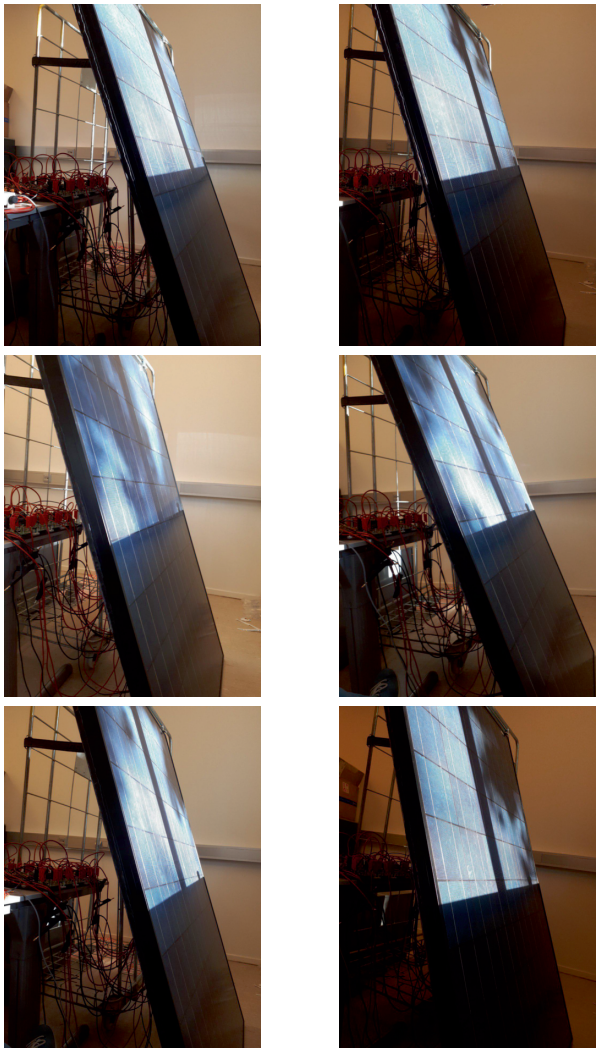

Fig. 12 : Smart panel under partial shading conditions

this period and that is because PSh relocated from this group during this period. The effect of PSh and TLSh is clearly shown on group G_4 with 60% decrease in its output power compared to the previous TW. G_1 and G_3 are second and third respect to maximum output power, as these groups are not covered with dark PSh and SOSh. The overall average output power from the smart module in this TW is 6.67W. Regarding the output power/current from groups under dark shades it is clear that total average output within this TW for a conventional panel would be almost 1.74 W.

At $t_3 \in [40, 60]$ min: Groups G_1, G_3 and G_5 in this TW are only under cover-

Table 6.4 · Average power in each TW from each group of cells

Group	TW	G_1	G_2	G_3	G_4	G_5
Average	t_1	1.2688	0.6373	0.3374	2.1413	1.8710
Power	t_2	1.2737	0.7849	1.0058	0.8542	1.6238
(W)	t_3	2.8691	1.7141	1.2301	1.3551	2.4370
Group	TW	G_6	G_7	G_8	G_9	G_{10}
Average	t_1	0.1958	0.1628	0.1701	0.2326	0.1307
Power	t_2	0.4452	0.4415	0.1770	0.2526	0.1172
(W)	t_3	0.3611	0.3528	0.1432	0.1908	0.0968

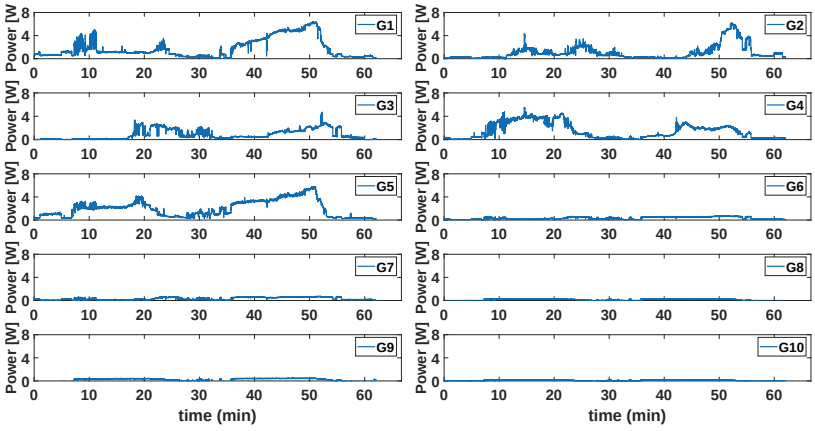

Figure 6.13 · Output Power from the smart panel

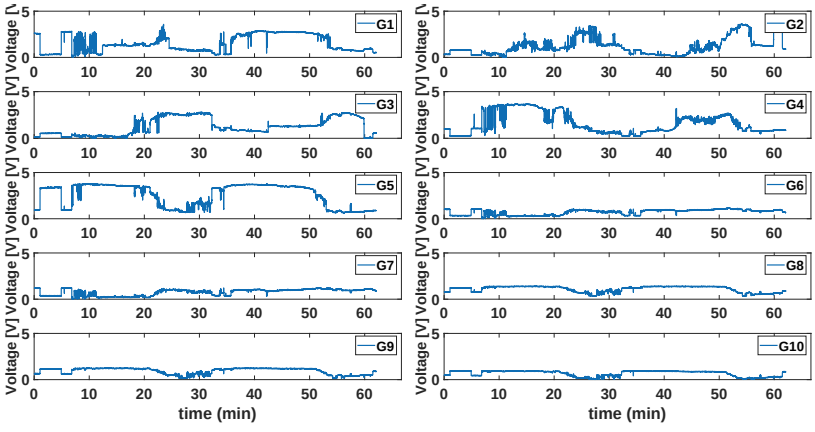

Figure 6.14 · Output Voltage from the smart panel

age of TLSh. Groups $G_i, i \in (2, 4, 6)$ are covered partially with PSh in this TW. Group G_7 at the begin of this TW comes out partially from the SOSh. The rest

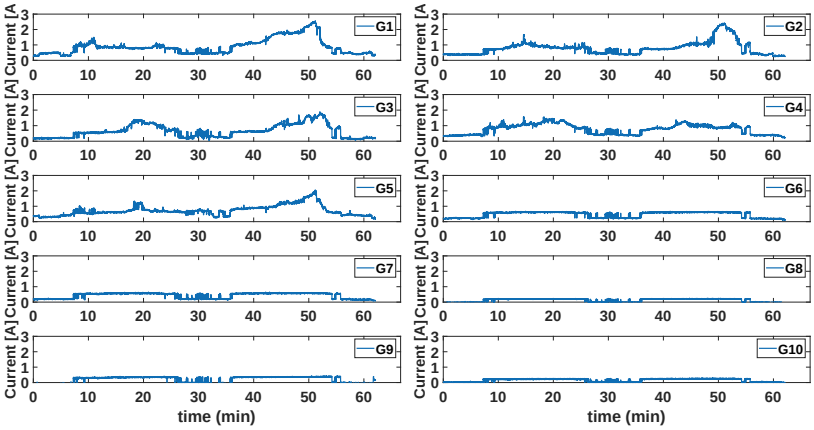

Figure 6.15 · Output Current from the smart panel

of the groups are under dark SOSh, and similar to the previous TW, this shade moves during this TW downward and PSh moves to the left.

Shown in Table 6.4 maximum average extracted power is from group G_1 and followed by group G_5. These two groups are only covered with TLSh, it is clearly shown in Figure 12 and also tabulated in Table 6.4 that group G_3 is covered with lots of TLSh and that is due to the change in sun tilt angle which changes the TLSh patterns. Comparing groups G_1 and G_2 in Figure 6.13 shows that once the PSh moves to the left the output power from G_2 increases a lot, but output power from group G_1 decreases, which is the effect of PSh. Average output power for the whole smart panel within the last TW is 11.1W. The overall average increased 167% compare to the previous TW. Conventional panel in this TW extracts 1.38 W.

Figure 6.16 shows the output power from different groups in the smart module. This figure depicts how the shading could affect the output power from group of cells with similar characteristics and different shading patterns. $G_6 - G_{10}$ are mainly under SOSh and that is the reason for their very low output power. This figure shows G_2 and G_3 have experience of being under very dynamic TLSh.

Table 6.5 tabulates a very brief conclusion on how two typologies of smart and conventional panels performed under PSC for both simulation and hardware experiment.

From the results presented here, we can state that the average output power in the smart module is higher than the expected average power from a conventional module with three BPDs. Regarding these values the smart module extracted on average 8.31W in a very restricted shading condition with three different shade

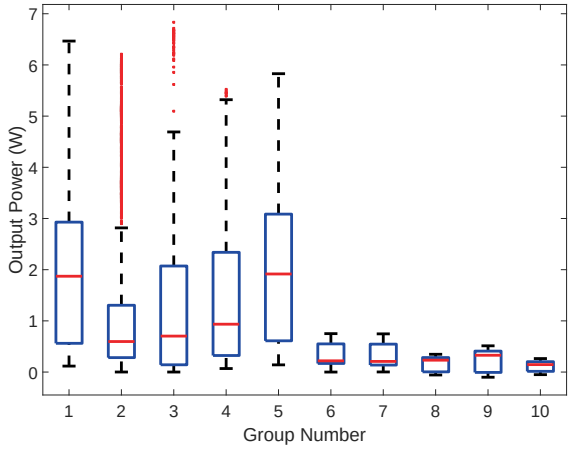

Figure 6.16 · Output power from groups

Table 6.5 · Average output power from both simulation and hardware experiment

Panel	Power (W)		Ratio (%)	
	Simulation	Prototype	Simulation	Prototype
Smart Panel	193.96	8.31	398%	508%
Conventional Panel	48.73	1.63		

* ambient condition is different in simulation and prototype testing

types and also maximum irradiation of 350W/m^2. However, considering the outputs from groups with most shaded condition a conventional panel in this testing condition could generate only about 1.63W. It can be concluded that both in simulation and prototype testing condition, smart module performed much better compared to the conventional panel. Tabulated in Table 6.5 smart module performed almost 508% better than conventional module with BPDs.

6.5 Conclusion

In this chapter, a smart module using a micro buck converter is proposed. The module is designed such that even at low irradiation due to shading optimal power is generated. A sample-based MPPT algorithm with two functions is introduced in this chapter. To investigate the functionality of the design, the MATLAB-SIMULINK environment is used. Simulation tests showed the smart panel could follow fast changes (<0.2s) in shading patterns very well.

As a proof of concept a hardware prototype for this module has been built. This prototype is tested under partial shading conditions with three different shade types. Testing has been done for this module for about one hour, and the logged

data is used for analysis in this work. The outcomes from hardware testing showed that the smart module is functioning well and that it could extract about 5.1 times more power compared to a conventional module with three BPDs in the aforementioned testing conditions. Future work will include longer outdoor tests to assess the benefits at longer timescales.

6.6 Acknowledgments

The authors gratefully acknowledge fruitful discussions with Rudi Jonkman and Robert van der Sanden (Heliox), Lenneke Sloof (ECN). This work is partly financially supported by the Netherlands Enterprise Agency (RVO) within the framework of the Dutch Topsector Energy (project Scalable Shade Tolerant Modules, SSTM).

7

Synthesis and conclusions

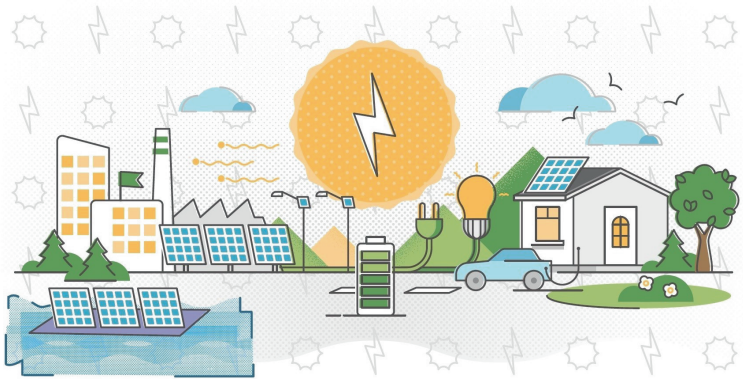

7.1 Research Context

In 2015, the Paris agreement was introduced with the main objective of limiting global temperature increase to 2 °C by 2100 and pursuing efforts to limit the increase to 1.5 °C. Major decarbonisation technologies which focus on the reduction of CO_2 emissions related to the supply and demand sides of energy are solar and wind energy [195, 1]. Sustained growth of wind and solar to multi-TW levels is required by mid-century to support a zero-emission society. As wind has been moving offshore, recently also floating photovoltaics are starting to be deployed offshore. Given the large amount of offshore surfaces, also being relatively close to human settlements, offshore floating photovoltaics offer a huge potential source of renewable energy. For this reason, this thesis has focused on the exploration of performance and system integration aspects of offshore floating photovoltaics systems, using simulation tools combined with development and testing of smart shade resilient module designs. This chapter will summarize the main results and will put them into context.

7.2 Answers to the research questions

The main research question in this thesis has been broken down into three smaller research questions to address weather effects on performance of offshore FPV systems, cable pooling for a hybrid solar-wind power system and also the mitigation of partial shading effects. In this section, first the three questions will be answered, followed by answering the main research question.

Question 1

How do weather conditions affect the performance of an offshore FPV system on open water, in particular, which parameters are of most importance?

In Chapter 2, a mathematical model for both land and sea based PV systems has been developed in order to compare both systems. To perform the analysis for this question, both actual irradiation and temperature data is used as input in the mathematical model. A floating PV system is characterized by constantly varying tilt and orientation angles, in contrast to a land-based system, which complicates energy yield modeling. A model has been developed that allows the calculation of the tilt angle variation based on wave characteristics and how these are influenced by wind speed leading to a wave spectrum analysis. Moreover, for calculating the temperature of the PV systems both heat transfer theory and an apparent temper-

ature method are implemented to estimate an accurate equilibrium temperature, where the effects of wind speed, relative humidity and presence of water are taken into account.

Our simulations show that the energy yield of both systems differs predominantly as a result of lower module temperatures, while the effects of varying tilt are minimal. We found that the system at sea shows 12.96% higher performance on average on an annual basis compared to the land based system. Seasonal effects can be discerned though: in some months a relative output energy increase of up to 18% is calculated.

Another environmental parameter, ocean surface albedo, is discussed in detail in Chapter 3. First a mathematical model for sea surface albedo is presented. It should be noted that the contribution of the ocean interior reflection to surface albedo is neglected in this model. The modeled albedo is implemented in a fully mathematical model of an offshore floating PV system considering variable tilt due to the wave spectrum, and wind speed. The results showed that albedo does not have a simple linear relation with wind speed. The effect of solar zenith angle is quite clear in these results. If the wind is strong enough to form whitecaps on the sea surface the albedo starts increasing and sea surface roughness is not dominant anymore.

Comparing the floating PV system implementing constant and modeled albedo shows that compared to a fixed value for ocean surface albedo, the PV system performance is larger by about 3.04% on average, without clear seasonal differences. This shows that dynamic albedo should be used in performance evaluations of floating PV systems.

Question 2

How can an offshore FPV system on the North Sea be used by employing cable pooling within an existing offshore wind farm?

The combination of an offshore solar PV system and a wind farm can be beneficial in technical and economical terms. At times with sub-optimal power generation by wind turbines the cable that transports electricity to the coast is not optimally used. Chapter 4 discusses the effects of adding PV capacity to increase cable usage, which is known as cable pooling. We have calculated optimal wind and solar combined capacity given meteorological conditions in the North Sea, showing that curtailment of solar is quite limited: adding a 700 MWp PV system to the existing 752 MW wind farm leads to an increase of about 30% in combined energy yield, with a curtailment ratio of about 4%.

The economical analysis further showed that the profitability of integrating

floating PV within offshore wind farms depends on two major factors: the marginal power delivered to the grid by floating PV and the costs of the solar system. Improving the marginal solar power delivered to the grid and decreasing the total costs for the offshore FPV system would result in larger total benefits. We have also shown that subsidy is needed at present to support offshore FPV deployment.

Finally, our case study is further generalized realizing that meteorological conditions, in particular the anti-correlation of the wind and solar resource is determining, next to cost, the optimum wind-solar combination.

Sub-question 3

How can potential partial shading conditions be addressed in a generic way and how should a smart shade resilient module be designed?

To mitigate partial shading effects on the performance of PV modules, a generic model is developed that is able to evaluate smart PV module architectures. In Chapter 5 the proposed architecture consisted of a number of PV cell groups, and a DC-DC buck converter for a group of PV cells is implemented to amplify the current of shaded groups. This converter was chosen after investigation of characteristics of appropriate micro-converters in the market with respect to the PV cell specifications. This resulted in the choice for the Linear Technology LTM4611 converter. The LS-SVM (Least Square Support Vector Machine) method was used (i) to generalize the behavior of the converter efficiency, and (ii) to optimize the group size of PV cells. In summary, the optimum grouping for the designed specifications was 10 groups of 6 cells.

After the smart module was designed, the effect of shading patterns was studied. A model for shading patterns was developed with two types of random and pole shadows based on actual measured irradiation data. Simulations demonstrated that the average amount of generated energy of the smart architecture was almost 79.5% of the energy generated by an ideal PV module. Compared with series connected and parallel connected architectures, the smart PV module showed 47% and 13.4% better performance, respectively. Moreover, the smart module economic payback time compared with the most commonly-used architecture in the market is expected to be shorter.

In Chapter 6, a smart module using a micro buck converter is further developed. The module is designed such that even at low irradiation due to shading optimal power is generated. A sample-based MPPT algorithm with two functions is introduced. To investigate the functionality of the design, the MATLAB-SIMULINK environment is used.

Simulation tests showed the smart panel could follow fast changes (<0.2s) in shading patterns very well. As a proof of concept a hardware prototype for this module has been built. This prototype is tested under partial shading conditions with three different shade types. Testing has been done for this module for about one hour, and the logged data is used for analysis in this work. The outcomes from hardware testing showed that the smart module is functioning well and that it could extract about 5.1 times more power compared to a conventional module with three BPDs in the aforementioned testing conditions. Future work will include longer outdoor tests to assess the benefits at longer timescales.

Main research question

How beneficial would an offshore FPV system installed on the North Sea be?

Based on the answers above, we can conclude that in terms of performance, a a considerable advantage of about 13% can be expected for deployment of offshore FPV. Moreover, economic advantages also exist in seeking the combination with existing (or planned) offshore wind farms. Although we note that at present subsidies are still needed for the FPV system, when assuming large-scale deployment, subsidies will not be needed in the future, similar to what has happened in offshore wind park developments.

A smart shade resilient PV module has been designed, based on existing components. Manufacturing and testing was successful, and these modules may be applied in the built environment. Given the design, integration of electronics should be possible especially in back contact cell module designs, in which the back plate connects all cells, forming one large electronic circuit. A similar idea is introduced in [196], where an interconnection design is developed for c-Si PV modules to increase the reliability, power and energy yield of PV modules under different partial shading conditions.

With the combination of an FPV system in an offshore wind park, dynamic shading from rotors will affect the performance of the FPV system. Thus, a shade resilient module system should be deployed.

7.3 Recommendations for future research

While this research shows that floating PV systems at the North Sea can be beneficial, it remains to be seen if deployment would be beneficial at other locations. At present, only a limited amount of studies exist, but they all show benefits in

terms of higher energy yields, e.g., in Singapore [46]. However, it is essential for widespread deployment of FPV systems to perform a generic study on a global scale to identify potential locations for floating PV systems. It should be noted that each open water has its own characteristics and may behave in a different manner.

In Chapter 2 a precise mathematical model is introduced. However, there are some variables which may have to be optimized to increase the accuracy of the model. For instance the effect of salinity in the system was neglected. We assumed this to be valid as a special coating may be present on the modules which would prevent effects of salinity, thus avoiding mismatch conditions which may lead to hot spots. This was inspired by existing research on anti-soiling coatings. One important issue could be the design and the effect of a preventive coating, e.g., if a new coating might cause a mismatch or the coating thickness may lead to decreasing the efficiency of the module.

In Chapter 3, the chemical characteristics of open water are neglected in the study of the dynamic albedo effect, also the formation of the fog at the ocean water level has not been taken into account. It is highly recommended for interested researchers to model the system considering these characteristics as well, as it should increase the accuracy of the results.

In Chapters 5 and 6 a smart module is introduced. To continue this part of research, it is strongly recommended to investigate thermal effects, focusing on hot spots under partial shading conditions. To find the optimal locations for the required electronics on the back sheet, application of an optimization method is essential. Adding the electronics circuitry should be done in such a way that intra-module and cell temperature is evenly distributed over the panel, otherwise hot spots or other mismatch conditions might occur, which could lead to decreased performance or even increased chances of malfunctioning. Considering the smart module design, the two following metrics can be addressed for future researches: (i) the energy return of energy investment (ERoEI), (ii) the lifetime assessments.

7.4 Epilogue

Following scientific consensus, full decarbonisation of our global energy system is the only way to achieve climate stabilisation. One big step in this transition is to exchange the source of energy from fossil fuel to renewable energy. Solar energy is a very well-known type of renewable energy, and its deployment keeps increasing during the last decade. Floating solar, however, is a relatively recent type of PV system. It has its own pros and cons, thus, especially considering its recent introduction, it needs more study to make all aspects of this field clear.

In this thesis, a comprehensive effort was made to show the benefits of a FPV system on the North Sea. All models and simulations presented here are only the tip of the iceberg in this field, and we hope this part of research will be helpful for other researchers in similar fields of study.

Bibliography

[1] International Energy Agency. *World Energy Outlook 2020*. International Energy Agency, Paris, France, 2020.

[2] The International Energy Agency (IEA). Snapshot of global pv markets 2020.

[3] IEA World Energy Statistics and Balances. Technical report, International Energy Agency.

[4] Atse Louwen, Wilfried G. J. H. M. van Sark, André P. C. Faaij, and Ruud E. I. Schropp. Re-assessment of net energy production and greenhouse gas emissions avoidance after 40 years of photovoltaics development. *Nature Communications*, 7:13728, 2016.

[5] Luis Hernández-Callejo, Sara Gallardo-Saavedra, and Víctor Alonso-Gómez. A review of photovoltaic systems: Design, operation and maintenance. *Solar Energy*, 188:426 – 440, 2019.

[6] Adrian Whiteman, Sonia Rueda, Dennis Akande, Nazik Elhassan, Gerardo Escamilla, and Iana Arkhipova. *Renewable Capacity Statistics 2020*. IRENA, 2020.

[7] Piyush Choudhary and Rakesh Kumar Srivastava. Sustainability perspectives- a review for solar photovoltaic trends and growth opportunities. *Journal of Cleaner Production*, 227:589 – 612, 2019.

[8] Arnulf Jäger-Waldau. Snapshot of photovoltaics—february 2020. *Energies*, 13(930), 2020.

[9] Improvement of Shade Resilience in Photovoltaic Modules Using Buck Converters in a Smart Module Architecture. *Energies*, 11(1):250, jan 2018.

[10] Joya Zeitouny, Noémie Lalau, Jeffrey M. Gordon, Eugene A. Katz, Gilles Flamant, Alain Dollet, and Alexis Vossier. Assessing high-temperature photovoltaic performance for solar hybrid power plants. *Solar Energy Materials and Solar Cells*, 182:61 – 67, 2018.

[11] U.S. Energy Information Administration. Net consumption of electricity worldwide from 1980 to 2017.

[12] Daryl M Chapin, CS Fuller, and GL Pearson. A new silicon p-n junction photocell for converting solar radiation into electrical power. *Journal of Applied Physics*, 25(5):676–677, 1954.

[13] Martin A Green, Ewan D Dunlop, Jochen Hohl-Ebinger, Masahiro Yoshita, Nikos Kopidakis, and Xiaojing Hao. Solar cell efficiency tables (version 56). *Progress in Photovoltaics: Research and Applications*, 28(7):629–638, 2020.

[14] B Tuncel, T Ozden, RS Balog, and BG Akinoglu. Dynamic thermal modelling of pv performance and effect of heat capacity on the module temperature. *Case Studies in Thermal Engineering*, 22:100754, 2020.

[15] Manju Santhakumari and Netramani Sagar. A review of the environmental factors degrading the performance of silicon wafer-based photovoltaic modules: Failure detection methods and essential mitigation techniques. *Renewable and Sustainable Energy Reviews*, 110:83 – 100, 2019.

[16] H. Patel and V. Agarwal. Matlab-based modeling to study the effects of partial shading on pv array characteristics. *IEEE Transactions on Energy Conversion*, 23(1):302–310, 2008.

[17] S. Mirbagheri Golroodbari, Arjen. de Waal, and Wilfried van Sark. Improvement of Shade Resilience in Photovoltaic Modules Using Buck Converters in a Smart Module Architecture. *Energies*, 11(1):250, jan 2018.

[18] Panagiotis Moraitis, Bala Bhavya Kausika, Nick Nortier, and Wilfried van Sark. Urban environment and solar pv performance: The case of the netherlands. *Energies*, 11(6), 2018.

[19] Mehmet Emin Meral and Furkan Dincer. A review of the factors affecting operation and efficiency of photovoltaic based electricity generation systems. *Renewable and Sustainable Energy Reviews*, 15(5):2176–2184, 2011.

[20] Nils H Reich, Bjoern Mueller, Alfons Armbruster, Wilfried GJHM Van Sark, Klaus Kiefer, and Christian Reise. Performance ratio revisited: is PR 90% realistic? *Progress in Photovoltaics: Research and Applications*, 20(6):717–726, 2012.

[21] Thomas Huld and Ana M. Gracia Amillo. Estimating pv module performance over large geographical regions: The role of irradiance, air temperature, wind speed and solar spectrum. *Energies*, 8(6):5159–5181, 2015.

[22] Hussein A Kazem, Miqdam T Chaichan, Iman Mohammed Al-Shezawi, Hanan Saif Al-Saidi, Hanan Sulaiman Al-Rubkhi, Khamis Al-sinani, and Ali HA Al-Waeli. Effect of humidity on the pv performance in oman. 2012.

[23] Esmail M Saber, Siew Eang Lee, Sumanth Manthapuri, Wang Yi, and Chirag Deb. Pv (photovoltaics) performance evaluation and simulation-based energy yield prediction for tropical buildings. *Energy*, 71:588–595, 2014.

[24] Bashar Hammad, Mohammad Al-Abed, Ahmed Al-Ghandoor, Ali Al-Sardeah, and Adnan Al-Bashir. Modeling and analysis of dust and temperature effects on photovoltaic systems' performance and optimal cleaning frequency: Jordan case study. *Renewable and Sustainable Energy Reviews*, 82:2218–2234, 2018.

[25] Daisuke Sato and Noboru Yamada. Review of photovoltaic module cooling methods and performance evaluation of the radiative cooling method. *Renewable and Sustainable Energy Reviews*, 104:151 – 166, 2019.

[26] EPJA Skoplaki and John A Palyvos. Operating temperature of photovoltaic modules: A survey of pertinent correlations. *Renewable energy*, 34(1):23–29, 2009.

[27] M Bardhi, G Grandi, and GM Tina. Comparison of pv cell temperature estimation by different thermal power exchange calculation methods. In *Proceedings of the International Conference on Renewable Energies and Power Quality (ICREPQ'12), Santiago de Compostela, Spain*, pages 28–30, 2012.

[28] Jean-Michel SERVANT. Calculation of the cell temperature for photovoltaic modules from climatic data. In E. BILGEN and K.G.T. HOLLANDS, editors, *Intersol Eighty Five*, pages 1640 – 1643. Pergamon, Oxford, 1986.

[29] Shrey Verma, Subhashree Mohapatra, Subhankar Chowdhury, and Gaurav Dwivedi. Cooling techniques of the pv module: A review. *Materials Today: Proceedings*, 2020.

[30] A Pfreundt, D Yucebas, AJ Beinert, et al. Post-processing thickness variation of pv module materials and its impact on temperature, mechanical stress and power. *Proceedings of the 36th EU PVSEC*, pages 935–940, 2019.

[31] John A Duffie, William A Beckman, and Nathan Blair. *Solar engineering of thermal processes, photovoltaics and wind*. John Wiley & Sons, 2020.

[32] Rodolphe Vaillon, Olivier Dupré, Raúl Bayoán Cal, and Marc Calaf. Pathways for mitigating thermal losses in solar photovoltaics. *Scientific reports*, 8(1):1–9, 2018.

[33] S Zahra Mirbagheri, Saad Mekhilef, and S Mohsen Mirhassani. MPPT with Inc. Cond method using conventional interleaved boost converter. *Energy Procedia*, 42:24–32, 2013.

[34] Ali Bidram, Ali Davoudi, and Robert S. Balog. Control and Circuit Techniques to Mitigate Partial Shading Effects in Photovoltaic Arrays. *IEEE Journal of Photovoltaics*, 2(4):532–546, oct 2012.

[35] E. Karatepe, Syafaruddin, and T. Hiyama. Simple and high-efficiency photovoltaic system under non-uniform operating conditions. *IET Renewable Power Generation*, 4(4):354, 2010.

[36] Boudewijn B. Pannebakker, Arjen C. de Waal, and Wilfried G.J.H.M. van Sark. Photovoltaics in the shade: one bypass diode per solar cell revisited. *Progress in Photovoltaics: Research and Applications*, 25(10):836–849, oct 2017.

[37] C. Olalla, D. Clement, M. Rodriguez, and D. Maksimovic. Architectures and Control of Submodule Integrated DC-DC Converters for Photovoltaic Applications. *IEEE Transactions on Power Electronics*, 28(6):2980–2997, jun 2013.

[38] S.Z. Mirbagheri, M. Aldeen, and S. Saha. A comparative study of MPPT algorithms for standalone PV systems under RCIC. In *Asia-Pacific Power and Energy Engineering Conference, APPEEC*, volume 2016-Janua, 2016.

[39] Marco Rosa-Clot and Giuseppe Marco Tina. *Submerged and Floating Photovoltaic Systems: Modelling, Design and Case Studies*. Academic Press, 2017.

[40] T Reindl, C Paton, A Kumar, H Liu, VA Krishnamurthy, J Zhang, S Tay, Y Zhan, Z Dobrotkova, S Chavez, et al. Where sun meets water-floating solar market report, 2019.

[41] Kim Trapani and Miguel Redón Santafé. A review of floating photovoltaic installations: 2007–2013. *Progress in Photovoltaics: Research and Applications*, 23(4):524–532, 2015.

[42] Alok Sahu, Neha Yadav, and K. Sudhakar. Floating photovoltaic power plant: A review. *Renewable and Sustainable Energy Reviews*, 66:815 – 824, 2016.

[43] Bp statistical review of world energy, London, 2017.

[44] M Grech, L Stagno, M Aquilina, M Cadamuro, and U Witzke. Floating photovolataic installations in maltese sea waters. In *32nd European Photovoltaic Solar Energy Conference and Exhibition*, volume 1968, page 5, 2016.

[45] S. Zahra M Golroodbari, D F Vaartjes, J B L Meit, A P Van Hoeken, M Eberveld, H. Jonker, and Wilfried G J H M Van Sark. Pooling the cable: a techno-economic feasibility study of integrating offshore floating photovoltaic solar technology within an offshore wind park. *Solar Energy*, (in press):xx–xx, 2021.

[46] Haohui Liu, Vijay Krishna, Jason Lun Leung, Thomas Reindl, and Lu Zhao. Field experience and performance analysis of floating pv technologies in the tropics. *Progress in Photovoltaics: Research and Applications*, 26(12):957–967, 2018.

[47] Shahriar Ahmed, Md Nur Alam Mondal, Md Nadim Mahmud, and Md Khairum Bashar Bhuiyan. Prospects and utilization of solar energy in bangladesh.

[48] China Daily.

[49] Yuan-Hsiou Chang, Chen-Ruei Ku, and Naichia Yeh. Solar powered artificial floating island for landscape ecology and water quality improvement. *Ecological engineering*, 69:8–16, 2014.

[50] Naichia Yeh, Pulin Yeh, and Yuan-Hsiou Chang. Artificial floating islands for environmental improvement. *Renewable and Sustainable Energy Reviews*, 47:616 – 622, 2015.

[51] Pietro Elia Campana, Louise Wästhage, Worrada Nookuea, Yuting Tan, and Jinyue Yan. Optimization and assessment of floating and floating-tracking pv systems integrated in on-and off-grid hybrid energy systems. *solar energy*, 177:782–795, 2019.

[52] Miguel Redón Santafé, Juan Bautista Torregrosa Soler, Francisco Javier Sánchez Romero, Pablo S Ferrer Gisbert, José Javier Ferrán Gozálvez, and Carlos M Ferrer Gisbert. Theoretical and experimental analysis of a

floating photovoltaic cover for water irrigation reservoirs. *Energy*, 67:246–255, 2014.

[53] Young-Kwan Choi, Nam-Hyung Lee, and Kern-Joong Kim. Empirical research on the efficiency of floating pv systems compared with overland pv systems. In *Proceedings, The 3rd International Conference on Circuits, Control, Communication, Electricity, Electronics, Energy, System, Signal and Simulation*, volume 25, pages 284–289, 2013.

[54] S Zahra Golroodbari and Wilfried van Sark. Simulation of performance differences between offshore and land-based photovoltaic systems. *Progress in Photovoltaics: Research and Applications*, 2020.

[55] Saad Mekhilef, Rahman Saidur, and Masoud Kamalisarvestani. Effect of dust, humidity and air velocity on efficiency of photovoltaic cells. *Renewable and sustainable energy reviews*, 16(5):2920–2925, 2012.

[56] Jan Maurice Bödeker, Marc Bauer, Martin Pehnt, et al. Aluminium and renewable energy systems–prospects for the sustainable generation of electricity and heat. *Institut für Energie und Umweltforschung Heidelberg GmbH: Heidelberg, Germany*, 2010.

[57] Shiva Gorjian, H Sharon, Hossein Ebadi, Karunesh Kant, Fausto Bontempo Scavo, and Giuseppe Marco Tina. Recent technical advancements, economics and environmental impacts of floating photovoltaic solar energy conversion systems. *Journal of Cleaner Production*, page 124285, 2020.

[58] Young-Kwan Choi, Nam-Hyung Lee, An-Kyu Lee, and Kern-Joong Kim. A study on major design elements of tracking-type floating photovoltaic systems. *International Journal of Smart Grid and Clean Energy*, 3(1):70–74, 2014.

[59] R. Cazzaniga, M. Cicu, M. Rosa-Clot, P. Rosa-Clot, G.M. Tina, and C. Ventura. Floating photovoltaic plants: Performance analysis and design solutions. *Renewable and Sustainable Energy Reviews*, 81:1730 – 1741, 2018.

[60] HI Kim, NH Lee, EC Lee, DG Kim, ST Hong, HH Lee, JS Yi, and SH Lee. Groundwork research for commercialization of floated photovoltaic system. *K-water research report*, 2012.

[61] R Cazzaniga, M Cicu, M Rosa-Clot, P Rosa-Clot, GM Tina, and C Ventura. Compressed air energy storage integrated with floating photovoltaic plant. *Journal of Energy Storage*, 13:48–57, 2017.

[62] Paritosh Sharma, Bharat Muni, and Debojyoti Sen. Design parameters of 10 kw floating solar power plant. In *Proceedings of the International Advanced Research Journal in Science, Engineering and Technology (IARJSET), National Conference on Renewable Energy and Environment (NCREE-2015), Ghaziabad, India*, volume 2, 2015.

[63] R. Cazzaniga, M. Rosa-Clot, P. Rosa-Clot, and G. M. Tina. Floating tracking cooling concentrating (ftcc) systems. In *2012 38th IEEE Photovoltaic Specialists Conference*, pages 000514–000519, June 2012.

[64] Kim Trapani. *Flexible floating thin film photovoltaic (PV) array concept for marine and lacustrine environments*. PhD thesis, Laurentian University of Sudbury, 2014.

[65] Kim Trapani, Dean L Millar, and Helen CM Smith. Novel offshore application of photovoltaics in comparison to conventional marine renewable energy technologies. *Renewable Energy*, 50:879–888, 2013.

[66] Christian Bussar, Philipp Stöcker, Zhuang Cai, Luiz Moraes Jr, Dirk Magnor, Pablo Wiernes, Niklas van Bracht, Albert Moser, and Dirk Uwe Sauer. Large-scale integration of renewable energies and impact on storage demand in a european renewable power system of 2050—sensitivity study. *Journal of Energy Storage*, 6:1–10, 2016.

[67] Giampaolo Manfrida and Riccardo Secchi. Seawater pumping as an electricity storage solution for photovoltaic energy systems. *Energy*, 69:470–484, 2014.

[68] Javier Farfan and Christian Breyer. Combining floating solar photovoltaic power plants and hydropower reservoirs: a virtual battery of great global potential. *Energy Procedia*, 155:403–411, 2018.

[69] Luis E Teixeira, Johan Caux, Alexandre Beluco, Ivo Bertoldo, José Antônio S Louzada, Ricardo C Eifler, et al. Feasibility study of a hydro pv hybrid system operating at a dam for water supply in southern brazil. *Journal of Power and Energy Engineering*, 3(09):70, 2015.

[70] M Dolores Esteban, J Javier Diez, Jose S López, and Vicente Negro. Why offshore wind energy? *Renewable Energy*, 36(2):444–450, 2011.

[71] Mario López, Noel Rodríguez, and Gregorio Iglesias. Combined floating offshore wind and solar pv. *Journal of Marine Science and Engineering*, 8(8):576, 2020.

[72] The intra-annual variability in the performance of wave energy converters: A comparative study in n galicia (spain). *Energy*, 82:138 – 146, 2015.

[73] Arnulf Jäger-Waldau. Snapshot of photovoltaics—february 2019. *Energies*, 12(769), 2019.

[74] Christian Breyer, Dmitrii Bogdanov, Arman Aghahosseini, Ashish Gulagi, Michael Child, Ayobami Solomon Oyewo, Javier Farfan, Kristina Sadovskaia, and Pasi Vainikka. Solar photovoltaics demand for the global energy transition in the power sector. *Progress in Photovoltaics: Research and Applications*, 26(8):505–523, 2018.

[75] O. Dupré, R. Vaillon, and M.A. Green. *Thermal Behavior of Photovoltaic Devices – Physics and Engineering*. Springer International Publishing, 2017.

[76] Zhiwen Wang, Rupp Carriveau, David S.-K. Ting, Wei Xiong, and Zuwen Wang. A review of marine renewable energy storage. *International Journal of Energy Research*, 0(0):in press, 2019.

[77] Tore Irgens Kuhnle. All subsea creating value from subsea processing. *DNVGL STRATEGIC RESEARCH and INNOVATION POSITION PAPER*, pages 1–72, 2015.

[78] Adam M. Pringle, R.M. Handler, and J.M. Pearce. Aquavoltaics: Synergies for dual use of water area for solar photovoltaic electricity generation and aquaculture. *Renewable and Sustainable Energy Reviews*, 80:572 – 584, 2017.

[79] Marco Rosa-Clot and Giuseppe Marco Tina. Chapter 5 - the floating pv plant. In Marco Rosa-Clot and Giuseppe Marco Tina, editors, *Submerged and Floating Photovoltaic Systems*, pages 89 – 136. Academic Press, 2018.

[80] Young-Kwan Choi. A study on power generation analysis of floating pv system considering environmental impact. *International Journal of Software Engineering and its Applications*, 8:75–84, 2014.

[81] Marco Rosa-Clot and Giuseppe Marco Tina. Chapter 4 - submerged pv systems. In Marco Rosa-Clot and Giuseppe Marco Tina, editors, *Submerged and Floating Photovoltaic Systems*, pages 65 – 87. Academic Press, 2018.

[82] N. Martín and J. M. Ruiz. Annual angular reflection losses in pv modules. *Progress in Photovoltaics: Research and Applications*, 13(1):75–84, 2005.

[83] Thomas M Klucher. Evaluation of models to predict insolation on tilted surfaces. *Solar energy*, 23(2):111–114, 1979.

[84] Marko Gulin, Mario Vašak, and Mato Baotic. Estimation of the global solar irradiance on tilted surfaces. In *17th International Conference on Electrical Drives and Power Electronics (EDPE 2013)*, volume 6, pages 347–353, 2013.

[85] American national snow and ice data (nsid), https://nsidc.org.

[86] Annette Muetze and JG Vining. Ocean wave energy conversion-a survey. In *Industry Applications Conference, 2006. 41st IAS Annual Meeting. Conference Record of the 2006 IEEE*, volume 3, pages 1410–1417. IEEE, 2006.

[87] K Hasselmann, D B Ross, P Müller, and W Sell. A parametric wave prediction model. *Journal of Physical Oceanography*, 6:200–228, Mar 1976.

[88] Yang Yu, Hailong Pei, and Chengzhong Xu. Parameter identification of jonswap spectrum acquired by airborne lidar. *Journal of Ocean University of China*, 16(6):998–1002, Dec 2017.

[89] Gunnar Steinn Asgeirsson. Hydrodynamic investigation of wavepower buoys. Master's thesis, KTH, Naval Systems, 2013.

[90] Stephanie J. Jacobs, Alexandre B. Pezza, Vaughan Barras, John Bye, and Timo Vihma. An analysis of the meteorological variables leading to apparent temperature in australia: Present climate, trends, and global warming simulations. *Global and Planetary Change*, 107:145 – 156, 2013.

[91] R.G. Steadman. Norms of apparent temperature in australia. *Australian Meteorological Magazine*, 43(1):1–16, 1994. cited By 81.

[92] Mark G. Lawrence. The relationship between relative humidity and the dewpoint temperature in moist air: A simple conversion and applications. *Bulletin of the American Meteorological Society*, 86(2):225–234, 2005.

[93] WGJHM Van Sark, Atse Louwen, Arjen C de Waal, and REI Schropp. Upot: The utrecht photovoltaic outdoor test facility. In *27th European Photovoltaic Solar Energy Conference and Exhibition*, pages 3247–3249. WIP Munich, Germany, 2012.

[94] The Royal Netherlands Meteorological Institute. Dutch national weather service.

[95] PAUL R. PINET. *Invitation to oceanography - 7th Edition* - . Jones And Bartlett Publishers, Inc, 2014.

[96] Sandia National Laboratories. PV_LIB toolbox.

[97] Christopher J C Burges. A Tutorial on Support Vector Machines for Pattern Recognition. *Data Mining and Knowledge Discovery*, 2:1–43, 1998.

[98] Johan A K Suykens, Tony Van Gestel, Jos De Brabanter, Bart De Moor, Joos Vandewalle, J A K Suykens, and T Van Gestel. *Least squares support vector machines*, volume 4. World Scientific, 2002.

[99] Victron Energy. Smartsolar mppt 75/15, www.victronenergy.com.

[100] Yue Hou, Haoyu Li, Lei Zhao, and Yutian Wang. Temperature-related power loss modeling for buck converter. *IEICE Electronics Express*, 14(6):20170004–20170004, 2017.

[101] P Ineichen, A Zelenka, O Guisan, and A Razafindraibe. Solar radation transposition models applied to a plane tracking the sun. *Solar Energy*, 41(4):371–377, 1988.

[102] Roland Séférian, Sunghye Baek, Olivier Boucher, Jean-Louis Dufresne, Bertrand Decharme, David Saint-Martin, and Romain Roehrig. An interactive ocean surface albedo scheme (osav1. 0): formulation and evaluation in arpege-climat (v6. 1) and lmdz (v5a). 2018.

[103] Richard E. Payne. Albedo of the sea surface. *Journal of the Atmospheric Sciences*, 29(5):959–970, 1972.

[104] Frédéric Hourdin, Marie-Alice Foujols, Francis Codron, Virginie Guemas, Jean-Louis Dufresne, Sandrine Bony, Sébastien Denvil, Lionel Guez, François Lott, Josefine Ghattas, et al. Impact of the lmdz atmospheric grid configuration on the climate and sensitivity of the ipsl-cm5a coupled model. *Climate Dynamics*, 40(9-10):2167–2192, 2013.

[105] Zhonghai Jin, Yanli Qiao, Yingjian Wang, Yonghua Fang, and Weining Yi. A new parameterization of spectral and broadband ocean surface albedo. *Opt. Express*, 19(27):26429–26443, Dec 2011.

[106] Charles Cox and Walter Munk. Measurement of the roughness of the sea surface from photographs of the sun's glitter. *Josa*, 44(11):838–850, 1954.

[107] Howard R Gordon and Michael M Jacobs. Albedo of the ocean–atmosphere system: Influence of sea foam. *Applied Optics*, 16(8):2257–2260, 1977.

[108] Robert Frouin, Myriam Schwindling, and Pierre-Yves Deschamps. Spectral reflectance of sea foam in the visible and near-infrared: In situ measurements and remote sensing implications. *Journal of Geophysical Research: Oceans*, 101(C6):14361–14371.

[109] Dominic J. Salisbury, Magdalena D. Anguelova, and Ian M. Brooks. Global distribution and seasonal dependence of satellite-based whitecap fraction. *Geophysical Research Letters*, 41(5):1616–1623.

[110] Charles H. Whitlock, David S. Bartlett, and Ernest A. Gurganus. Sea foam reflectance and influence on optimum wavelength for remote sensing of ocean aerosols. *Geophysical Research Letters*, 9(6):719–722.

[111] Tom W Brown, Tobias Bischof-Niemz, Kornelis Blok, Christian Breyer, Henrik Lund, and Brian Vad Mathiesen. Response to 'burden of proof: A comprehensive review of the feasibility of 100% renewable-electricity systems'. *Renewable and sustainable energy reviews*, 92:834–847, 2018.

[112] Manish Ram, Dmitrii Bogdanov, Arman Aghahosseini, Solomon Oyewo, Ashish Gulagi, Michael Child, Hans-Josef Fell, and Christian Breyer. Global energy system based on 100% renewable energy—power sector. *Lappeenranta University of Technology and Energy Watch Group: Lappeenranta, Finland*, 2017.

[113] Dolf Gielen, Francisco Boshell, Deger Saygin, Morgan D Bazilian, Nicholas Wagner, and Ricardo Gorini. The role of renewable energy in the global energy transformation. *Energy Strategy Reviews*, 24:38–50, 2019.

[114] John van Zalk and Paul Behrens. The spatial extent of renewable and non-renewable power generation: A review and meta-analysis of power densities and their application in the us. *Energy policy*, 123:83–91, 2018.

[115] Arnulf Jäger-Waldau. The untapped area potential for photovoltaic power in the european union. *Clean Technologies*, 2(4):440–446, 2020.

[116] Alessandra Scognamiglio and François Garde. Photovoltaics' architectural and landscape design options for net zero energy buildings, towards net zero energy communities: spatial features and outdoor thermal comfort related considerations. *Progress in Photovoltaics: Research and applications*, 24(4):477–495, 2016.

[117] RJ Randle-Boggis, Piran Crawfurd Limond White, Joana Cruz, Guy Parker, Hannah Montag, JMO Scurlock, and Alona Armstrong. Realising co-benefits for natural capital and ecosystem services from solar parks: a co-developed, evidence-based approach. *Renewable and Sustainable Energy Reviews*, 125:109775, 2020.

[118] Rijksoverheid. Kamerbrief moties dik-faber over zonneladder als nationaal afwegingskader bij inpassing van zonne-energie. Technical report, Rijksoverheid, 2019.

[119] W Folkers, W van Sark, C de Keizer, W van Hooff, and M van den Donker. Roadmap pv systems and applications. *Study commissioned by the Netherlands Enterprise Agency (RVO) in collaboration with the TKI Urban Energy*, 2017.

[120] Rijksdienst voor Ondernemend Nederland. Appendices hollandse kust (zuid) wind farm sites iii and iv. Technical report, RVO, 2019.

[121] Dutch New Energy Research. Het nationaal solar trendrapport. Technical report, 2020.

[122] Iñaki Arrambide, Itziar Zubia, and Ander Madariaga. Critical review of offshore wind turbine energy production and site potential assessment. *Electric Power Systems Research*, 167:39–47, 2019.

[123] Sundar Venkataraman, Chris Ziesler, Peter Johnson, and Stephanie Van Kempen. Integrated wind, solar, and energy storage: Designing plants with a better generation profile and lower overall cost. *IEEE Power and Energy Magazine*, 16(3):74–83, 2018.

[124] S Astariz and G Iglesias. Output power smoothing and reduced downtime period by combined wind and wave energy farms. *Energy*, 97:69–81, 2016.

[125] Wilfried G.J.H.M. Van Sark, Lex Bosselaar, Pierre Gerrissen, Kendall Esmeijer, Panagiotis Moriatis, Menno Van den Donker, and Gerjan Emsbroek. Update of the Dutch PV specific yield for determination of PV contribution to renewable energy production: 25% more energy! *29th European Photovoltaic Solar Energy Conference and Exhibition*, pages 4095–4097, jan 2014.

[126] Thodoris Karpouzoglou, Brigitte Vlaswinkel, and Johan van der Molen. Effects of large-scale floating (solar photovoltaic) platforms on hydrodynamics and primary production in a coastal sea from a water column model. *Ocean Science*, 16(1):195–208, 2020.

[127] Orsted. Eerste turbine borssele 1&2 geïnstalleerd.

[128] TenneT. Borssele alpha offshore grid connection ready for north sea wind power.

[129] Siemens Gamesa. Sg 8.0-167 dd offshore wind turbine.

[130] L.J. Vermeer, J.N. Sørensen, and A. Crespo. Wind turbine wake aerodynamics. *Progress in Aerospace Sciences*, 39(6):467 – 510, 2003.

[131] BH Bulder, ETG Bot, EJ Wiggelinkhuizen, and FDJ Nieuwenhout. *Quick Scan Wind Farm Efficiences of the Borssele Location*. ECN, 2014.

[132] N O Jensen. A note on wind generator interaction. Technical report, 1983.

[133] I Katic, J Højstrup, and N O Jensen. A Simple Model for Cluster Efficiency. In W Palz and E Sesto, editors, *Proceedings EWEC'86*, pages 407–410, 1987.

[134] Iain Staffell and Richard Green. How does wind farm performance decline with age? *Renewable Energy*, 66:775 – 786, 2014.

[135] Exasun. Black glass^{TM} "power that lasts", data-sheet.

[136] Thomas Nordmann, L Clavadetscher, Wilfried van Sark, and M Green. Analysis of long-term performance of pv systems, 2015.

[137] Dirk C Jordan and Sarah R Kurtz. Photovoltaic degradation risk. Technical report, National Renewable Energy Lab.(NREL), Golden, CO (United States), 2012.

[138] L.W.M. Beurskens S.M. Lensink. Kosten wind op zee 2017. Technical report, Energy Research Centre of the Netherlands, 2017.

[139] Ministry of Economic Affairs and Climate Policy. Sde+ spring 2020, instructions on how to apply for a subsidy for the production of renewable energy. Technical report, 2020.

[140] JÄGER-WALDAU Arnulf. Pv status report 2019. Technical report, European Commission's science and knowledge service, 2019.

[141] IL Wijnant, B van Ulft, B van Stratum, J Barkmeijer, J Onvlee, C de Valk, S Knoop, S Kok, GJ Marseille, H Klein Baltink, et al. The dutch offshore wind atlas (dowa): description of the dataset. Technical report, Tech. Rep. TR-380, Royal Netherlands Meteorological Institute 10 (KNMI ..., 2019.

[142] The Copernicus Atmosphere Monitoring Service. CAMS provides consistent and quality-controlled information related to air pollution and health, solar energy, greenhouse gases and climate forcing, everywhere in the world. https://atmosphere.copernicus.eu.

[143] Marco Rosa-Clot and Giuseppe Marco Tina. Chapter 10 - levelized cost of energy (lcoe) analysis. In Marco Rosa-Clot and Giuseppe Marco Tina, editors, *Floating PV Plants*, pages 119 – 127. Academic Press, 2020.

[144] N.A. Rahim and S. Mekhilef. Implementation of three-phase grid connected inverter for photovoltaic solar power generation system. In *Proceedings. International Conference on Power System Technology*, volume 1, pages 570–573. IEEE.

[145] Mohamed A Elsaharty, Hamdy A Ashour, Elyas Rakhshani, Edris Pouresmaeil, and João P S Catalão. A Novel DC-Bus Sensor-less MPPT Technique for Single-Stage PV Grid-Connected Inverters. *Energies*, 9(4):248, 2016.

[146] Angèle Reinders, Wilfried van Sark, and Pierre Verlinden. Introduction. In *Photovoltaic Solar Energy*, pages 1–12. John Wiley & Sons, Ltd, Chichester, UK, jan 2017.

[147] The International Energy Agency (IEA). 2016 SNAPSHOT OF GLOBAL PHOTOVOLTAIC MARKETS.

[148] Nat Kreamer. SEIA ANNUAL REPORT 10 COMPELLING STORIES ABOUT SOLAR. Technical report, 2016.

[149] V Salas, E Olias, A Barrado, and A Lazaro. Review of the maximum power point tracking algorithms for stand-alone photovoltaic systems. *Solar energy materials and solar cells*, 90(11):1555–1578, 2006.

[150] Efstratios I Batzelis, Pavlos S Georgilakis, and Stavros A Papathanassiou. Energy models for photovoltaic systems under partial shading conditions: a comprehensive review. *IET Renewable Power Generation*, 9(4):340–349, 2014.

[151] S. Berclin Jeyaprabha and A. Immanuel Selvakumar. Model-Based MPPT for Shaded and Mismatched Modules of Photovoltaic Farm. *IEEE Transactions on Sustainable Energy*, 8(4):1763–1771, oct 2017.

[152] S.Z. Mirbagheri, M. Aldeen, and S. Saha. A PSO-based MPPT re-initialised by incremental conductance method for a standalone PV system. In *2015 23rd Mediterranean Conference on Control and Automation, MED 2015 - Conference Proceedings*, 2015.

[153] S Z Mirbagheri, M Aldeen, and S Saha. A PSO-based MPPT re-initialised by incremental conductance method for a standalone PV system. In *Control*

and Automation (MED), 2015 23th Mediterranean Conference on, pages 298–303. IEEE, 2015.

[154] M Godoy Simoes, N N Franceschetti, and M Friedhofer. A fuzzy logic based photovoltaic peak power tracking control. In *Industrial Electronics, 1998. Proceedings. ISIE'98. IEEE International Symposium on*, volume 1, pages 300–305. IEEE, 1998.

[155] T. Hiyama, S. Kouzuma, and T. Imakubo. Identification of optimal operating point of PV modules using neural network for real time maximum power tracking control. *IEEE Transactions on Energy Conversion*, 10(2):360–367, jun 1995.

[156] Liu Yi-Hwa, Huang Shyh-Ching, Huang Jia-Wei, Liang Wen-Cheng, Y H Liu, S C Huang, J W Huang, and W C Liang. A Particle Swarm Optimization-Based Maximum Power Point Tracking Algorithm for PV Systems Operating Under Partially Shaded Conditions. *IEEE Transactions on Energy Conversion*, 27(4):1027–1035, dec 2012.

[157] Sergio Serna-Garcés, Juan Bastidas-Rodríguez, and Carlos Ramos-Paja. Reconfiguration of Urban Photovoltaic Arrays Using Commercial Devices. *Energies*, 9(1):2, dec 2015.

[158] H. Schmidt, S. Rogalla, B. Goeldi, and B. Burger. Module Integrated Electronics – An Overview. *25th European Photovoltaic Solar Energy Conference and Exhibition / 5th World Conference on Photovoltaic Energy Conversion, 6-10 September 2010, Valencia, Spain*, pages 3700–3707, oct 2010.

[159] Masatoshi Uno and Akio Kukita. Current Sensorless Equalization Strategy for a Single-Switch Voltage Equalizer Using Multistacked Buck–Boost Converters for Photovoltaic Modules Under Partial Shading. *IEEE Transactions on Industry Applications*, 53(1):420–429, jan 2017.

[160] Christopher J C Burges. A tutorial on support vector machines for pattern recognition. *Data mining and knowledge discovery*, 2(2):121–167, 1998.

[161] Linear Technology. LTM4611/ Typical Application Ultralow VIN, 15A DC/DC micro Module Regulator.

[162] K Sinapis, C Tzikas, G Litjens, M Van Den Donker, W Folkerts, W G J H M Van Sark, and A Smets. A comprehensive study on partial shading response of c-Si modules and yield modeling of string inverter and module level power electronics. *Solar Energy*, 2016.

[163] A. Mäki and S. Valkealahti. Power Losses in Long String and Parallel-Connected Short Strings of Series-Connected Silicon-Based Photovoltaic Modules Due to Partial Shading Conditions. *IEEE Transactions on Energy Conversion*, 27(1):173–183, mar 2012.

[164] Linear Technology. 60V Synchronous 4-Switch Buck-Boost Controller with Spread Spectrum 98% Efficient 48W (12V 4A). 2017.

[165] W.G.J.H.M. Van Sark, A. Louwen, A.C. De Waal, and R.E.I. Schropp. UPOT: The Utrecht Photovoltaic Outdoor Test Facility. *27th European Photovoltaic Solar Energy Conference and Exhibition*, pages 3247–3249, jan 2012.

[166] UPOT - System layout.

[167] Atse Louwen, Arjen C. de Waal, Ruud E. I. Schropp, André P. C. Faaij, and Wilfried G. J. H. M. van Sark. Comprehensive characterisation and analysis of PV module performance under real operating conditions. *Progress in Photovoltaics: Research and Applications*, 25(3):218–232, mar 2017.

[168] Milieu Centraal. Prijs en opbrengst zonnepanelen - MilieuCentraal.

[169] The International Energy Agency (IEA). 2018 SNAPSHOT OF GLOBAL PHOTOVOLTAIC MARKETS.

[170] Seyed Mohsen Mirhassani, Sayedeh Zahra Mirbagheri Golroodbari, Sayedeh Mina Mirbagheri Golroodbari, and Saad Mekhilef. An improved particle swarm optimization based maximum power point tracking strategy with variable sampling time. *International Journal of Electrical Power & Energy Systems*, 64:761–770, 2015.

[171] G. Velasco-Quesada, F. Guinjoan-Gispert, R. Pique-Lopez, M. Roman-Lumbreras, and A. Conesa-Roca. Electrical pv array reconfiguration strategy for energy extraction improvement in grid-connected pv systems. *IEEE Transactions on Industrial Electronics*, 56(11):4319–4331, Nov 2009.

[172] T. Takashima, T. Tanaka, M. Amano, and Y. Ando. Maximum output control of photovoltaic (pv) array. In *Collection of Technical Papers. 35th Intersociety Energy Conversion Engineering Conference and Exhibit (IECEC) (Cat. No.00CH37022)*, volume 1, pages 380–383 vol.1, July 2000.

[173] J. J. Schoeman and J. D. v. Wyk. A simplified maximal power controller for terrestrial photovoltaic panel arrays. In *1982 IEEE Power Electronics Specialists conference*, pages 361–367, June 1982.

[174] S.Z. Mirbagheri, S. Mekhilef, and S.M. Mirhassani. MPPT with Inc.Cond method using conventional interleaved boost converter. In *Energy Procedia*, volume 42, 2013.

[175] A Safari and S Mekhilef. Simulation and Hardware Implementation of Incremental Conductance MPPT With Direct Control Method Using Cuk Converter. *IEEE Transactions on Industrial Electronics*, 58(4):1154–1161, apr 2011.

[176] Tawfik Radjai, Lazhar Rahmani, Saad Mekhilef, and Jean Paul Gaubert. Implementation of a modified incremental conductance mppt algorithm with direct control based on a fuzzy duty cycle change estimator using dspace. *Solar Energy*, 110:325 – 337, 2014.

[177] Makbul A.M. Ramli, Ssennoga Twaha, Kashif Ishaque, and Yusuf A. Al-Turki. A review on maximum power point tracking for photovoltaic systems with and without shading conditions. *Renewable and Sustainable Energy Reviews*, 67:144 – 159, 2017.

[178] N. Aouchiche, M.S. Aitcheikh, M. Becherif, and M.A. Ebrahim. Ai-based global mppt for partial shaded grid connected pv plant via mfo approach. *Solar Energy*, 171:593 – 603, 2018.

[179] H. A. Sher, A. F. Murtaza, A. Noman, K. E. Addoweesh, K. Al-Haddad, and M. Chiaberge. A new sensorless hybrid mppt algorithm based on fractional short-circuit current measurement and p amp;o mppt. *IEEE Transactions on Sustainable Energy*, 6(4):1426–1434, Oct 2015.

[180] G. Aurilio, M. Balato, G. Graditi, C. Landi, M. Luiso, and M. Vitelli. Fast hybrid mppt technique for photovoltaic applications: Numerical and experimental validation. volume 2014, 2014.

[181] K. S. Tey and S. Mekhilef. Modified incremental conductance algorithm for photovoltaic system under partial shading conditions and load variation. *IEEE Transactions on Industrial Electronics*, 61(10):5384–5392, Oct 2014.

[182] T. K. Soon and S. Mekhilef. A fast-converging mppt technique for photovoltaic system under fast-varying solar irradiation and load resistance. *IEEE Transactions on Industrial Informatics*, 11(1):176–186, Feb 2015.

[183] Ali Reza Reisi, Mohammad Hassan Moradi, and Shahriar Jamasb. Classification and comparison of maximum power point tracking techniques for photovoltaic system: A review. *Renewable and Sustainable Energy Reviews*, 19(0):433–443, 2013.

[184] S. Mirbagheri Golroodbari, Arjen. de Waal, and Wilfried van Sark. Improvement of Shade Resilience in Photovoltaic Modules Using Buck Converters in a Smart Module Architecture. *Energies*, 11(2):250, jan 2018.

[185] O. Lopez-Santos, G. Garcia, L. Martinez-Salamero, R. Giral, E. Vidal-Idiarte, M. C. Merchan-Riveros, and Y. Moreno-Guzmán. Analysis, design, and implementation of a static conductance-based mppt method. *IEEE Transactions on Power Electronics*, 34(2):1960–1979, Feb 2019.

[186] Alberto Dolara, Francesco Grimaccia, Marco Mussetta, Emanuele Ogliari, and Sonia Leva. An evolutionary-based mppt algorithm for photovoltaic systems under dynamic partial shading. *Applied Sciences*, 8(4):558, 2018.

[187] Masatoshi Uno and Akio Kukita. Current Sensorless Equalization Strategy for a Single-Switch Voltage Equalizer Using Multistacked Buck–Boost Converters for Photovoltaic Modules Under Partial Shading. *IEEE Transactions on Industry Applications*, 53(1):420–429, jan 2017.

[188] J. A. Abu Qahouq and Y. Jiang. Distributed photovoltaic solar system architecture with single-power inductor single-power converter and single-sensor single maximum power point tracking controller. *IET Power Electronics*, 7(10):2600–2609, 2014.

[189] Y. Jiang and J. A. A. Qahouq. Single-sensor multi-channel maximum power point tracking controller for photovoltaic solar systems. *IET Power Electronics*, 5(8):1581–1592, Sep. 2012.

[190] J A Gow and C D Manning. Development of a photovoltaic array model for use in power-electronics simulation studies. *IEE Proceedings - Electric Power Applications*, 146(2):193–200, 1999.

[191] S. Cuk and R. D. Middlebrook. A general unified approach to modelling switching dc-to-dc converters in discontinuous conduction mode. In *1977 IEEE Power Electronics Specialists Conference*, pages 36–57, June 1977.

[192] Analog Devices. Ltspice. 1995 - 2018.

[193] Analog Devices. AD626 Low Cost, Single-Supply Differential Amplifier. Technical report, 2003.

[194] Texas Instruments. CDx4HC405x, CDx4HCT405x High-Speed CMOS Logic Analog Multiplexers and Demultiplexers.

[195] Samer Fawzy, Ahmed I Osman, John Doran, and David W Rooney. Strategies for mitigation of climate change: a review. *Environmental Chemistry Letters*, pages 1–26, 2020.

[196] Hamed Hanifi, Matthias Pander, Bengt Jaeckel, Jens Schneider, Afshin Bakhtiari, and Waldemar Maier. A novel electrical approach to protect pv modules under various partial shading situations. *Solar Energy*, 193:814–819, 2019.

Acknowledgements

Throughout the writing of this dissertation I have received a great deal of support and assistance.

I would like to thank you Wilfried for your invaluable supervision, support and encouragement during four years my PhD research. Your insightful feedback pushed me to sharpen my thinking and brought my work to a higher level. Working with you was a great experience, I am happy that I had this opportunity to work with you in a pleasant atmosphere. I would also like to thank you Atse, for your technical support on my research. I would like to thank Pearl PV Cost Action, to make it possible for us to attend fruitful workshops in the field of solar Energy. Angèle and David, thank you for the efforts you put on this Action.

I would also like to thank industrial parties who were active on projects we were involved in during this research. Thank you Lenneke and Nico from TNO. Thank you Rudi for welcoming me to Heliox for a short period of time during my PhD. Finally, Special thanks to Allard and Brigitte from Oceans of Energy.

Anne, Odysseas, Panos, and Ivan you were all lovely colleagues. Working on the same office with you made my PhD life much more delightful. Anne, I will never forget working together on the floating project and our work plannings on the way to the floater location. A very special gratitude goes out to all other members of PV integration team: Bhavya, Wouter, Lennard, Kostas, Ioannis, Eelke, Nick, and Nico. Thank you Douwe for contributing a lot for preparing one of the papers published in this thesis.

I must also thank all my helpful and kind colleagues in the Copernicus Institute of Sustainable Development. Annand, Birka, Ernst, David, Floor, Gert Jan, Gijs, Ibti, Ivan, Juraj, Laurens, Li, Lukas, Madeleine, Marc, Matteo, Oscar, Pita, Robert, Steven, Thuy, Vincent, Vincenz, Wen, Will, Wina, thanks for making E&R a wonderful place. Christian, thank you for your nice suggestions introducing very nice destinations in your beautiful country, Italy. Also, thank you Federica for delicious Italian dishes. Thank you Szabolcs, we spent a lot of time in the campus together, that was a great time. Hu Jing, thank you for introducing books written by Nasim Taleb. Thank you Marte for bringing a sense of art to our group by playing piano. Special thanks to Aisha, you always make the atmosphere comfortable and friendly. Thank you Anna for your charming smile. Ana thank you for being so kind. Thank you Sara for the time we spent together talking about everything in the world. Thank you Ario and Shahab, I wish we can plan a trip to Iran together. Thank you Tarek for being always like my encouraging brother. Special thanks to Jesús for calling me Sarita and making my day. Thank

you Siham and Fiona, without you all nothing is in order.

Finally, my deep and sincere gratitude to my family for their continuous and unparalleled love, help and support. I am grateful to my sister for always being there for me as a friend. I am forever indebted to my parents for giving me the opportunities and experiences that have made me who I am.

Hamed, my life partner, my love, and my best friend! Thank you very much for being by my side for six years (and counting)! Could not have done it without you. Chokh mamnoon!

About the author

S. Zahra Mirbagheri Golroodbari was born in Lahijan, Iran, on 16 September 1983. She obtained a Bachelor of Engineering degree in Electrical Engineering at the Azad University of Isfahan in 2005. She started the master program Power Electronics at University of Malaya, in 2011. She defended her master thesis with the title of "Maximum Power Point Tracker for Standalone Photovoltaic System with Incremental Conductance Variable Step Size Method" in 2013. She spent three years on research at University of Melbourne and Technical University of Delft.

In April 2017, she started a PhD at the Copernicus Institute of Sustainable Development. In her PhD, she Worked on floating PV systems and researched on the smart module design to mitigate the mismatch conditions. She gave oral presentations at two international conferences, and presented posters at two international conferences, she won the Grand Cru prize the Dutch Sunday in 2019, and was nominated twice for a best student presentation award. She was main author of four peer-reviewed journal publications, also she has submitted another paper which is still under review at the date of publishing this book. She also supervised students and is co-author for one submitted paper. After her PhD, she would like to stay active as a researcher in the field of solar and renewable energy.

Journal publications

- Mirbagheri Golroodbari, S.Z., De Waal, A. and Van Sark, W.G., 2018. Improvement of shade resilience in photovoltaic modules using buck converters in a smart module architecture. Energies, 11(1), p.250.
- Golroodbari, S.Z.M., de Waal, A.C. and van Sark, W.G., 2019. Proof of concept for a novel and smart shade resilient photovoltaic module. IET Renewable Power Generation, 13(12), pp.2184-2194.
- Golroodbari, S.Z. and van Sark, W., 2020. Simulation of performance differences between offshore and land-based photovoltaic systems. Progress in Photovoltaics: Research and Applications, 28(9), pp.873-886.
- Golroodbari, S.Z.M., Vaartjes, D.F., Meit, J.B.L., van Hoeken, A.P., Eberveld, M., Jonker, H. and van Sark, W.G.J.H.M., 2021. Pooling the cable: A techno-economic feasibility study of integrating offshore floating photovoltaic solar technology within an offshore wind park. Solar Energy 219 (2021) 65-74.
- Golroodbari, S.Z. and van Sark, W., 2021. Effect of Dynamic Albedo Modeling on the Performance of Offshore Floating Photovoltaic Systems, submitted to Solar Energy.

Prizes

- Mirbagheri Golroodbari, S.Z. (Sara) 13.11.2019 Recipient Grand Cru 2019

Conferences publications

- Mirbagheri Golroodbari, S.Z. (2017) Presenter 32rd EU PVSEC Amsterdam An Adaptive PSO-Based Approach for Optimal Energy Harvesting in PV Systems, Poster, 6BV.1.49
- Mirbagheri Golroodbari, S.Z. (24.09.2018) Presenter 33th EU PVSEC Brussels Architecture, Design and Simulation for a Shade Resilient Smart Module.
- Mirbagheri Golroodbari, S.Z. (09.09.2019) Speaker 34th EU PVSEC Marseille Architecture, Design and Simulation Floating PV system on the North Sea.
- Mirbagheri Golroodbari, S.Z. (08.09.2020) Speaker 35th EU PVSEC Quantification of the Effect of Albedo Modeling for a Floating PV System on the North Sea.

ISBN 978-94-6416-590-6